MEASUREMENTS OF HEAT, STRAIN, AND REFRACTIVE INDEX WITH MULTICORE OPTICAL FIBERS

by

Sema Güvenç Kılıç

B.S., Physics, Yildiz Technical University, 2010

B.S., Mathematics, Yildiz Technical University, 2012

M.S., Boğaziçi University, 2014

Submitted to the Institute for Graduate Studies in
Science and Engineering in partial fullfilment of
the requirements for the degree of
Doctor of Philosophy

Graduate Program in Physics

Boğaziçi University

2020

ACKNOWLEDGEMENTS

First, I would like to thank my advisor Prof. M. Naci Inci for his contributions, patience, and enthusiasm with his never-ending moral support during my doctoral period. His guidance provided me to improve my critical and analytical thinking abilities and brought my research studies to a higher quality level. His immense knowledge and experience have encouraged me throughout my Ph.D. thesis period, and it is an absolute honor for me to pursue my Ph.D. study under his supervision. I will never forget his help, advice, and motivation. His constructive criticisms and optimistic point of view were some of his prominent positive characteristics that I would like to project on my future academic life.

I would like to express my special appreciation to my husband, Dr. Ufuk Kılıç, because his encouragement, directives as well as full support during my entire Ph.D. education positively back me up. I would like to thank him for his help during the learning process of Finite Element Modelling technique, his contributions, guidance, and being with me throughout all this academic period. Our discussions on these fiber optic sensing research topics were so helpful and fruitful and provided me another perspective.

I would like to thank my dear friends and colleagues Dr. Belkis Gökbulut, Dr. Gülşen Görk, Mr. Arda İnanç, and Asst. Prof. Ekrem Yartaşı for their friendships and supports throughout my doctoral period.

I would like to offer my special thanks to Prof. Christos Argyropoulos for giving me the opportunity to learn and apply the finite element computation technique to various fiber-optic systems which lead us to gain an in-depth understanding on their underlying physical mechanisms. I would like to extend my sincere thanks to my friends Asst. Prof. Tianjing Guo, Asst. Prof. Ying Li, Dr. Larousse Khosravi Khorashad, and Dr. Bouyon Jin for their friendships and helps for learning period of FEM simulation method.

I would like to express my sincere gratitude and appreciation to Prof. Ming Han whose guidance and support were invaluable throughout the seven-core optical fiber sensing project. I also would like to thank him for his never-fading immense support which led me to experimentally realize another sensing method so-called Fiber Bragg Grating based refractometer. I would like to extend my thanks to Dr. Guigen Liu, Mr. Yupeng Zhu, and Mr. Qiwen Sheng for their friendships and help during the learning of Fiber Bragg Grating fabrication and sensing process.

I would like to thank Prof. Şenol Mutlu and his Ph.D. student Mr. Ozan Ertop to help for Aluminum coating process of our multicore fibers. I would like to thank Prof. M. Burçin Ünlü and Prof. Heba Yüksel for their support throughout this Ph.D. period. I would like to thank Prof. Mathias Schubert for his valuable advices and support.

I would like to thank The Scientific and Technological Research Council of Turkey (TUBITAK) for their financial support throughout one year during my stay in Lincoln-Nebraska-USA to carry out the proposed research study which is titled as `Interferometric temperature and heat sensor with a four-core optical fiber and its finite element simulations` in the Electrical and Computer Engineering Department at the University of Nebraska, Lincoln (2214-A- International Research Fellowship Program for Ph.D. Students-BIDEB 2214-A Program).

Finally, I would like to thank my father “Selahattin Güvenç”, mother “Mine Güvenç”, and brothers “Murat Güvenç” and “Hüseyin Güvenç” for their encouragement, unconditional trust, continued moral support, endless patience, and motivation throughout my entire life and academic career. I am forever indebted to my family for giving me the opportunities, experiences, and support that have made me who I am.

ABSTRACT

MEASUREMENTS OF HEAT, STRAIN, AND REFRACTIVE INDEX WITH MULTICORE OPTICAL FIBERS

In this thesis, different types of multicore optical fibers are designed and employed in the optical sensing experimental setups to investigate their detection abilities of temperature, heat transfer rate, strain, and refractive index. In the first section of this comprehensive investigation, a four-core optical fiber is introduced as a calorimetric gauge for the measurements of one-dimensional heat transfer rates. Transient heat pulses from an Nd:YAG laser are sent onto Aluminum coated surface, provided that the laser pulse is focused onto one of the optical fiber cores only. As a result of this, a phase shift in the interference pattern occurs and the corresponding optical signal is recorded by a CMOS camera. In the second section, the thermal expansion property of a stainless-steel cylinder is used to generate a strain on the optical fiber cores. Multicore fiber is coiled around a solid stainless-steel cylinder to obtain a circular optical fiber loop and this cylinder is placed onto the heater. Heating the stainless-steel cylinder results in thermal expansion in radial direction and a shear strain in the optical fiber cores. Thereby, a phase shift in the transmission spectrum is observed and monitored by the camera. As a third study, a four-core fiber is proposed and demonstrated for temperature sensing and heat transfer rate measurements. Laser heat pulses from are sent onto this Aluminum coated surface, which results in a variation in the interference pattern as a result of change in the refractive index and physical lengths of the cores. In addition to this experiment, hot air vortices were sent onto Aluminum coated surface of the fiber and variations in interference pattern are recorded. In the last section, a seven-core optical fiber with two fiber Bragg gratings is employed to detect the refractive index changes of surrounding environment. A small portion of optical fiber is etched in order to further expose the outer six cores to the surrounding environment. As the outer cores are affected by both temperature and refractive index change, the center core is only affected by the temperature.

ÖZET

ÇOKLU ÇEKİRDEKLİ FİBERLER İLE ISI, GERİLME VE KIRILMA İNDİSİ ÖLÇÜMLERİ

Bu tezde, farklı türlerde çok çekirdekli optik fiberler, optiksel algılama deney düzeneklerinde sıcaklık, ısı transfer oranı, gerinim ve kırılma indisi algılama yeteneklerini gözlemlemek için kullanılmıştır. Bu kapsamlı araştırmanın ilk aşamasında, dört çekirdekli optiksel fiber, bir boyutlu ısı transfer oranlarının ölçülmesi için kalorimetrik gösterge olarak takdim edilmiştir. Nd:YAG lazerden geçici ısı atımları, Alüminyum kaplamalı yüzeye optiksel fiber içerisindeki bir çekirdeğe odaklanacak şekilde gönderilir. Bunun sonucunda, girişim deseninde bir kayma meydana gelir ve CMOS bir kamera tarafından kaydedilir. İkinci bölümde, optiksel fiberin çekirdekleri üzerinde bir gerilme meydana getirmek için paslanmaz çelik bir silindirin ışınsal genleşme özelliği kullanılır. Çok çekirdekli fiber, paslanmaz çelik bir silindirin etrafına bir halka olacak şekilde sarılır ve silindir ısıtıcının üzerine yerleştirilir. Paslanmaz çelik silindirin ısıtılması radyal yönde bir termal genleşmeye ve optiksel fiberin çekirdeklerinde kayma gerinimine sebep olur. Böylelikle, iletim spektrumunda bir faz kayması gözlemlenir ve kamera tarafından görüntülenir. Üçüncü bir çalışma olarak, dört çekirdekli fiber sıcaklık algılama ve ısı transfer oranı ölçümleri için sunulmuş ve gösterilmiştir. Çekirdeklerin uzunluğunda ve kırılma indisinde değişimin bir sonucu olarak girişim desenindeki farklılıklara yol açan lazer ısı atımları, Alüminyum kaplamalı yüzeye gönderilir. Bu deneye ek olarak, sıcak hava girdapları Alüminyum kaplamalı yüzeye gönderilir ve girişim desenindeki değişimler kaydedilir. Son bölümde, fiberin etrafını çevreleyen ortamın kırılma indisindeki değişiklikleri tespit etmek için yedi çekirdekli bir optik fiber kullanılır. Dışarıdaki altı çekirdeği çevredeki ortama daha fazla maruz bırakmak için, optiksel fiberin küçük bir kısmı asitle uzaklaştırılmıştır. Dışarıdaki altı çekirdek sıcaklık ve kırılma indisi değişiminden etkilenirken, merkezdeki çekirdek sadece sıcaklıktan etkilenmektedir.

TABLE OF CONTENTS

LIST OF FIGURES

LIST OF TABLES

LIST OF SYMBOLS

θ_1	Angle of incidence
θ_2	Angle of refraction
θ_c	Critical angle
n_1	Lower refractive index
n_2	Higher refractive Index
α	Acceptance angle
Δ	Fractional refractive index difference
d_{core}	Diameter of core
$d_{cladding}$	Diameter of cladding
$z(x,y)$	Out of plane displacement of the object surface
I_0	Intensity contribution of a single core
δ	Separation between two horizontal or vertical cores
f	Focal length of the lens
λ	Wavelength of the laser source
θ	Illumination angle
V	Visibility of the interference pattern
φ	Phase
n	Refractive index of the fiber core
l	Length of the sensitive part of the fiber
$\Delta\varphi$	Average phase change
ΔT	Average temperature change
T_0	Ambient temperature
ρ	Density of the fiber

c	Specific heat capacity of the fiber
k	Thermal sensitivity
γ	Thermal diffusivity
d	Diffusion length
K	Thermal conductivity coefficient
Q	Heat transfer rate
ε	Strain
C	Volume concentration
n_w	Refractive index of distilled water
n_A	Refractive index of acetone
n_E	Refractive index of ethanol
E_z	Z component of the Electric Field
Δl	Path Length Difference
I_R	Intensity of Reflected Light
I_T	Intensity of Transmitted Light

LIST OF ACRONYMS/ ABBREVIATIONS

TiO_2	Titanium Dioxide
Ge	Germanium
UV	Ultraviolet
Nd:YAG	Neodymium-doped Yttrium Aluminum Garnet
Al	Aluminum
HeNe	Helium Neon
SiO_2	Fused Silica
FOS	Fiber Optic Sensor
CMOS	Complementary Metal Oxide Semiconductor
TIR	Total Internal Reflection
NA	Numerical Aperture
LED	Light-Emitting Diodes
VCSEL	Vertical Cavity Surface-Emitting Lasers
GRIN	Graded index
SCF	Single core fiber
MCF	Multicore Fiber
SMF	Single Mode Fiber
MMF	Multimode Fiber
PCF	Photonic Crystal Fiber
IFOS	Interferometric Fiber Optic Sensor
FPI	Fabry-Perot Interferometer

MZI	Mach–Zehnder interferometer
MI	Michelson interferometer
SI	Sagnac interferometer
FBG	Fiber Bragg Grating
CFBG	Chirped Fiber Bragg Grating
DFOS	Distributed Fiber Optic Sensor
SEM	Scanning Electron Microscope
RI	Refractive Index
DFB	Distributed Feedback
BHF	Buffered Hydrofluoric Acid
OSA	Optical Spectrum Analyzer
DAQ	Data Acquisition
LD	Laser Diode
TEC	Temperature Controller
LDC	Laser Current Controller
FG	Function Generator
PD	Photo Diode
PC	Polarization Controller
FEM	Finite Element Modelling
DI	Distilled Water
1D	One dimensional
3D	Three Dimensional

μm	Micrometer
$^{\circ}C$	Celsius
nm	Nanometer
K	Kelvin
mW	Miliwatt
m	Meter
mm	Millimeter
ms	Millisecond
kJ	KiloJoule
s	Second
cm	Centimeter
pm	Picometer
$\mu\varepsilon$	Millistrain
rad	Radians
$mrad$	Milliradians
CCD	Charge-Coupled Device
T	Temperature
r	Position
t	Time
Hz	Hertz
mA	Milliampere
V	Volt

ml	Milliliter
RIU	Refractive Index Unit
LASER	Light Amplification by Stimulated Emission of Radiation
LIGO	The Laser Interferometer Gravitational-Wave Observatory

1. INTRODUCTION

Recent developments in fiber optic technology have provided a great opportunity to demonstrate the detection ability of fiber optic sensors (FOSs) for various physical, chemical, and biological parameters [1]. Because of inherent and distinguishing advantages of FOSs, they have been utilized in many different fields; such as military, nuclear power industry, medical applications, and optical communication systems [2]. In addition to the structural simplicity and design flexibility of FOSs, their durability as response to possible harsh, corrosive, high temperature, and high voltage environments brings them into greater prominence among the other types of sensor applications [3].

FOSs based on interferometric methods have a significant and crucial role in detecting numerous external physical parameters such as temperature, heat, rotation, pressure, refractive index, strain, stress change, displacement, vibration, polarization, humidity, linear and angular position, viscosity, etc. [4]. Small size, longer lifetime, simplicity, high sensitivity and accuracy, design, low cost, high flexibility, durability, low propagating loss, immunity to electromagnetic interference, and reliability in signal detection can be listed as some of the unique and remarkable features of the fiber optic interferometry [5].

Over the past 60 years, many theoretical and experimental studies on FOSs have been carried out using different types, configurations, or combinations of optical fibers. At the early stage of such studies, in general, single core, single mode, and multiple number of optical fibers were preferred in the sensor application experiments which are based upon the interferometric methods such as Mach Zehnder Interferometer, Fabry Perot interferometer, or Michelson Interferometer. One of the most well-known studies of fiber optic interferometer to measure temperature and pressure changes was successfully presented by G. B. Hocker in 1979 [6]. In this study, to generate an interference pattern in transmission scheme, two single core optical fibers were employed. By applying temperature to one of the optical fibers, a phase shift in the interference pattern occurred as a result of temperature induced refractive index change and the thermal expansion of the fiber core. Similarly, pressure was applied to one of the fibers and pressure change was determined depending on the amount of phase shift. In 1992, the configuration of the Fabry-Perot interferometer was used to measure heat transfer rates by K. S. Chana *et al*. [7]. One year later, in 1993, a

miniature interferometric fiber optic temperature sensor was constructed by M. N. Inci and his colleagues by using single mode and single core optical fiber. The end of the fiber was cut properly and then coated with titanium dioxide (TiO_2). A short single core and single mode fiber was added to TiO_2 coated end of the fiber by using fusion splicer. TiO_2 coated surface served as an internal mirror in the optical fiber which introduced this system as a Fabry-Perot interferometer. By applying heat to second short optical fiber, a shift in the interference pattern occurred. The temperature change and the amount of heat accumulated inside the optical fiber core were calculated [8]. In addition to these sensing structures, which based upon Mach Zehnder and Fabry Perot Interferometer, one of the recent studies which employs Michelson interferometer to form an interference pattern in reflection spectrum was presented by H. Meng *et al.* to detect refractive index changes in liquids, theoretically and experimentally [9].

In the aforementioned studies, experiments were performed using single core and single mode optical fibers with different interferometric configurations. Within the last two decades, experiments have become less complicated and sensors have become more compact with the help of multicore fiber structures. A multicore fiber was employed for the first time by M.J. Gander *et al*. for the bending measurements [10]. In this experiment, a four-core optical fiber was preferred and the phase difference between modes propagating in different cores was measured by using Fourier analysis of a two-dimensional far-field interferogram which consists of six superimposed interferograms due to each combination of optical fiber core pairs. A linear relationship was obtained between the phase difference and the bend angle. Another impressive and detailed study with a multicore fiber was carried out by Libo Yuan *et al.*, in 2007. A series of experiments with a four-core optical fiber were carried out to detect several to physical parameters such as rotation, bending, and temperature [11]. In the first stage of the experiment, the optical fiber was bended at certain angles to demonstrate that the fiber was able to detect the bending and the shifts in the interference pattern were recorded by a CCD camera. As a second study to demonstrate the rotation detection ability of this sensor, the fiber was rotated with small angles and the rotation pattern of the interference was detected by the camera. In the final step of this project, multicore fiber was placed between two plates of Peltier device which consists of one hot and one cold plate to generate a heat flow inside the optical fiber cores. As a consequence of this process, no change in interference pattern was observed, since all the cores were experienced with this

temperature change, simultaneously. In 2012, a temperature sensor for the purpose of detecting refractive index changes was constructed by R. Romaniuk *et al.* by using two-core optical fiber [12]. In this paper, mainly, the changes in both length and refractive index of the region between the two fiber cores were examined, depending on the temperature increase, experimentally and theoretically.

Recent studies on sensing applications by using different types of fibers with smart structures have been focused on temperature and heat measurements. In 2016, L.V. Nguyen *et al.* fabricated a special fiber structure, used as an interferometric high temperature sensor, which can operate up to 1100˚C [13]. In this special fiber structure, the fiber core was surrounded by three air cores which served as cladding. This optical fiber system still holds the total internal reflection phenomenon observed in regular fiber structures. In this experiment, using this special fiber structure, a shift in the interference pattern was observed because of the increase in temperature. Another recent study reported by Guigen Liu *et al.* successfully showed that a fiber optic structure-based temperature sensor can operate at temperatures higher than 1000˚C [14]. In this study, the miniature silicon crystal Fabry Perot interferometry was attached to a single core optical fiber using a fusion splicer. The silicon part was heated with a laser and the shifts in the interference pattern were examined.

The arrival of intense laser light with a periodic pattern on a single or multi core fiber results in permanent refractive index changes. This technique is called as the fiber Bragg gratings and was first reported by Kenn Hill in 1978 where the photosensitivity feature of optical fibers with Germanium (Ge) doped cores was presented [15]. With the further development of optoelectronics technology, the Bragg gratings; especially uniform, chirped, tilted, and phase shifted forms have been fabricated to sense many physical and chemical parameters such as refractive index [16-19], temperature [20-22], strain [23], and pressure [24]. However, among the very first but fundamental sensor applications, which used fiber Bragg gratings, were reported by G. Meltz and W. W. Morey et. al. in 1989 and 1990, respectively [25, 26]. In their studies, the Bragg gratings in Ge doped fiber cores were fabricated by exposing Ultraviolet (UV) light to a short section of fiber and finalized their investigations by employing the fiber Bragg gratings so as to sense temperature and strain parameters. In another early study related to fiber Bragg gratings, M. A. Davis *et al.* reported the detection of the strain change by using five arrays of 12 fiber Bragg gratings [27].

Various configurations and combinations of different single core and multicore fibers with or without Fiber Bragg Gratings have been extensively studied and continued to become an active research field to compensate the ultra-high sensing demand of new generation optoelectronic circuit designs [28, 29]. Hence, in this thesis, we have presented our detailed investigation on how to fabricate multicore fiber optic sensors and their strong detection abilities of various physical parameters such as heat transfer rates, strain, temperature, and refractive index changes. In these sensing studies, two different types of multicore fibers are employed: four core and seven core optical fibers.

Firstly, a four-core optical fiber is employed to determine the heat transfer rate measurements. In this experiment, transient heat pulses from an Neodymium-doped Yttrium Aluminum Garnet (Nd:YAG; $Nd:Y_3Al_5O_{12}$) laser with a pulse duration of 0.6 s are sent onto the Aluminum (Al) coated cross sectional end of the four core optical fiber, in such a way that only one fiber core is targeted. This results in an optical path length difference between four guiding cores due to the temperature-induced change in the refractive index and physical length of the fiber core.

Another study with the four-core optical fiber is achieved to investigate the strain, which is induced by the radial expansion of a solid stainless-steel cylinder. A certain part of a four-core fiber is coiled around a cylinder which is placed onto a heater. Radial expansion in the cylinder gives rise to a shear strain in the fiber cores and introduces an optical path-length difference between the fiber core pairs. This results in a phase shift in the interference, pattern which is monitored and recorded by a Complementary Metal Oxide Semiconductor (CMOS) camera.

In chapter three, a four-core fiber is proposed and demonstrated for temperature sensing and heat transfer rate measurements, successfully. Cladding region with a length of 4-5 cm is removed from the center part of the optical fiber to coat half of this surface with Al. Laser heat pulses from Nd:YAG laser of 532 nm are sent onto this Al coated surface, which results in a variation in the interference pattern in the transmission scheme as a result of change in the refractive index and physical lengths of the cores. These heat pulse applications cause a heat dissipation among the fiber cores. Applying heat pulses also causes thermal expansion in the radial direction, which is negligible when it is compared to the

thermal expansion in the axial direction. In addition to experiments with laser heat pulses, a different experiment series based on unsteady temperature change measurements is also conducted. Hot air vortices were sent onto Al coated surface of the fiber and variations in interference pattern are recorded by the CMOS camera.

Different from the first three studies, last sensing work was carried out with a seven-core optical fiber. In this study, a seven-core fiber optic refractive index sensor, based on the Fabry-Perot interferometer, which consists of two Chirped Fiber Bragg Gratings, is introduced. Cladding region is etched to reach the outer cores and expose the outer cores to the ambient environment. While optical modes of outer six cores are affected by both temperature and refractive index changes of the surrounding liquid, the optical mode in the center core is affected by the temperature changes only. Because only a small part of the cladding is removed, the sensor maintains excellent mechanical strength and stability.

The layout of the thesis consists of the basic theory on single and multicore fibers, fiber Bragg gratings, interferometric methods in sensor applications, which are followed by the experimental results and discussion parts of each multicore optical fiber sensor, and conclusion part.

2. FUNDAMENTALS OF OPTICAL FIBERS

2.1. Introduction

One of the most crucial developments in the waveguide technology was the discovery of optical fibers, which opened up new research avenues due to their unique features such as low loss transmission, immunity to electromagnetic interference, small size, light weight, and information carrying capacity [30]. Since the invention of the laser and fabrication of different types of optical fibers in 1960s, numerous investigations and practical applications have gained speed for the emergence of sensing technologies and optical communication industry with different methods using their distinctive properties [31].

As a precision metrology system, optical fibers are frequently employed in sensor applications which provide a great opportunity to detect many different physical parameters with higher sensitivity as it is compared with the traditional sensor types [2]. Simplicity, high accuracy, design elegancy, flexibility, low cost, small size, light weight, and reliability in signal detection can be given as some unique and remarkable features of FOSs [32]. Furthermore, FOSs are regarded as durable and robust enough for many different environments such as high voltage and high temperature [33].

FOSs have had a key role in detecting many of the external physical, chemical, and biological parameters such as temperature, heat, pressure, magnetic field, refractive index, strain, stress, displacement, rotation, vibration, flow rate etc. [4, 34]. In addition to these parameters, FOSs have been used to determine a change in ph value, humidity, and to monitor the radiation pipeline conditions [35, 36]. The basic working mechanism of FOSs is based upon the variation in the phase, intensity, or wavelength of the light propagating through the fiber core(s) induced by external perturbations [4]. Depending on the operating principles and fabrication processes, in general, FOSs can be categorized into 3 main branches: Interferometric fiber optic sensors, Graded index fiber optic sensors, and Distributed fiber optic sensors [37]. In this thesis, mainly, first two types of metrology

methods were focused and studied and further information about these methods will be given in the fiber optic sensors section.

FOSs have attracted a great attention due to their distinctive properties such as multiplexing, remote sensing, and simultaneous sensing ability [5]. The first method in sensing applications is the fiber optic interferometry to detect and measure many physical, chemical, and biological quantities in studies. Depending on operation principles, there are many different configurations of optical interferometry exist. For example, Fabry Perot, Mach Zehnder, Michelson, and Sagnac are listed as main interferometric methods [5]. These configurations can be obtained by using multiple number of fibers, multicore fibers, or combinations of different types of optical fibers such as single mode, multimode, single core, multicore optical fibers, and optical fibers with different diameters. In general, the basic working principle of these methods is based upon forming an interference pattern of two or multiple beams which propagate through the optical fiber cores. A variation in the interference pattern occurs when an external disturbance is applied to the sensing part of an optical fiber or the sensing optical fiber. Therefore, the amount of physical quantity can be determined by measuring the optical path difference between the propagating beams.

The second method in constructing a fiber optic sensor is based upon fiber Bragg grating. Exposing the fiber core to intense laser light (especially UV laser light) causes a permanent refractive index modulation, which is called the Bragg grating in fiber cores [38]. At each point where the refractive index is changed, small amount of light is reflected. All this reflected light combines into a large reflection. Depending on the phase mask used during the fabrication process, different types of fiber Bragg gratings such as uniform, chirped, phase shifted, tilted, and long period can be written into optical fiber cores. Employing these fiber Bragg gratings in sensing experimental setups helps to determine many external parameters with very high accuracy.

In FOS applications, the type of the optical fiber utilized in experiments is another important factor. During the early stages of FOS systems, single core, single mode, and multiple number of optical fibers were used in the experiments [6]. Due to the need for extreme sensing ability with high design flexibility to employ such sensors in complicated devices, FOSs have gained increasing interest which led further developments in optical

fiber structures with different shapes, types, and combinations. In recent years, technological advancements in especially micro/nano fabrication techniques and laser technologies lead to significant improvements in optical fiber structures. More sophisticated fiber structures, such as multicore fibers, have become more visible in the sensing applications and their potential use have significantly increased due to offering a cheaper alternative and more flexible sensing methods.

This chapter briefly reviews the basic optical fiber structure, types of optical fibers, working mechanism of optical fibers, applications of optical fibers, fiber optic sensors, and sensing methods; which are followed by a discussion part.

2.2. Basic Structure and Working Principle of Optical Fibers

An optical fiber is simply described as a cylindrical dielectric waveguide which consists of core(s), cladding, and silicon or buffer jacket and is made of low loss materials with high chemical purity [39]. A simple and basic fiber structure is demonstrated in Figure 2.1.

A Silicon jacket or a buffer layer surrounds the outer surface of the fiber structure, which is a type of plastic material of an elastic nature. This buffer layer provides an extra mechanical protection to the cladding and cores of the optical fiber from physical damage [40].

The cladding layer is generally made of a dielectric material (silica glass) with a lower refractive index than the fiber cores. Cladding region prevents the loss of light from the fiber cores and decreases the scattering loss at the surface of the core [40]. In addition to these, cladding part increases mechanical strength of the fiber structure because the fiber core with a small diameter has a rather lower strength.

The fiber core is a cylindrical structure of a dielectric material and is generally made of doped fused silica (SiO_2) [41]. The diameter of the core is smaller than the cladding and the buffer jacket layers. The optical fiber core provides a path for the light propagation and prevents the light from radiating out of the fiber. In general, to increase both the refractive index and the photosensitivity of the fiber core, the core is doped with Ge [42]. Because of

that reason, the refractive index of the optical fiber core is slightly higher than that of the cladding part, which leads to confine and guide the light along the core(s).

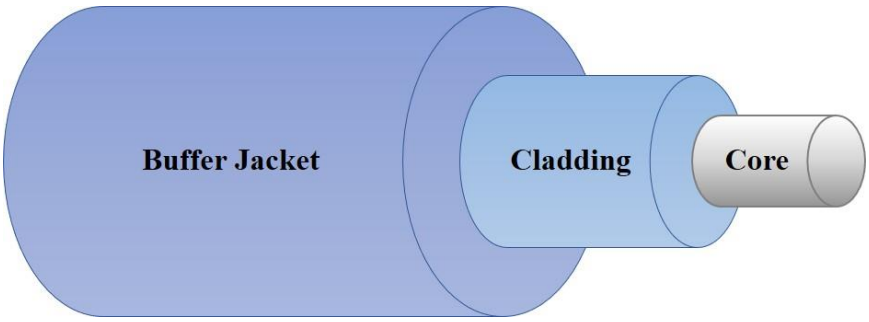

Figure 2.1. Basic structure of an optical fiber which consists of buffer jacket, cladding, and core(s).

Engineering the refractive index difference between core and cladding enables to guide the light along the cores by abiding the Total Internal Reflection (TIR) rule. Because cladding structure does not absorb any light, the light in the optical fiber travels through the core(s) with very low loss and longer distances. This simplistic mechanism is an excellent example to the waveguide systems. Basic description of total internal reflection is the reflection of total amount of incident light at the interface or boundary between two different media. When the light travels from a medium with higher refractive index (n_1) to another medium with lower refractive index (n_2), it bends away from the normal, which is shown by red dashed lines in Figure 2.2 [43]. The total internal reflection and critical angle are shown in detail in Figure 2.2.

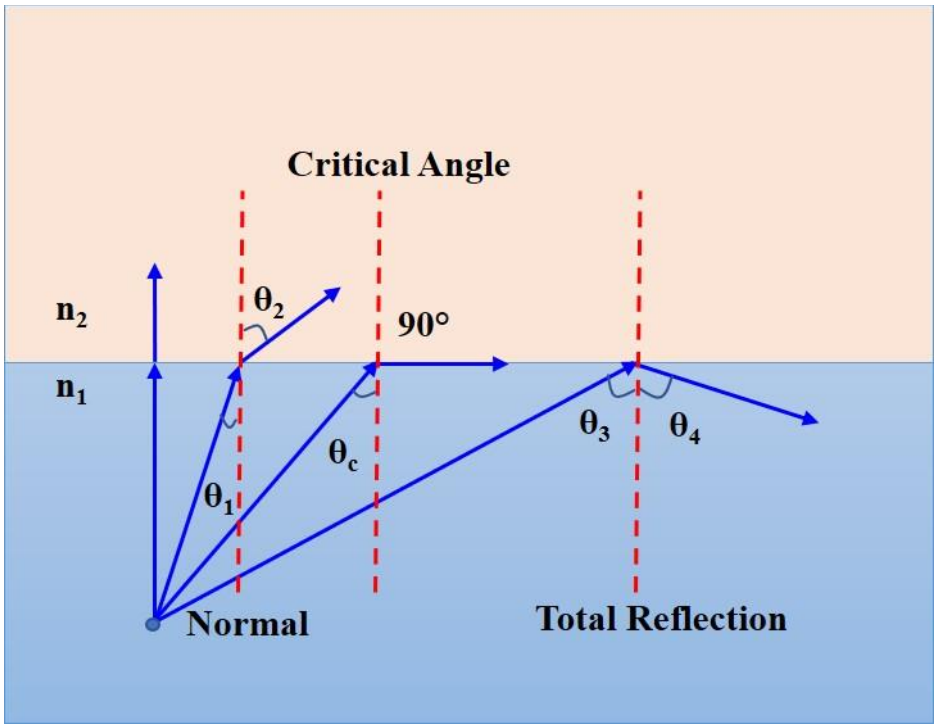

Figure 2.2. Schematic representation of total internal reflection and critical angle. Red dashed line shows the normal line.

According to the Snell Law, the relation between the refractive indices of the first and the second environments and the angle of incidence and refraction is given by the following formula:

$$n_2 \sin\theta_2 = n_1 \sin\theta_1 \tag{2.1}$$

where n_1 and n_2 are the refractive index of the first environment and the second environment, respectively; θ_1 is the angle of incidence, and θ_2 is the angle of refraction. Because $n_1 > n_2$, it can be obtained easily that $\theta_2 > \theta_1$.

As seen from the Figure 2.2, while the angle of incident light increases, the angle of refraction also increases. At the point where the angle of refraction is equal to 90°, the angle of incidence is called as the 'critical angle', which is given by the following equation [43]:

$$\theta_c = \sin^{-1}\left(\frac{n_2}{n_1}\right) \tag{2.2}$$

When the angle of incidence is greater than the critical angle, the incoming light completely reflects from the interface and it travels into the same medium with no loss of intensity. Figure 2.3 schematically depicts the total internal reflection phenomenon in a fiber structure.

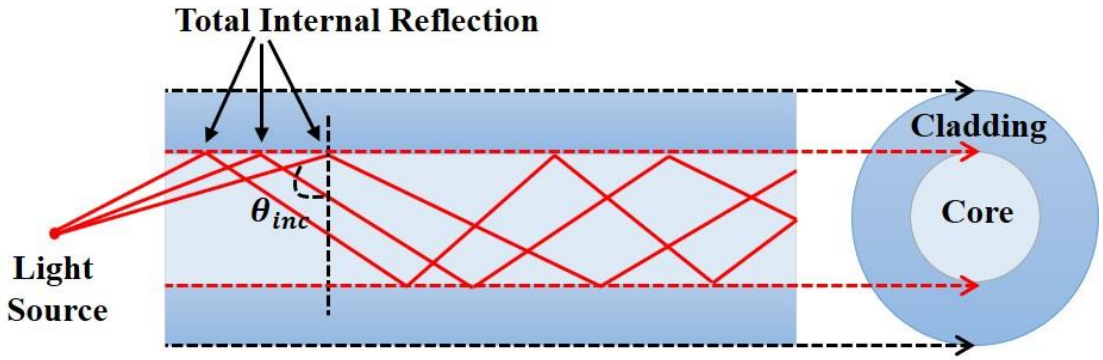

Figure 2.3. Total internal reflection ($\theta_{inc} > \theta_c$) in fiber structure.

Another important parameter so called the Numerical Aperture (NA) shows the ability of an optical fiber to confine the incoming light inside the fiber core [44]. NA is demonstrated by the following formula:

$$NA = \sin\alpha = \sqrt{{n_1}^2 - {n_2}^2} \tag{2.3}$$

where α is the acceptance angle. α is defined as the maximum half angle of the acceptance cone which is demonstrated in Figure 2.4 [45]. As it is seen from the formula, acceptance angle is related to the NA. If NA is known, it is trivial to determine the acceptance angle. Furthermore, for a fiber structure, if both the NA value and the refractive index of the core (or cladding) are known, the refractive index of the cladding (or core) can be calculated.

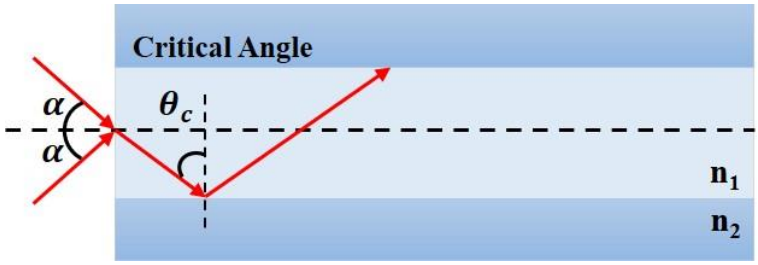

Figure 2.4. Critical and acceptance angle.

The fractional refractive index difference between core and cladding region is another crucial parameter in fiber optics and it is given by the following formula [46]:

$$\Delta = \frac{n_1 - n_2}{n_1} \tag{2.4}$$

While this parameter value is greater than zero in the presence of TIR condition, for effective light guiding mechanism along the fiber, it should also be less than 1 [46].

Up to now, the review part briefly introduced the physical mechanism behind the propagation of light inside the fiber core. The following sections in review part will be devoted to the types of optical fibers and fiber optic sensors.

2.3. Optical Fiber Types

Mainly, optical fibers are classified into two main categories and each of which has two subcategories depending on their properties such as diameter and refractive index profile, which is seen in Figure 2.5.

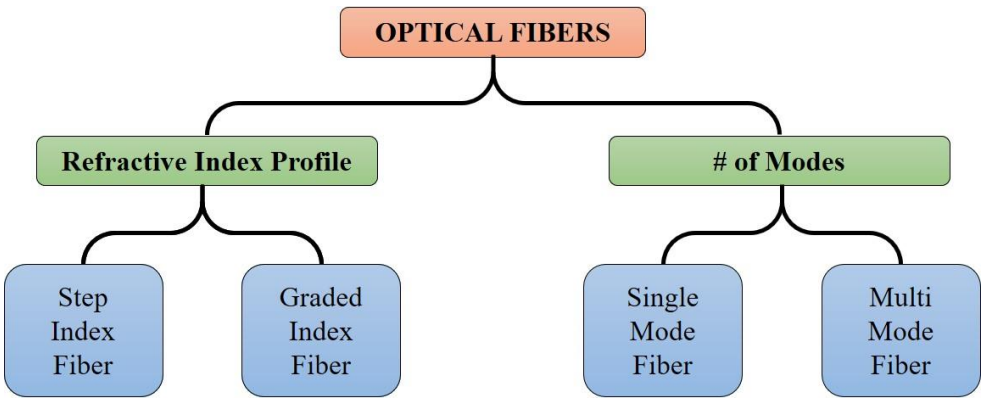

Figure 2.5. Classification of the optical fibers.

In an optical fiber, light propagates through the fiber core following different light paths which are called as ‘modes’. Early studies showed that fine adjustment of core diameter allows certain number of modes to propagate through the optical fiber [46]. Thereby, the number of permitted modes for propagation is used as a classification method of optical fibers: single mode and multimode optical fibers.

2.3.1. Single Mode Optical Fibers (SMF)

As it is stated before, optical fibers are classified depending on their core diameters, because it restricts the number of modes which propagates along the optical fiber [46]. Here, the single mode optical fibers possess cores with narrow diameters which are typically ranging from 8.3 to 10 µm in a cladding region with a diameter of 125 µm ($d_{core}/d_{cladding}$ is ranging from 0.066 to 0.08) [47]. In this type of fiber structures, only one mode can propagate. Another way of permitting only one mode to be coupled into the fiber core is to tune the wavelength of incident beam. For example, operation wavelength of a typical single mode fibers with 8.3 to 10 µm diameter is varied from 1310 nm to 1550 nm [48]. Since single mode optical fibers are operated with a laser source, they still function for long distances with very high reliability [49]. Additionally, the refractive index difference of cladding and core region (Δ) is very small. Figure 2.6 shows the basic structure and cross section part of a single mode fiber.

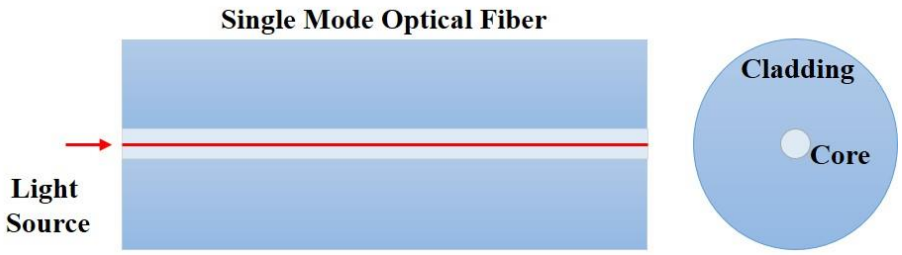

Figure 2.6. Single mode optical fiber.

2.3.2. Multimode Optical Fibers (MMF)

As it is compared with the single mode fibers, multimode optical fibers have larger core diameters which range from 50 µm to 85 µm in a cladding region with a diameter of 125 µm ($d_{core}/d_{cladding}$ is ranging from 0.4 to 0.68) [49]. In these particular multimode optical fibers, the core diameters are larger than that of the single mode fiber. On the other hand, an upscaled dimensions of multimode optical fiber system which has a core diameter of 100 µm in a single cladding with a diameter of 140 µm is also used in some applications in harsh environments including military and specified network applications [46]. The ratio of core

and cladding diameter is still almost one order of magnitude larger than that of single mode fibers ($d_{core}/d_{cladding}$ =0.71).

In this type of fiber structures, multiple modes can propagate. Unlike the single mode fibers, these fibers operate for shorter distances. Their typical operation wavelengths range from 850 nm to 1300 nm [49]. The refractive index difference between cladding and core region is also larger than that of the single mode optical fibers. Figure 2.7 indicates the schematic representation of a multimode fiber and its cross section. Because of the large core size of the multimode fibers, low cost light sources can be used such as light-emitting diodes (LED) and vertical cavity surface-emitting lasers (VCSEL) [50].

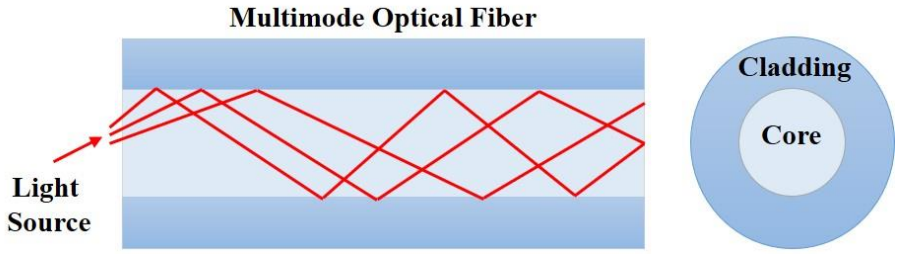

Figure 2.7. Multimode optical fiber.

To sum up, there is a tradeoff between working distance, fiber core diameters, and operating light source. A low-cost light source may significantly decrease the working distance, provided that the selected optical fiber has larger core diameter. On the other hand, high-cost laser sources work in considerably longer distances, but the selected optical fiber should have a smaller core diameter.

The second classification method of optical fibers rests on refractive index profiles of their cores. The refractive index profile can be either uniform throughout the fiber core or gradually increased from outer to inner part of the fiber core (i.e., radial direction). Depending on refractive index profiles of cores, there are two types of optical fibers: step index and graded index optical fibers. As graded index optical fibers are the multimode optical fibers, step index fibers can be single or multimode optical fibers.

2.3.3. Graded Index (GRIN) Optical Fibers

Refractive index of the fiber core gradually changes along radial direction which takes maximum value at the center of the fiber core. Figure 2.8a and b present the cross section of a graded index optical fiber and its refractive index profile along radial direction, respectively. For a multimode graded index fiber, the core diameter can be approximately 50, 62.5, 85, and 100 μm [44]. As seen from the Figure 2.8c, light path in a multimode graded index optical fiber has a helical shape. In physics, attenuation is known as the gradual loss of intensity through a medium [40]. Moreover, attenuation for multimode graded index is less than multimode step index fibers.

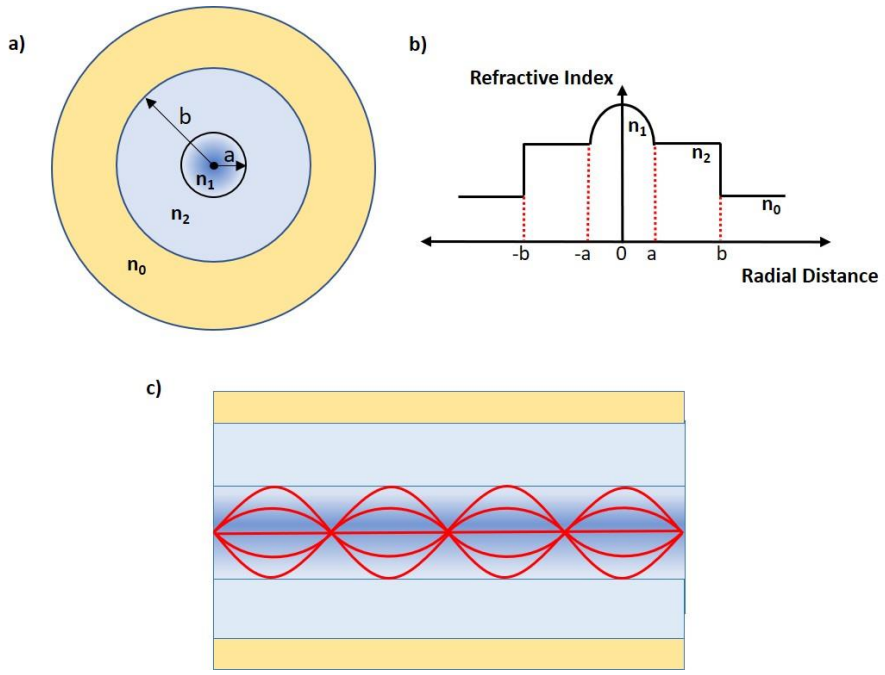

Figure 2.8. (a) Cross section and (b) side view of a graded index optical fiber and its refractive index profile. While light yellow color region shows the cladding, blue colored region is core region. (c) The gradual increase in the darkness of blue color is the representative of graded refractive index.

2.3.4. Step Index Optical Fibers

In step index fiber type, the fiber core and cladding regions have uniform and constant refractive index value. Unlike graded index fiber type, in the step index fiber, the refractive

index does not change in the radial direction and the refractive index value sharply increases at the boundary and become constant in the cladding region (n_2), as well. The schematic representation of a step index optical fiber and its refractive index profile is illustrated in Figure 2.9a and b. Due to the sharp change in the refractive index at intersection/boundary of core and cladding, the light path for a step index fiber does not bend and therefore, the beam path draws a zigzag pattern when it reflects off from the intersection by conforming the TIR rule which is seen from Figure 2.9c. The typical refractive index of the core for step index fiber ranges from 1.44 to 1.46 [46]. The standard diameter of core and cladding ratio (2a/2b) is 8/125 for single mode step index optical fibers and 50/125, 62.5/125, 85/125, and 100/140 for multimode step index optical fibers [46]. The fractional refractive index difference varies from 0.001 to 0.02 ($\Delta \ll 1$) [46].

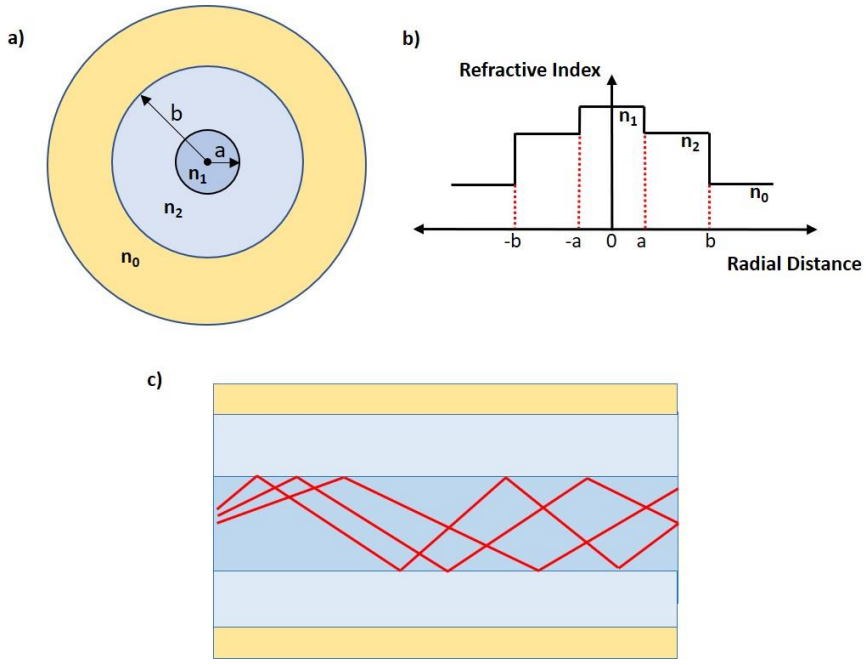

Figure 2.9. Schematic representations of (a) cross section (c) lateral side views of a step index fiber and b) its refractive index profile, the blue, light blue, and yellow colored sections show core, cladding, and jacket parts of fiber.

Up to now, the optical fibers are classified as a function of both the diameter and refractive index profile of cores. The number of the cores in a single fiber leads to another classification according to the number of cores: single and multicore fibers.

2.3.5. Single Core (SCF) and Multicore Optical Fibers (MCF)

If an optical fiber has only one core, this fiber structure is called as single core optical fiber (SCF). Multicore optical fibers (MCF) have more than one core in a single common cladding. Depending in demand in experiments, the number of cores can be increased in a single cladding. With the advent of multicore fiber fabrication, fiber optic field diversify its utilization in many different fields especially sensing applications and biological and medical imaging [51]. Detailed classification of MCFs can be seen from Figure 2.10 [51]. Depending on the material properties, there are two types of multicore fiber: Solid and holey MCFs [52]. The solid MCFs have a single cladding with slightly different refractive indices in which all cores are embedded into this cladding. For the case of holey MCF, the fiber is made of photonic crystal fiber (PCF) which consists of hexagonal array of holes. Additionally, MCFs can be either weakly coupled or strongly coupled. Such classification occurs because of the distance between cores.

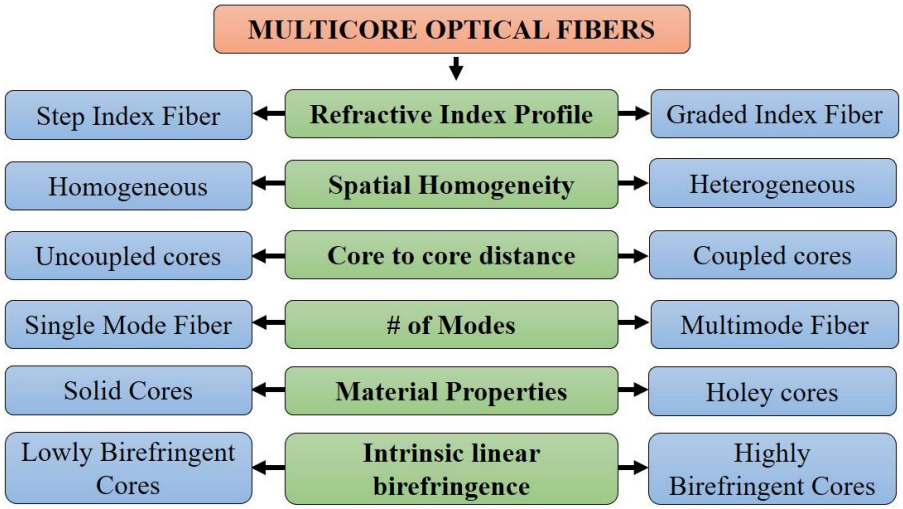

Figure 2.10. Classification of multicore optical fibers.

Moreover, the strength of crosstalk/communication between individual cores increases with the decrease in the distance between cores. If the strength of cross talk is weak or strong the fiber is called as the weakly coupled MCF or strongly coupled MCF, respectively. Weakly and strongly coupled four core optical fibers and their core distances can be seen from Figure 2.11c and d.

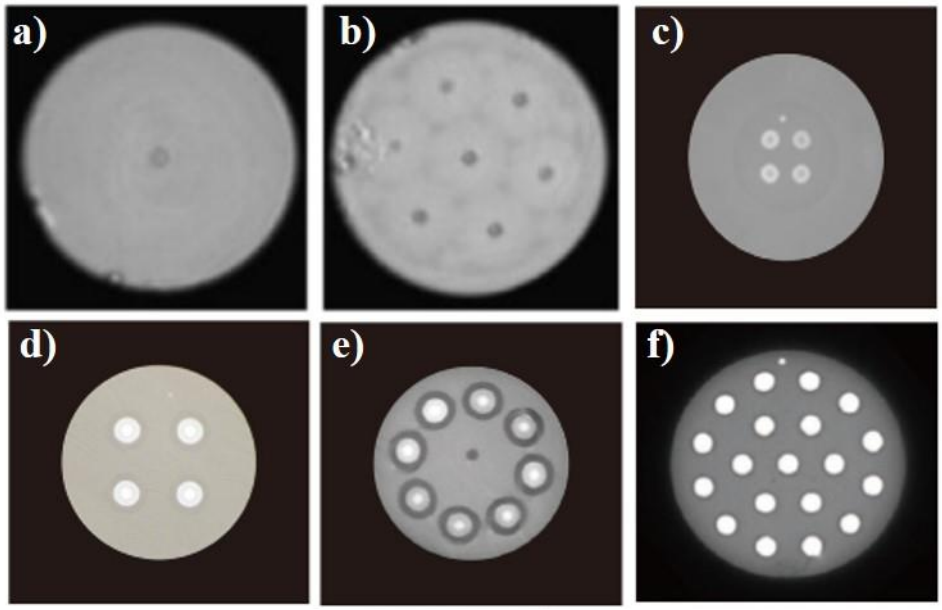

Figure 2.11. (a) single core, (b) seven core, (c) strongly coupled four core, (d) weakly coupled four core, (e) eight core, and (f) nineteen core optical fiber [53, 54].

2.4. Optical Fiber Applications

Optical fibers have had an important place in numerous and different technological applications and industries such as telecommunication systems, spectroscopy, biomedical sciences, medical imaging such as endoscopes and laparoscopes, and military (aircrafts, ships, tanks, nuclear testing applications etc.) [55]. Due to their unique properties like compact size, high sensitivity, electrical insulation, light weight, simplicity in signal detection, flexibility, low cost, immunity to electromagnetic interference, easy maintenance, and work over long distances, they have a great potential for sensor applications [56].

The main working mechanism of the FOSs is based on the variation in the intensity, phase, or wavelength of the light introduced by the external perturbations [2]. By using different configurations and types of optical fibers, many physical parameters such as temperature, heat, refractive index, strain, stress, pressure, deformation, vibration, acceleration, displacement etc. can be detected with a high sensitivity and accuracy, easily. In general, interferometric methods which are used in sensing experiments can be categorized into 3 subtitles and it is listed as in Figure 2.12 [5].

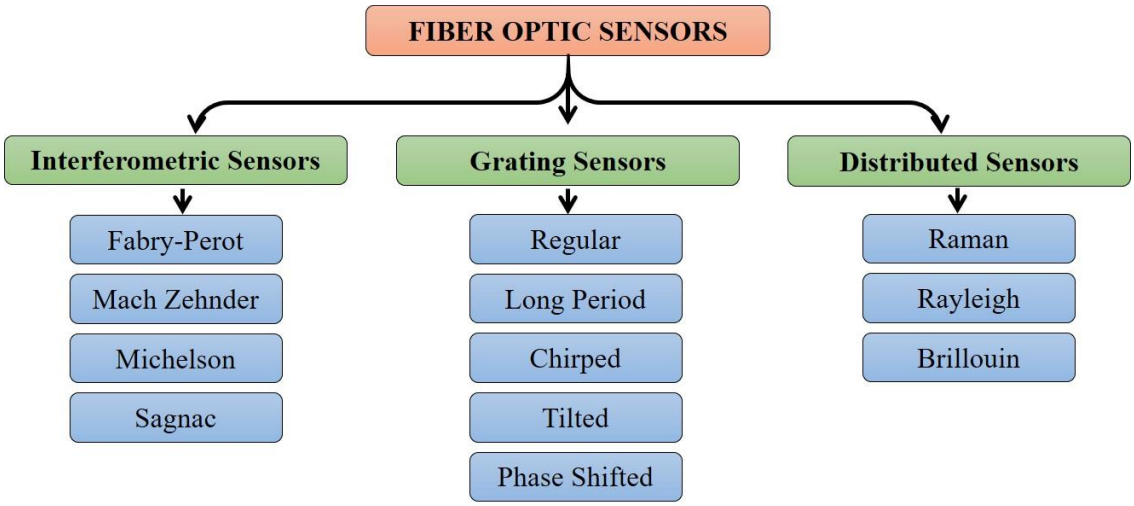

Figure 2.12. Classification of fiber optic sensors.

2.4.1. Interferometric Fiber Optic Sensors (IFOS)

Interferometry is a precision metrology which is based upon the phenomenon of the interference of two or more light beams [57]. Interferometers are used to determine and measure many physical parameters such as displacement, temperature, pressure, refractive index, and strain [58].

Depending on fabrication processes, operating principles, and application fields, interferometric methods are categorized into four types: Michelson, Mach Zehnder, Fabry-Perot, and Sagnac [5].

2.4.1.1. Fabry Perot Interferometer (FPI)

In general, Fabry Perot Interferometer (FPI) is an optical cavity which consists of two parallel reflecting surfaces which is schematically displayed in Figure 2.13. FPI is also called as etalon. Interference pattern is formed because of the reflected and transmitted lights from two parallel surfaces (mirrors). FPI was discovered by Charles Fabry and Alfred Pérot in 1899 [59, 60].

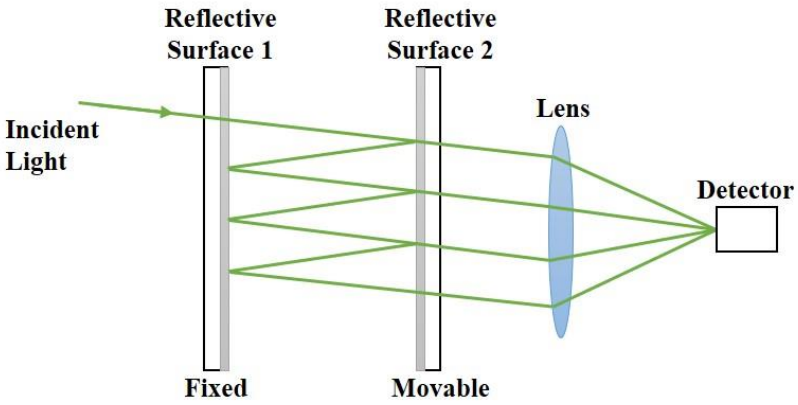

Figure 2.13. Schematic representation of Fabry Perot Interferometer.

Depending on their fabrications process, fiber based FPIs can have extrinsic or intrinsic cavities [5]. The difference between those two cavities related to the location of the cavity. While the extrinsic FPI sensors utilize reflections from the cavity, which is generated outside of the optical fiber, the intrinsic FPI sensors however utilize reflections inside the optical fiber structure [5]. Figure 2.14a and b show lateral view of fiber structures based on intrinsic and extrinsic FPI sensor, respectively.

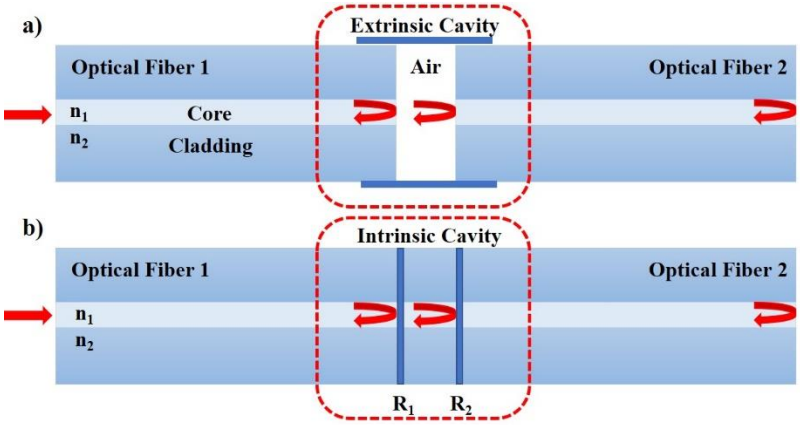

Figure 2.14. Schematic representations of fiber-based (a) extrinsic and (b) intrinsic Fabry Perot Interferometers.

For extrinsic FPIs, fabrication process is easy and does not require sophisticated mechanism therefore it is cheaper as it is compared with the intrinsic FPI system. Obtaining a high finesse fringe pattern is possible as highly reflective surfaces are utilized in the

experimental set up for extrinsic FPIs. However, low coupling efficiency and alignment problems can be listed as some of the disadvantages of this type of FPIs.

On the other hand, there are many methods such as thin film coating [8], fiber Bragg grating [61], and etching process [62] to achieve fiber based intrinsic FPIs. Since the cavity is inside the optical fiber, there is no alignment problems for these types of interferometers. Thus, light intensity losses due to the slight misalignment problems are eliminated in this method. However, the costly fabrication process can be counted as the drawback of such FPI system.

Although there are similarities between advantages of FPI sensors and the other type of FOSs, the property of having a sensing head at the tip of the optical fiber which provides to embed it in biological tissues and small volumes brings FPI sensors into greater prominence among the other sensor types [63]. Fiber optic based FPIs have been used in numerous experimental and theoretical studies for detection of many parameters such as ultrasound and imaging [64, 65], humidity [66], salinity [67], temperature [68], refractive index [63], and pressure [69, 70].

2.4.1.2. Mach Zehnder Interferometer (MZI)

The Mach–Zehnder interferometer (MZI) was discovered by Ludwig Mach and Ludwig Zehnder in 1892 [71, 72]. As seen from Figure 2.15, working principle of this interferometer is based on the path difference of the two beams. Light beams from the same source travels different distances and their interferences form the main working mechanism of MZIs. This interferometric system includes a light source, two beam splitters, two mirrors, and detectors.

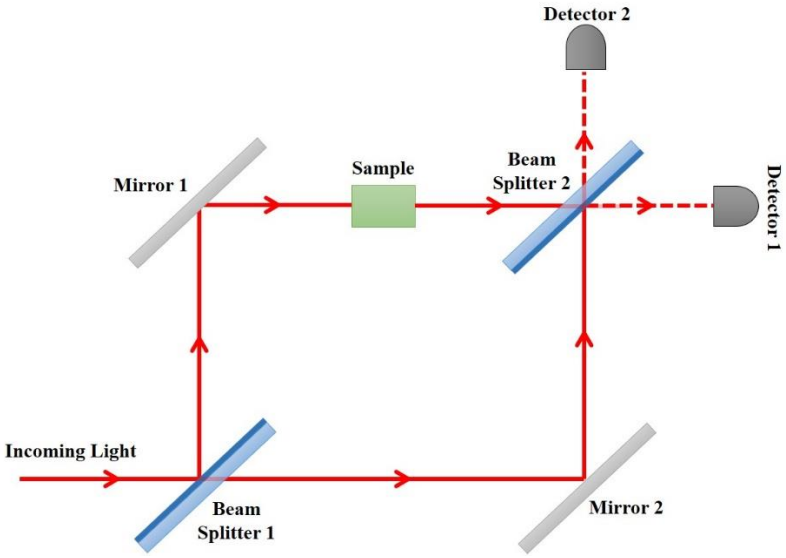

Figure 2.15. Schematic representation of Mach Zehnder Interferometer.

Using the first beam splitter, incoming light is split into two beams and they are reflected by two mirrors. Reflected beams are recombined by the second beam splitter and are sent onto photodetectors. The MZIs employs a phase shifter or a sample on one of the optical paths after the first beam splitter in order to intensify the phase shift (see Appendix 1) [73].

In a conventional fiber based MZI, the interference pattern is obtained by employing two single cores with single mode optical fibers. As it is displayed in Figure 2.16, while one of these fibers is employed as a reference optical fiber, the other optical fiber is used as the sensing optical fiber where the external parameters are subject to a change so that a path length different occurs. In other words, the external physical parameters such as temperature, pressure, vibration, and strain are applied to the sensing optical fiber however, reference optical fiber (reference arm) is isolated from the changes. This causes an optical path difference between two beams which is detected by the photodetector.

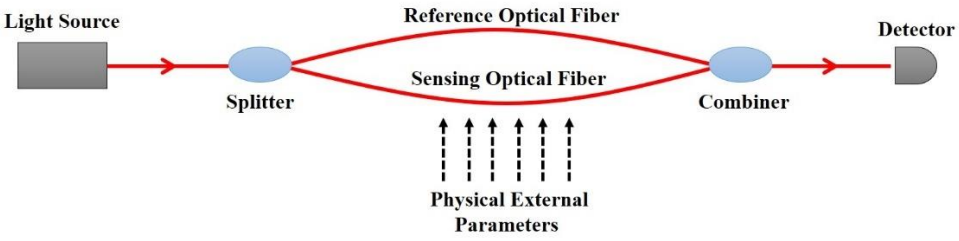

Figure 2.16. Schematic illustration of a basic fiber-based Mach Zehnder Interferometer.

There are various methods to obtain fiber based MZI sensors by using different configurations of the optical fibers such as combination of multimode and single mode optical fibers, core mismatch, fiber tapering, and small core with single mode optical fiber sandwiched between two regular single mode fibers [5]. Some of these configurations can be seen from Figure 2.17.

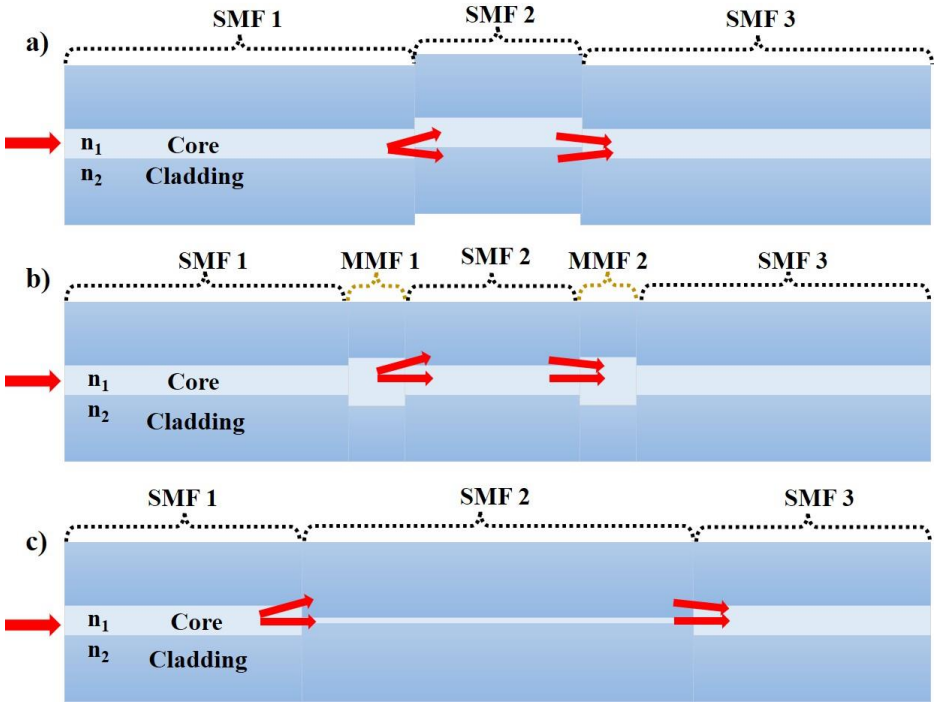

Figure 2.17. Schematic representations of some types of MZI. (a) core mismatch, (b) two MMF segments, and (c) small core SMF is sandwiched between two SMFs.

Due to their flexible and simple configurations, fiber based MZI sensors are utilized to detect and measure many physical and chemical parameters with very high sensitivity. One of the simplest and the most fundamental studies on fiber based MZI sensors was

reported by G. Hocker in 1979. In this research, an interference pattern in transmission scheme is formed by two single core optical fibers. By applying temperature to one of the optical fibers, a phase shift in interference pattern occurs due to both the temperature induced refractive index change and the thermal expansion of the fiber core. Recently, fiber based MZI sensors in different configurations listed above have attracted great attention and have been preferred to detect various physical parameters with high sensitivities, such as temperature [74-77], strain [78], pressure [79], and refractive index change [80, 81].

2.4.1.3. Michelson Interferometer (MI)

Michelson interferometer (MI) was invented by Albert Abraham Michelson in 1887 and well known in the Michelson–Morley experiment [82]. The working principle and fabrication process of this interferometric method is similar to MZI. One of the most popular and successful MI configurations was achieved in famous The Laser Interferometer Gravitational-Wave Observatory (LIGO) experiment which made it possible to observe gravitational waves for the first time, in 2015 [83].

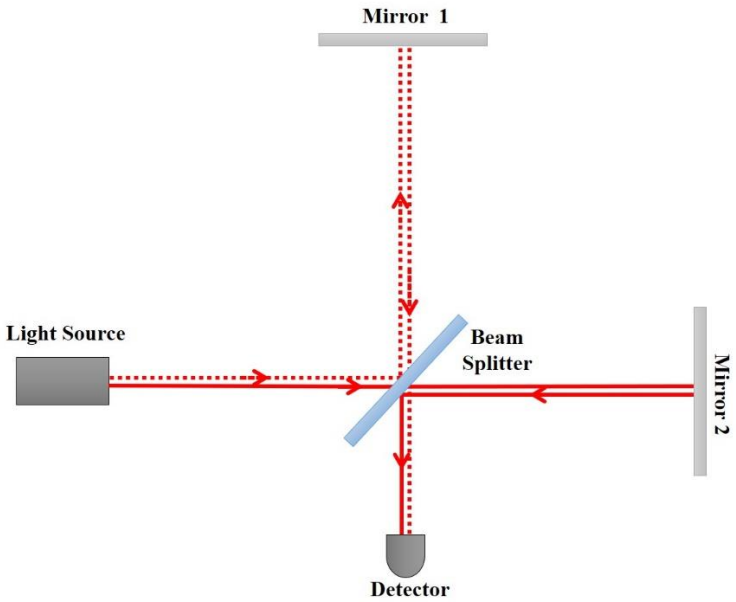

Figure 2.18. Schematic representation of Michelson Interferometer.

The basic structure of MI consists of one beam splitter, two mirrors, and a light source as it is seen from Figure 2.18. Incoming light is split into two beams and these beams

are reflected from the two mirrors. An interference pattern is formed and directed to the photodetector. The schematic representation of a basic fiber-based MI is shown in Figure 2.19. Incoming light from a laser source is split into two beams, each light is reflected from mirrors, and interference pattern is sent onto photodetector. If an external disturbance is applied to sensing optical fiber, a shift in the interference pattern is observed.

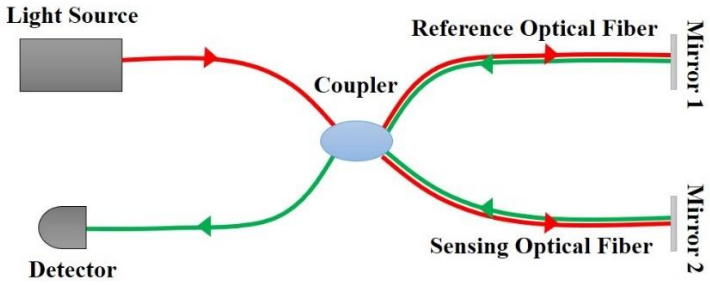

Figure 2.19. Schematic illustration of a basic fiber-based Michelson Interferometer.

Two different MI configurations: core mismatch and SMF-MMF combination are schematically shown in Figure 2.20a and b, respectively. In the literature, such hybrid fiber systems were utilized, and their extreme sensing abilities were reported. For instance, temperature [84], flow velocity [85], pressure [86], and refractive index changes in liquids [9] are among some of the external parameters which can be detected with very high accuracy by using aforementioned optic fiber systems. It is worth noting that there are some differences between MZI and MI based sensors. While MI method in especially sensing applications includes mirrors, MZI operates in a transmission mode therefore mirrors are eliminated from the optical set up. Another distinct difference is the number of couplers. As MI based FOSs include one coupler to split the incoming laser light and recombine the beams, MZI based FOSs have two couplers.

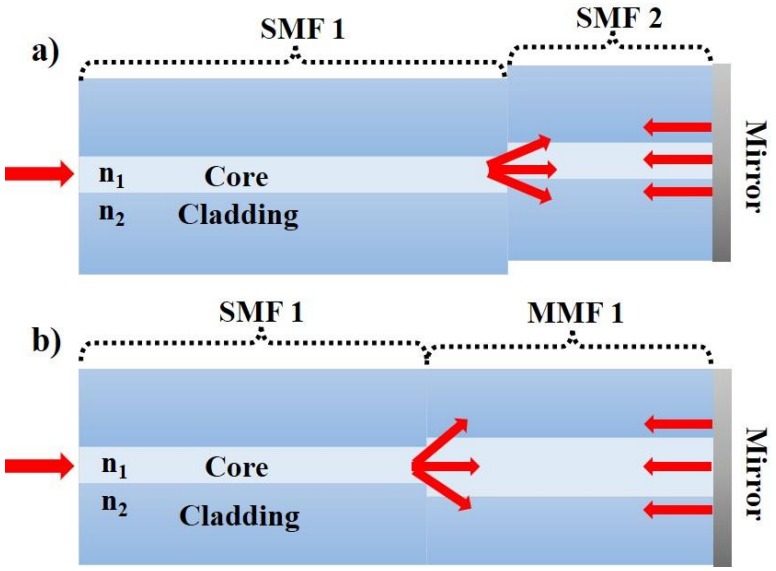

Figure 2.20. Some MI configurations. (a) core mismatch and (b) SMF-MMF combination.

2.4.1.4. Sagnac Interferometer (SI)

Sagnac Interferometer (SI) is one of the most important interferometric configurations which includes many unique properties such as simple design, low cost, and simple structure. In addition to the theoretical investigations, the first experimental study of SI was performed by Georges Sagnac in 1913 [87, 88].

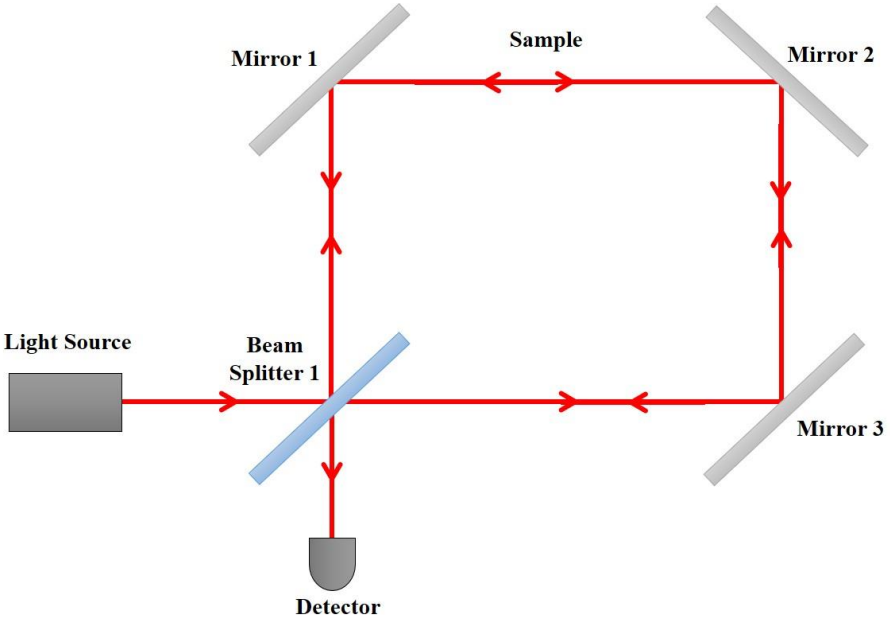

Figure 2.21. Basic configuration of Sagnac Interferometer.

Figure 2.21 shows the SI optical set up. While the laser is split into two beams by using a beam splitter (or half-silvered mirror), each beam is reflected from mirrors and follows a single path in opposite directions. Thus, an interference pattern occurs, and it is detected by the photodetector.

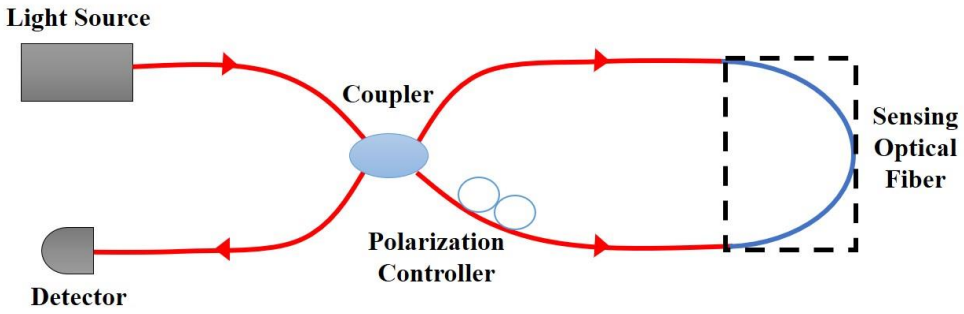

Figure 2.22. Fiber based Sagnac Interferometer configuration.

In Figure 2.22, the schematic representation of a fiber-based SI sensor which consists of an optical fiber loop, a laser, detector, coupler, and polarization controller is shown. The working principle of SI is different from the other interferometric methods. Incoming laser light is split into two beams by using coupler. Optical path difference is related to the polarization dependent wave propagation speed which travels throughout the optical fiber loop. Pressure vector sensor [89], refractive index [90], and temperature [91, 92] can be given as some examples of studies which employ SI configuration in their sensor structure.

2.4.2. Fiber Bragg Gratings (FBG)

In 1978, K. O. Hill et. al. reported the first investigation regarding the fiber Bragg grating (FBG) [15]. In this research, the presence of photosensitivity of Ge doped fiber cores were demonstrated. Intense laser light induced permanent refractive index changes in the fiber core was the evidence of the high photosensitivity in the fiber cores.

Fiber Bragg Gratings are fabricated by exposing the fiber cores to a periodic pattern of an intense laser light. This results in a permanent periodic variation or increase in the refractive index of the fiber core(s). Each region or surface with a higher refractive index serves as an internal mirror and a small amount of incident light is reflected from these

surfaces. As a result of this, reflected lights combine in a large reflection at a particular wavelength which is called as ‘Bragg Wavelength’ which is shown in Figure 2.23.

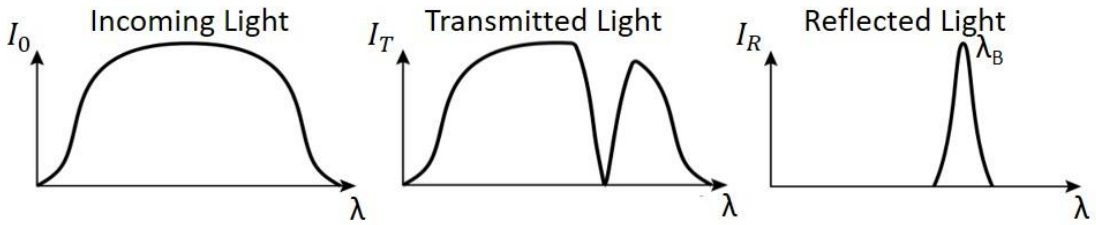

Figure 2.23. (a), (b), and (c) show the incoming, transmitted, and reflected intensity [93].

In general, sensors, optical fiber mode converters, wavelength selective filters, optical communication systems, structural health monitoring, acoustic sensing, aerospace, medical applications, nuclear power industry (especially, strain, temperature, and displacement are monitored in thermonuclear reactors), spacecraft monitoring, wind blade monitoring, and stress monitoring in airplane fuel tanks can be given some examples of FBG applications [94].

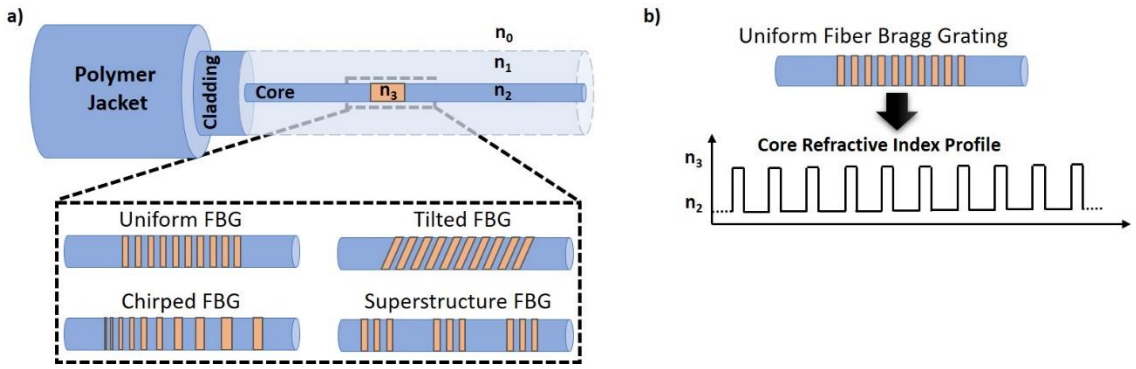

Figure 2.24. (a) The schematic representation of uniform, tilted, chirped, and superstructure FBGs and zoom in section is where the exposure of laser on that particular region caused irreversible refractive index change. Bright orange sections are where the refractive index changed. Depending on the patterns the Bragg grating type changes. (b) The refractive index profile of a uniform FBG.

Depending on the properties and specifications of phase mask used in FBG writing process, one can generate different patterns on fiber cores. A few examples to such patterns can be listed as uniform, tilted, phase shifted, chirped, and superstructure. Figure 2.24 shows the schematic representation of those types of FBGs. Figure 2.24b shows the corresponding refractive index profile of a uniform FBG.

Using different types and combination of FBGs, many physical and chemical parameters such as refractive index [95], temperature [96], pressure [97], and strain [98] can be determined, and they can adapt to many different and harsh environments.

2.4.3. Distributed Fiber Optic Sensors (DFOSs)

The basic working principle of a distributed fiber optic sensor (DFOS) is based upon the light scattering from an impurity exist in the core section of the optical fiber [99]. The optical fiber is used as a sensing structure and given as an example of intrinsic optical fiber sensors. Such mechanism is employed in various detection studies including temperature, strain, and vibration etc. [99].

Rayleigh scattering is an elastic scattering process which is caused by the local refractive index changes because of the heterogeneity and density fluctuations of the fiber structure. Figure 2.25 illustrates the schematic representation of Rayleigh scattering in optical fibers.

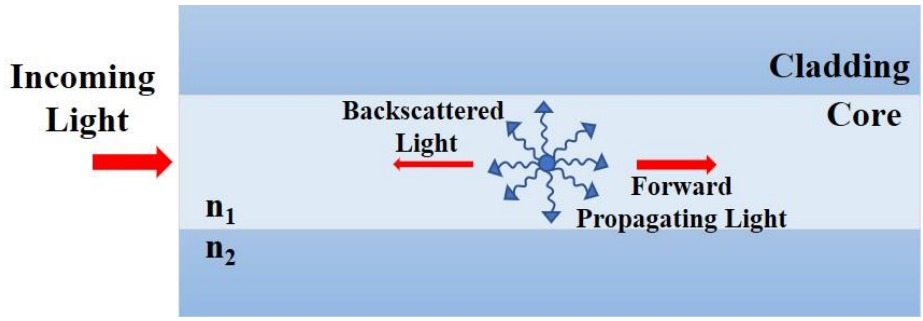

Figure 2.25. Rayleigh scattering in optical fibers.

A small portion of light is scattered from these scattering points with different refractive indices and these points behave like a weak reflector which reflects the incoming light in all directions. Unlike Rayleigh scattering, Brillouin and Raman scatterings are inelastic. Raman scattering occurs due to the molecular vibrations. The incoming light interacts with electrons of vibrating molecules and is scattered. Depending on the resonance frequency of the lattice oscillation, a shift in the frequency occurs. Lastly, Brillouin scattering is based upon the interaction between the incident light and thermally induced material-density fluctuations. It is understood that each DFOS has a different working principle and they have been used to detect various physical parameters [100-103, 37].

2.5. Discussion

By the advent of laser and optical fiber technologies, highly sensitive fiber optic sensors to detect different physical parameters have attracted enormous interest due to their unique, simple, and flexible design properties. This led the quick establishment of theory and therefore the experimental fabrication techniques/protocols which further broaden the research impact area. Nowadays, in addition to the next generation and highly sensitive sensor applications, fiber optics technology has frequently been utilized in communication systems, data transmission, and bio-medical imaging fields.

Fiber optical sensors which are one of the most common and important application areas of optical fibers have great potential in many different fields with numerous configuration and combinations. They can detect various external physical parameters such as temperature, heat, rotation, pressure, refractive index, strain, stress change, displacement, vibration, polarization, humidity, linear and angular position, viscosity, etc. with very high efficiency. Small size, longer lifetime, simplicity, high sensitivity and accuracy, design, low cost, high flexibility, durability, low propagating loss, immunity to electromagnetic interference, and reliability in signal detection can be listed as some of the unique and remarkable features of fiber optic sensors. All fiber optic sensor types including interferometric, grating based, and distributed types can operate in harsh and high voltage environments and they do not need any additional protection.

Developing technology has enabled to fabricate many special types of fiber structures and experimental studies in fiber optic sensing applications have become less complicated. As mentioned before, while the first fiber optic interferometric methods such as Mach Zehnder and Michelson interferometry included multiple number of optical fibers, in recent years, the same working principle or the sensor structure has generated by combining different types of optical fibers into only one optical sensing element with compact size or utilizing different optical components such as internal mirrors and fiber Bragg grating.

All these interferometric and grating based sensing methods listed above can be applicable to single or multicore optical fibers. To use single and multicore optical fibers in sensing applications brings some advantages and disadvantages. The increase in the number of optical fibers and equipment used in sensing experiments results in some alignment and adjustment problems. Interference pattern which is generated by the multiple numbers of single core optical fibers can be affected external fluctuations, easily. These disturbing factors can also change the distance between the fibers ends with respect to each other which results in a poor and unstable interference pattern. Multicore fibers have a fixed core separation which provides a stable interference pattern. As it is understood that utilization of multicore fibers in interferometric sensing applications has many advantages.

Fiber Bragg grating writing process into multicore fibers is more difficult than that of the single core optical fibers. Because different locations of the optical fiber cores relative to the intense laser light can cause some differences in the interference pattern of each core. In other words, the curvature shape of the fiber surface may lead to a non-uniform intensity distribution of the UV laser. FBG writing process into single core optical fibers does not have these kind of fabrication problems. On the other hand, after a successful FBG writing fabrication process is carried out into multicore optical fibers, each fiber core behaves like an individual sensor. As some of the cores are used as reference optical fiber cores, the rest can be introduced as sensing optical fiber cores.

3. FOUR-CORE OPTICAL FIBER AS A CALORIMETRIC GAUGE

3.1. Introduction

Fiber optic interferometry is one of the most promising instrumentation branches in the area of the optical sensing. Design elegancy, reliability, robustness, simplicity in the signal detection scheme, and the cost are a few remarkable features to mention about a newly proposed fiber optic interferometric sensor to become a preferable alternative device for the measurand in concern.

A numerous successful work has been reported for detecting various temperature ranges and highly sensitive heat transfer measurements. In almost all of these interferometric sensors, the intrinsic properties of single-mode-single-core optical fibers are used as the sensing mechanism. For example, two single mode optical fibers were employed to detect temperature and pressure variations separately by Hocker [6], which allowed investigating heat transfer studies. A miniature single-mode fiber optic Fabry-Perot was demonstrated as a high-speed thermal sensor by Inci *et al.* [8], where the fiber optic cavity was axially exposed to the transient heat pulses. Nguyen *et al*. [13] showed that a multimode interference pattern arising from a suspended-core micro-structured optical fiber could be successfully utilized to detect temperatures up to 1000 ˚C.

In recent years, optical fibers with smart configurations have been preferred more and more in variety of experiments with growing device-making facilities, which allow widening the optical sensing technologies. A multicore optical fiber was employed for the first time by Gander *et al.* [10] for bending measurements. An optical sensor based on the temperature-induced change in the index of refraction of a two-core optical fiber inside a heater pipe was proposed by Romaniuk and Dorosz [12]. Yuan and Wang [11] demonstrated that a four-core fiber optic sensor had a capability to determine a relationship between the twisting angle of a four-core optical fiber and the rotated fringe pattern. It was also shown that such a sensor was insensitive to a temperature gradient.

In this project, a four-core optical fiber is described for the first time as a calorimetric gauge for heat transfer measurements. The objective of the work is to obtain heat transfer data through the temperature induced shift in the interference pattern of the four-core optical fiber at the far field upon applied heat pulses onto the distal end face of the fiber. Heat pulses from a Nd:YAG laser are aimed to be delivered only onto one of the four fiber cores axially (see Figure 3.2). The fiber core serves as a calorimetric gauge with an infinite length and preserves the accumulated heat supplied by a discrete laser pulse, which introduces a variation in the refractive index and fiber length, resulting in an optical path difference between the four-guiding fiber cores inside the single fiber cladding of 125 μm in diameter. The optical path difference between the four fiber cores is monitored through the shift in the constructed interference fringe pattern on reflection, which is recorded by a fast CMOS camera. The amount of accumulated heat along the penetrated fiber depth is measured from the phase shift of this interferometric system. The Fourier Heat Equation is used to successfully determine the amount of the accumulated heat, temperature change, and the total phase shift in the sensitive part of the four-core fiber, which is calculated to be about 2.8 mm from the fiber distal face [104]. The accumulated heat inside the targeted fiber core with laser heat pulses leads to a temperature increase. This property may be exploited to use a multicore fiber as an alternative temperature sensor as well. One of the unique features of this work is that the length of the four-core fiber is undoubtedly infinite when compared to the heat diffusion length, which enables no heat loss along the fiber core since any heat loss in the system causes unavoidable higher error rates in the measurements.

Two or more single mode optical fibers are usually employed in many related former works to produce an interference pattern, which may complicate the experimental setup and give rise to many alignment and unstable fringe problems. However, four fiber cores with fixed core separations within a single cladding form a stable and reliable fringe pattern. The fixed core separation also simplifies the coupling of the light into the cores, reduces the complexity of the experimental setup and needs no extra modifications to carve a device out of the given multicore fiber, for example, forming internal reflecting mirrors or constructing Michelson or Mach-Zehnder two beam interferometers. The device can be operated both in transmission and in reflection mode. Since there are no cavities in the addressing fiber to cause any temperature induced path imbalance and all four cores are exposed to the same thermal optical and the same thermal expansion effects, the device is insensitive to any

external thermal fluctuations. For example, no phase shift is observed even though the four-core fiber is heated up to 400 ˚C degrees prior to the experiment.

The layout of the project consists of the basic theory on the fringe pattern of a four-core optical fiber and heat induced phase shift between the four guiding cores, which is followed by the experimental results, discussion, and conclusion.

3.2. Theory

Since the invention of lasers and optical fibers in 1960s, many scientists have carried out a lot of experiments based on interferometric methods and theoretical studies to find some equations to define the effects of external parameters on the total phase shift [6, 12, 104, 46]. By using these mathematical equations, change in external factors such as pressure, strain, temperature, the amount of accumulated heat, and heat diffusion length can be calculated, easily. These changes result in a variation in the optical pathlength, which is defined as a product of the physical length of the path and the index of refraction of the medium where the light propagates.

Schematic illustration of the side view of a four-core optical fiber is described in Figure 3.1a. The intensity distribution of the fringe pattern formed by this fiber (see Figure 3.1b) on a topographical surface of height $z\,(x, y)$ is given by [105]

$$\begin{aligned} I(x,y) = 2I_0 \Big[& 2 + 2\cos\left(2\pi\frac{\delta}{\lambda f}(x\cos\theta - z(x,y)\sin\theta)\right) \\ & + 2\cos\left(2\pi\frac{\delta}{\lambda f}y\right) \\ & + \cos\left(2\pi\frac{\delta}{\lambda f}(x\cos\theta - z(x,y)\sin\theta + y)\right) \\ & + \cos\left(2\pi\frac{\delta}{\lambda f}(x\cos\theta - z(x,y)\sin\theta - y)\right)\Big] \end{aligned} \tag{3.1}$$

where I_0 is the intensity contribution of a single core, δ is the separation between two horizontal or vertical cores, f is the focal length of the lens, λ is the wavelength of the laser source, $z(x,y)$ is the out of plane displacement of the object surface, and θ is the illumination angle. This intensity distribution is used for the applications of the optical profilometry. However, in our case, the illumination angle $\theta = 0$, and the intensity of the fringe pattern on the CMOS camera with no surface topography, i.e., $z(x,y) = 0$, is reduced to

$$I(x,y) = 2I_0\left[2 + 2\cos\left(2\pi\frac{\delta}{\lambda f}x\right) + 2\cos\left(2\pi\frac{\delta}{\lambda f}y\right) + \cos\left(2\pi\frac{\delta}{\lambda f}(x+y)\right) + \cos\left(2\pi\frac{\delta}{\lambda f}(x-y)\right)\right]. \quad (3.2)$$

In our experiments, a four-core fiber is used to divide incident laser beam into 4 coherent beams. Therefore, vertical, horizontal, and diagonal fringe patterns occur due to the couplings of the guiding waves of the four cores. Figure 3.1 illustrates a four-core fiber structure together with its interferogram on transmission (or reflection). Vertical fringes are formed due to cores 1-2 and cores 3-4 couplings; and horizontal fringes are formed by cores 1-3 and cores 2-4 couplings. In addition to these, couplings of cores 1-4 and cores 2-3 produce diagonal fringes [105].

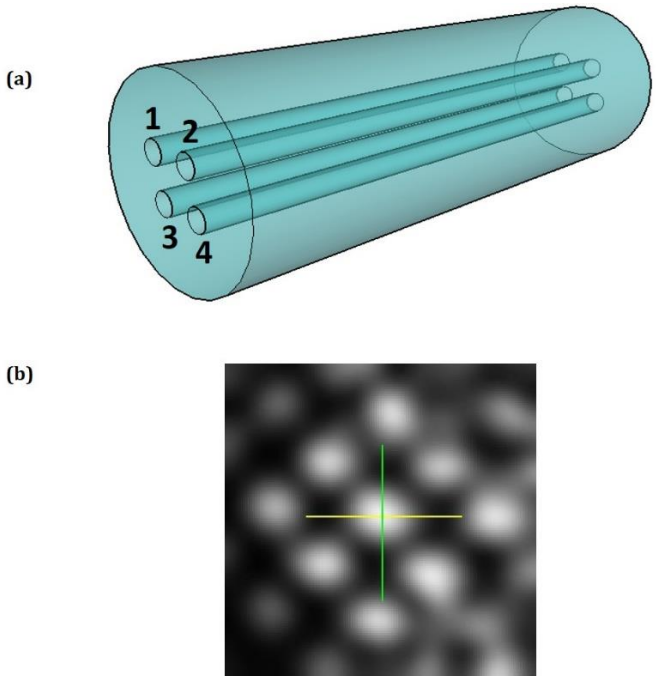

Figure 3.1. (a) Side view of a four-core fiber and (b) Interference pattern.

Since the total intensity distribution on the camera screen (see Figure 3.1b) described by Equation 3.2 is considered constant, the intensity distribution of the fringe pattern changes as a result of the phase shift. In general, this intensity distribution is expressed in terms of the phase as [8]

$$I(\varphi) \propto I_0(1 + V\cos\varphi) \tag{3.3}$$

where V is the visibility of the interference pattern, varying between the maximum and minimum output signals, which is given by

$$V = \frac{I_{max} - I_{min}}{I_{max} + I_{min}} \tag{3.4}$$

and

$$\varphi = \frac{2\pi nl}{\lambda} \tag{3.5}$$

where φ shows the phase, n is the refractive index of the fiber core, λ is the wavelength of the source, and l is the length of the sensitive part of the fiber.

When one of the fiber cores is exposed to the heat pulses as illustrated in Figure 3.2, the length of the fiber core and its refractive index experience a change due to the thermal expansion and the thermo-optic effects, respectively. These variations result in a path difference between this core exposed to heat and the other three ones, causing a phase shift, which is expressed as

$$\Delta\varphi = \frac{2\pi l}{\lambda}\left(\frac{n}{l}\frac{dl}{dT} + \frac{dn}{dT}\right)\Delta T \tag{3.6}$$

where $\Delta\varphi$ and ΔT are the average phase change and the temperature variation, respectively. For fused silica fiber used in our work, n=1.456, $\lambda = 632.8\,nm$, $dl/ldT = 5 \times 10^{-7}\,K^{-1}$, and $dn/dT = 10 \times 10^{-6}K^{-1}$ [6, 8].

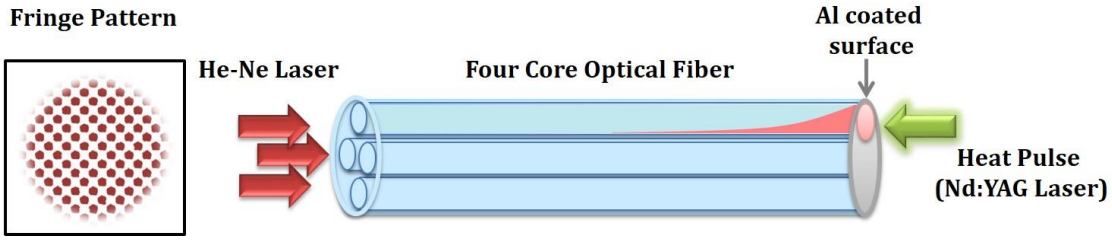

Figure 3.2. Working mechanism of the system.

The diameter of the fiber core also experiences a temperature change. However, the radial expansion in the diameter of the fiber core due to the temperature increase is much smaller than that of in the axial length. For example, for 40 mW laser heat pulse, the radial and axial expansions are determined to be ~4.81x10^{-6} μm and ~2.00x10^{-3} μm, respectively. Therefore, the effect of the radial expansion is considered to be negligible.

Equation 3.6 simply shows that the phase change is directly proportional to the temperature change. If one of the parameters is measured, the other one can easily be calculated. That is, one may calculate the temperature change within the fiber core if the phase shift is experimentally measured, and vice versa. Furthermore, $\Delta\varphi$ can be expressed as

$$\Delta\varphi = \varphi(T_0 + \Delta T) - \varphi(T_0) \tag{3.7}$$

where T_0 is the ambient temperature. Increase in the temperature is a result of one-dimensional heat transfer along the axial direction of one fiber core, which acts like a calorimetric gauge. It is assumed that the fiber length is almost infinite for heat to diffuse and a negligible amount of the heat is dissipated in the radial direction. The net heat flux is calculated using Equation 3.8 [8]

$$Q = (\rho c l)\frac{dT}{dt} = \left(\frac{\rho c}{k}\right)\frac{d\varphi}{dt} \tag{3.8}$$

where ρ is the density, c is the specific heat capacity of the fiber, and k is the thermal sensitivity, which is given by

$$k = \frac{2\pi}{\lambda}\left(\frac{n}{l}\frac{dl}{dT} + \frac{dn}{dT}\right)\Delta T. \tag{3.9}$$

The heat diffusion length along the fiber core in time *t*, which almost corresponds to the heat pulse duration from the Nd:YAG laser, is determined from Equation 3.10 as

$$d = \sqrt{\gamma t} \tag{3.10}$$

where γ is the thermal diffusivity, which is equal to $\sim 8.2 \times 10^{-7} m^2 s^{-1}$ for fused silica material. The diffusion length d is very important for constructing a heat sensor since the fiber length must be at least 4 times longer than the diffusion length, i.e., $l \geq 4d$, to safely assume that there is no heat loss [7]. In our case, diffusion length is about 0.71 mm with a pulse width of 0.6 s. In which case, the minimum fiber length is required to be 2.8 mm. However, our fiber length is chosen to be 400 mm, which is almost infinite when compared to 2.8 mm thermal diffusion length.

The relationship between the heat flow and temperature is given by Fourier Heat Equation below, which is a function of position and time. The equation also gives detailed information about the penetration depth of the heat too:

$$K\nabla^2 T(r,t) = c\rho\left(\frac{\partial T}{\partial t}\right) - Q(r,t) \tag{3.11}$$

where K is the thermal conductivity coefficient and Q is the heat transfer rate [7]. Since the heat flows in one dimension, the above Fourier Heat Equation is reduced to

$$\frac{\partial^2 T}{\partial x^2} = \frac{1}{\alpha}\frac{\partial T}{\partial t} \tag{3.12}$$

where $\alpha = K/C\rho$. The exact solution of this equation with respect to time and position is given by [104, 106]

$$T(x,t) = \frac{Q}{\rho c K}\left[\frac{2\sqrt{t}}{\sqrt{\pi}} e^{-\frac{x^2}{4\alpha t}} - \frac{x}{\sqrt{\alpha}} erfc\sqrt{\frac{x^2}{4\alpha t}}\right]. \tag{3.13}$$

According to Equation 3.13, different pulse durations lead to different temperature distributions and different heat penetration distances.

3.3. Experimental Setup

A four-core optical fiber, developed by HesFibel Ltd., Kayseri, Turkey, with a length of 40 cm is used in the experiment. Each core has a diameter of 10.6 μm with core separation of 40.6 μm. A single cladding of 125 μm surrounds the cores. Additionally, refractive index of the fiber cores is equal to 1.456.

At the initial stage of the experiment, both fiber ends are cleaved and one of the cross-sectional cleaved ends of the optical fiber is coated with a thin layer of Aluminum (Al) by thermal evaporation technique (NANOVAK-NVTH 350) to study a fringe pattern in the reflection configuration as illustrated in Figure 3.3.

In this experiment, two lasers are used: HeNe and Nd:YAG (532 nm, 150 mW, Coherent Compass 315M). HeNe laser is used to generate an interference pattern in the reflection mode while the Nd:YAG laser is used to produce heat pulses onto the chosen optical fiber core. The detailed schematic representation of the experimental setup is shown in Fig. 3. Firstly, HeNe laser at λ= 632.8 nm is aligned into the four cores of the fiber with a 10X microscope objective. Then, laser beam is reflected from the coated surface, which serves as a mirror at the cleaved fiber tip. A beam splitter is placed between HeNe laser and 10X lens to direct the reflected interference pattern onto a CMOS camera (OPTRONIS CR600X2). All images are taken with a resolution of 800x600 pixels.

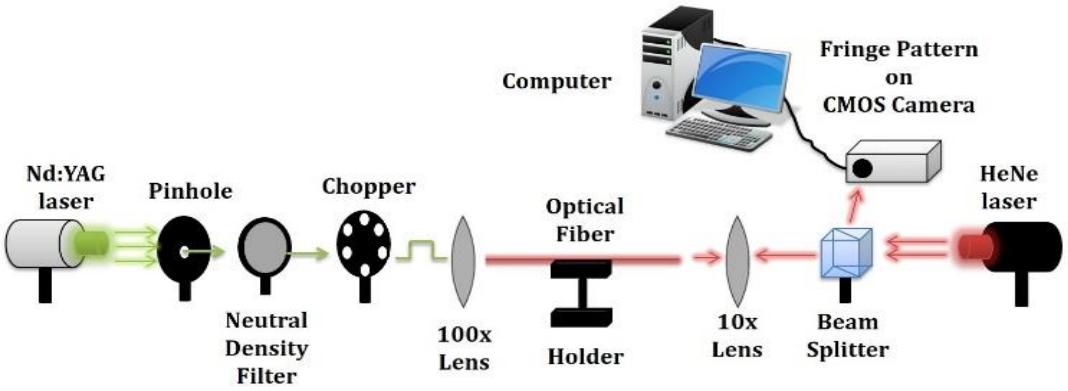

Figure 3.3. Schematic representation of the experimental set-up.

After a desired fringe pattern is obtained with the HeNe laser, using a 100X microscope objectives with NA of 0.7 and working distance of 1 cm, the Nd:YAG laser is

coupled carefully into the one of the fiber cores only from the Al coated distal end face of the four-core fiber (see Figure 3.2). A pinhole in front of the Nd:YAG laser is used to confine the beam diameter. A neutral density filter is placed before the pinhole to adjust the intensity of the Nd:YAG laser beam. A chopper is employed between the neutral density filter and the micro-positioner to obtain the Nd:YAG laser beam pulses of 600 ms duration with 10 s repetition rate, yielding a discrete pulsed heat source. Such a long repetition rate of the heat pulses is streamlined with the help of the chopper to enable enough time to the fiber core to heat up and then to cool down to its initial room temperature. This heating up and cooling down process is monitored through the shift in the reflection pattern shown in Figure 3.1b and is recorded with the CMOS camera. In other words, the fringe pattern would return back to its original place when the fiber core reaches its initial temperature upon cooling down process. The Nd:YAG laser is operated with average powers of 40 and 140 mW to heat the fiber core at different rates. CMOS camera is set to capture a number of frames during the heat induced phase shift, and then these frames are used to analyze the amount of the phase shift. A MATLAB code is written to obtain the intensity distribution of the frames. A cropped fringe pattern of a four-core fiber is given in Figure 3.1b.

Yellow and green lines on the selected fringe pattern indicate the intensity distribution of the points on two distinct directions. Using Pythagorean Theorem, two-dimensional average phase shifts are determined for each power value and are shown in Figure 3.4.

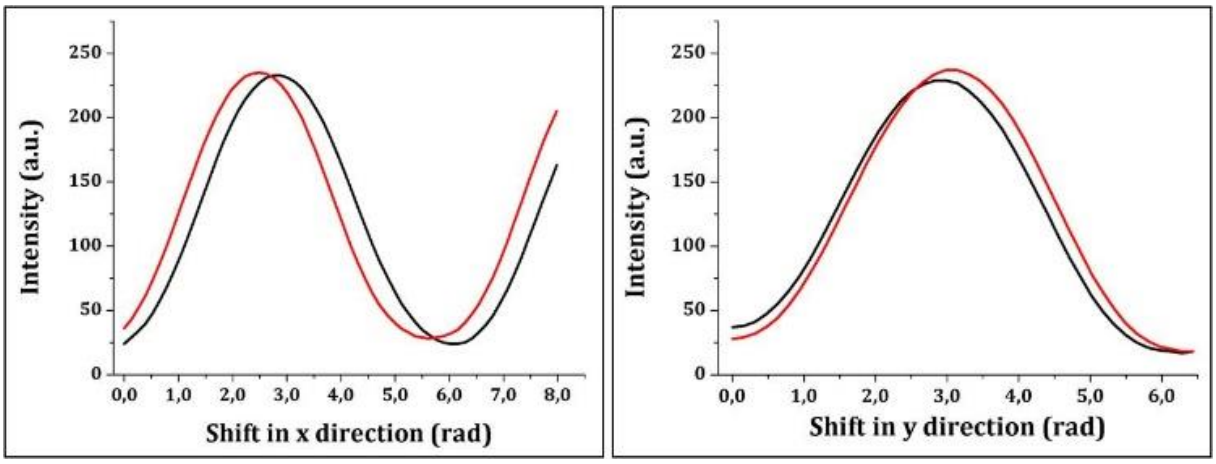

Figure 3.4. Phase shift of intensity distribution in x and y direction.

3.4. Results and Discussions

The interferogram that shows the interference fringe pattern on reflection of the four-core optical fiber used in our experiments is shown in Figure 3.1b. This interferogram is monitored by a CMOS camera with the optical arrangement shown in Figure 3.3, which is observed to shift vertically, horizontally and diagonally when one of the fiber core at the fiber tip is exposed to the heat pulses produced by the Nd:YAG laser. If we assume that the heat pulses are incident onto the fiber core number 1, as shown in Figure 3.1a, a diagonal shift will occur due to cores 1 and 4; vertical and horizontal shifts would occur due to cores 1-2 and 1-3, respectively.

Transient heat pulses with 40 mW optical average power and of 600 ms duration with a repetition rate of the order of 10 s from a Nd:YAG laser are delivered onto the distal end face of the four core fiber, aiming at one of the single cores only (see Figure 3.2), which cause an optical path length difference between the four guiding cores due to the temperature induced change in the index of refraction and physical length of the fiber core in concern. This results in a 0.43±0.015 rad phase shift in the fringe pattern, which causes 1.43±0.05 K temperature rise in the fiber core. For the average pulse power of 40 mW, such a phase shift, and hence 1.43 K temperature change, corresponds to a heat flux Q of approximately 10.9±0.38 kJ/m^{2}s. Temperature and phase sensitivities of our calorimetric gauge are determined to be $\Delta\varphi/\varphi\Delta T = 7.37 \times 10^{-6}\, K^{-1}$ and $\Delta\varphi/l\Delta T = 106.5\ rad/m.K$, respectively. The phase shift determined from the interferogram shown in Fig. 1b is converted to a graph in Figure 3.4 for the clarity of the heat induced phase change of the optical sensor.

The temperature distribution versus position along the fiber core is determined using the Fourier Heat Equation, i.e., Equation 3.11, which is shown in Figure 3.5. Temperature distribution graph helps us to determine the minimum required fiber length for the calorimetric gauge. As seen from the graph in Figure 3.5, heat decays completely at the distance of 2.8 mm, which corresponds to four times the diffusion length (d=0.71 mm). Therefore, the calorimetric gauge's length should be equal or greater than 2.8 mm, i.e., $l \geq 4d$.

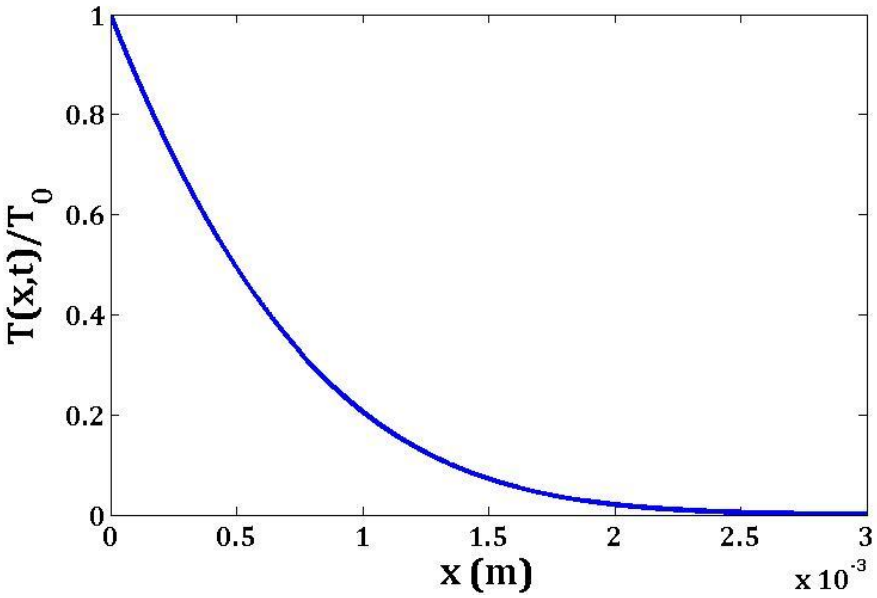

Figure 3.5. Temperature versus the length of the fiber core.

The same experiment is also carried out with the average pulse power of 140 mW. Such a high power is observed to lead a phase shift of 1.30 rad, rising the sensor's temperature up to 4.30 K, and providing a heat accumulation of 33.2 kJ/m^{2}s.

For sensing applications, the increase in the number of equipment employed in optical setups usually causes many adjustment and alignment problems. If an experiment includes multiple fibers, external disturbing factors influence the orientation and the distance of the fiber ends with respect to each other and this situation results in a poor fringe pattern. For the four-core fiber used in this work, a fixed core separation provides a stable fringe pattern, which is used both addressing fiber as well as the sensor, and also simplifies the signal detection scheme.

In the heat measurement studies and temperature sensing applications, the rate of heat loss is the most important factor to ensure whether the system is functioning properly or not. Hence, the sensing fiber length plays a crucial role in constructing a heat detecting sensor, which prevents the system from any heat losses along the fiber core. Besides having a simple working mechanism, cheap and compact sensor, the main feature of this experimental work is to demonstrate that an almost infinite length of the addressing fiber is made available for the heat diffusion in such calorimetric applications. The minimum fiber

length is accepted to be four times of the diffusion length [7], that is, approximately 2.8 mm. For our device, this length is equal to the length of the whole addressing fiber, which is 400 mm, and can be made even longer if needed.

It would be a comprehensive assumption if one models the core of the fiber as a one-dimensional system without studying a 3D heat diffusion modeling since in reality the heat is also diffused in the radial direction and probably a small quantity of heat is also diffused to the adjacent cores. However, each fiber core has a diameter of 10.6 μm and the spot size diameter of the Nd:YAG laser targeted on one of the Al coated fiber cores from the cleaved end-face is less than 1 μm. In addition to this, the distance between the adjacent cores is 40.6 μm. Therefore, it is assumed that the heat diffusion to the adjacent cores may not be significant. Even if some amount of the heat radially diffuses to the adjacent cores, this effect would not alter or change our experimental results since the total phase shift is experimentally measured via a CMOS camera.

The real fiber structure does not only consist of four cores and a single cladding but also consists of four triangular and one square air holes, which can be clearly seen from the SEM image of the four-core optical fiber in Figure 3.6. While one side length of square air hole is 15 μm, each side of the triangular air holes is approximately 17 μm. As the triangular air holes are located between two adjacent fiber cores in horizontal and vertical directions, there is as square air hole at the center of the optical fiber. When laser heat pulses are applied to Al-coated cross-sectional end of the optical fiber, there will be a heat dissipation from the targeted core to the other cores and the air holes. When temperature distribution firstly reaches to the air holes, there will be abrupt and sharp decrease in the temperature. Because these air holes behave like a shield for the cores, temperature distribution does not reach the other cores and it is assumed that the heat distribution in the axial direction occurs inside one targeted fiber core only.

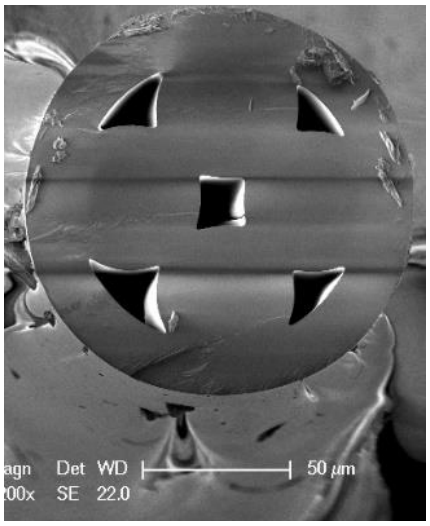

Figure 3.6. SEM image of the four-core optical fiber.

As it is mentioned above that the cleaved end face of the four-core fiber is coated with Al to serve as an end mirror to allow us to operate the experimental work in the reflection scheme. Since the melting point of Al is about 660℃, this system can operate at any temperatures up to 600℃ caused by a Nd:YAG laser irradiation. For higher temperature operations, one may prefer to coat the fiber tip with an oxide material of high refractive index to yield a good Fresnel reflection; for example, with titanium dioxide, tantalum pentoxide or similar oxide coatings with higher melting points.

Transient heat pulses from an Nd:YAG laser, which are perpendicular to surface, are sent onto Al-coated cross sectional end face of the optical fiber, provided that the light is focused onto one of the cores. Since the heat pulses are in the axial direction, Equation 3.10 can be applied to calculate the diffusion and minimum sensor lengths. If these heat pulses were sent to lateral surface or sent with an angle of incidence, Equation 3.10 could not be used to determine the heat diffusion length and the required minimum sensor length. In conclusion, this experimental configuration makes easier to determine these significant lengths.

As explained in the introduction, the four-core optical fiber is insensitive to any external temperature variations since there are no cavities in the system to cause any path imbalance between the four fiber cores. This is certainly a great feature for an optical fiber sensor to be unaffected from the temperature fluctuations in the vicinity of an operating

optical sensor. The only external effect to be taken under control is the vibration or bending effects, which are eliminated by fixing the fiber on a stable stage.

The four-core optical fiber used in our experiments is originally designed to operate at 1.55 μm optical communication wavelength. The cut-off wavelength of each guiding core is much higher than the operating wavelength of 632.8 nm. For this reason, higher order guided modes occur naturally. These higher order modes are filtered out by introducing many bends into the addressing fiber. Bending the fiber also introduces a constant phase shift between the cores but that does not affect the measurement. Instead of using a fiber with larger core size, a fiber designed with appropriate core size being compatible with the operating wavelength in concern would be more suitable to eliminate extra higher order modes and to obtain an ideal interference pattern.

4. INVESTIGATION OF A NOVEL TEMPERATURE-SENSING MECHANISM BASED ON STRAIN-INDUCED OPTICAL PATH-LENGTH DIFFERENCE IN A MULTICORE OPTICAL FIBER

4.1. Introduction

Measurement of specific conventional physical parameters such as temperature, strain, pressure, bending, vibration, humidity, or magnetic field in an ingenious scientific way has always been the main motivation behind the research in the field of sensing technology. Interferometric fiber optic sensors have taken a particularly significant role in this area by introducing cost-effective optical devices with high sensitivity, small size, light weight, and sustainability against high temperatures [3, 5, 107, 108, 11, 12].

Several former studies have made use of multicore and photonic crystal fibers in the measurement of temperature and strain sensing. For example, Antonio-Lopez *et al.* [109] sandwiched a segment of 2–3 cm of seven-core fiber between two single mode fibers by splicing them to each other, thus constructing a Fabry–Perot type interferometer to measure temperatures of up to 1000 ˚C with an accuracy of 29 pm/˚C. In another study, a piece of hollow-core fiber was connected at both ends to standard single-mode fiber to construct a modal interferometer for both temperature and strain measurements. The resolutions were reported to be 1.4 με and 0.2 ˚C for strain and temperature, respectively [110]. Four-core optical fibers were used previously in two axis bend measurement [107] and three-dimensional optical profilometry [105]. Recently, Guvenc *et al.* successfully used the same type of fiber to demonstrate that a four-core optical fiber can be used as a calorimetric gauge in heat transfer measurements. The sensitivity of the device was given to be 7.37×10^{-6} K^{-1}.

In this paper, an interferometric fiber optic temperature-sensing mechanism based on shear strain in a four-core optical fiber is demonstrated. A four-core optical fiber allows guiding four mutually coherent light beams within a single cladding of 125 μm in diameter and is capable of producing an interference pattern of square-like strips at the far field [107]. One may assume that each fiber core corresponds to an arm of a Michelson or Mach–Zhender interferometer to form an interferogram. A few centimeters of the four-core fiber are wound around a solid stainless steel cylinder to obtain a tight circular loop, which is

exposed to temperature rise. The temperature-induced radial expansion of the stainless-steel cylinder introduces a shear strain in the fiber loop, which causes an optical path-length difference between the four guiding beams in the inner and outer core pairs. This results in a phase shift in the interference pattern of the four-core fiber, which is monitored by a CMOS camera, giving a monotonic relationship between the temperature and phase of the guiding laser light. The method also allows determining the value of the shear strain with good precision.

A straight piece of a four-core optical fiber is totally immune to any temperature changes under normal circumstances since there are no cavities to cause any optical imbalance in the addressing fiber, provided that the fiber is much longer than the coherence length of the laser source. However, since the four-core optical fiber is quite sensitive to any bending due to the strain effects [107], such a mechanism is utilized to build a strain-based temperature-sensing mechanism, which is considered to be the unique feature of this work. In addition to the temperature measurements using the thermal expansion of a known cylindrical material, one may measure the thermal expansion of unknown materials with the proposed experimental arrangement since the working mechanism allows to relate the phase shift to the temperature change, strain, and thermal expansion of the material in concern.

The layout of the paper includes the strain-induced phase shift related to the optical path-length difference, which is followed by the experimental results, discussions, and a conclusion.

4.2. Principle of the Method

A four-core optical fiber is used to obtain the interference of four coherent light beams. A schematic illustration of a four-core optical fiber and its corresponding interference fringe pattern are shown in Figures 4.1a and b. There are six couplings of the fiber cores, which introduce four different interferograms. A vertical interferogram is formed by pairings of the horizontal cores, a horizontal interferogram is generated by couplings of the vertical cores, and the pairings of the diagonal cores produce two opposite diagonal interferograms. The superposition of these enables an interferometric fringe pattern, which is shown in Figure 4.1b.

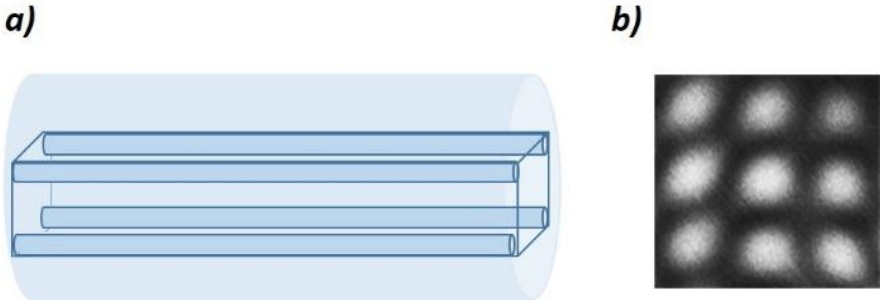

Figure 4.1. (a) Schematic representation of a four-core optical fiber and (b) its real interferometric fringe pattern.

The intensity distribution of the fringe pattern from a four-core optical fiber is given by [105]

$$I(x,y) = 2I_O\left[\begin{array}{l} 2 + 2\ \cos\left(2\pi\frac{\delta}{\lambda f}(x\cos\theta - z(x,y)\sin\theta)\right) \\ +2\cos\left(2\pi\frac{\delta}{\lambda f}(y\cos\theta - z(x,y)\sin\theta)\right) \\ +\cos\left(2\pi\frac{\delta}{\lambda f}((x+y)\cos\theta - z(x,y)\sin\theta)\right) \\ +\cos\left(2\pi\frac{\delta}{\lambda f}((x-y)\cos\theta - z(x,y)\sin\theta)\right) \end{array}\right] \tag{4.1}$$

where λ is the wavelength of the light beam, I_0 is the intensity, f is the focal length of the lens, θ is the illumination angle, δ is the separation distance between horizontal and vertical cores, x, y and z are the coordinates of the interferogram. However, in this work, the fringe pattern on the CMOS camera and the cores are illuminated by a laser beam at zero-degree angle. Therefore, when z=0 and θ=0, the intensity equation becomes the following:

$$I(x,y) = 2I_O\left[\begin{array}{l} 2 + 2\cos\left(2\pi\frac{\delta}{\lambda f}(x)\right) \\ +2\cos\left(2\pi\frac{\delta}{\lambda f}(y)\right) \\ +\cos\left(2\pi\frac{\delta}{\lambda f}((x+y))\right) \\ \cos\left(2\pi\frac{\delta}{\lambda f}((x-y))\right) \end{array}\right] \tag{4.2}$$

As the temperature is varied in the vicinity of the four-core fiber shown in Figure 4.1a, no path difference is expected to occur between the guiding four cores to cause any fringe shifts since all the cores experience the same thermal expansion and the same thermal optical effects. However, if one makes the same fiber as a tight circular loop around a cylindrical object and lets the cylinder radially expand, as seen in Figure 4.2, then Δl path-length difference occurs between the inner and outer core-pairs since the outer core-pairs would be elongated more due to the presence of a shear strain. Exposing the cylindrical object to a temperature rise for a radial expansion is the principal idea behind our novel strain-based fiber optic temperature sensing method.

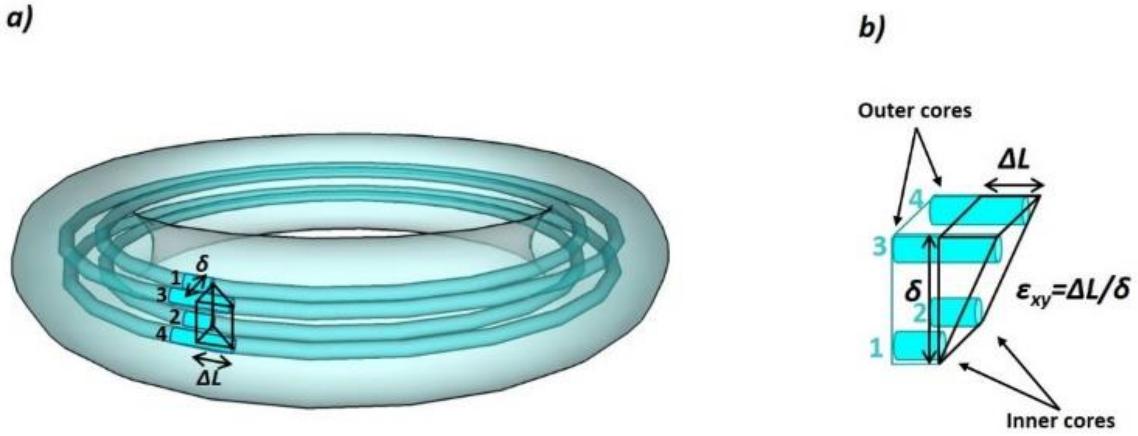

Figure 4.2. (a) Schematic representation of the strain induced path-length difference between inner and outer core lengths and (b) enlarged picture of the path length difference.

One can express the phase of the guiding light in the fiber cores as:

$$\phi = \frac{2\pi n l}{\lambda} \tag{4.3}$$

where n is the refractive index and l is the sensitive part of the fiber length. The strain ($\mathcal{E}$) dependent phase difference corresponding to the changes in the refractive index and the length is given by

$$\frac{\partial \phi}{\partial \varepsilon} = \frac{2\pi}{\lambda}\left(n\frac{\partial l}{\partial \varepsilon} + l\frac{\partial n}{\partial \varepsilon}\right) \tag{4.4}$$

The strain-induced phase difference between inner and outer two cores is given by [111]

$$\Delta\phi = \frac{2\pi}{\lambda}\Delta l(n - Kn^3) \tag{4.5}$$

where λ is the wavelength of the guiding beam and Δl is the length difference of one inner and one outer core after strain-induced stretching, for example, 1-3, 2-4, 1-4, or 2-3. For fused silica fiber, n=1.46 and K=0.103 [112] are taken. Since the phase change is experimentally measured by a CMOS camera, Δl is easily calculated via Equation 4.5, which allows us to determine shear strains $\varepsilon_{xx} = \frac{\Delta l}{l}$ and $\varepsilon_{xy} = \frac{\Delta l}{\delta}$, where l is the length of the fiber loop and δ is the separation between the two cores, as shown in Figure 4.2.

4.3. Experimental Setup

A schematic representation of the experimental setup is given in Figure 4.3. Linearly polarized light from a He-Ne laser with the emission wavelength of 632.8 nm is coupled into a four-core optical fiber of about 45 cm in length using a 21× microscope objective lens to produce the interference fringe pattern shown in Figure 4.1b. A polarizer was located at the end of the fiber, before the screen, to obtain a fully polarized light in order to improve the fringe quality. In this experiment, a Glen type polarizer was used to work with only p-polarized light. Since the four cores are embedded in a single cladding with a bare fiber diameter of 125 μm, four cores act as mutually coherent sources to produce an interference pattern. Each core has a diameter of 10.6 μm and the distance between adjacent cores is 40.6 μm. The details of the four-core fiber can be found elsewhere [113].

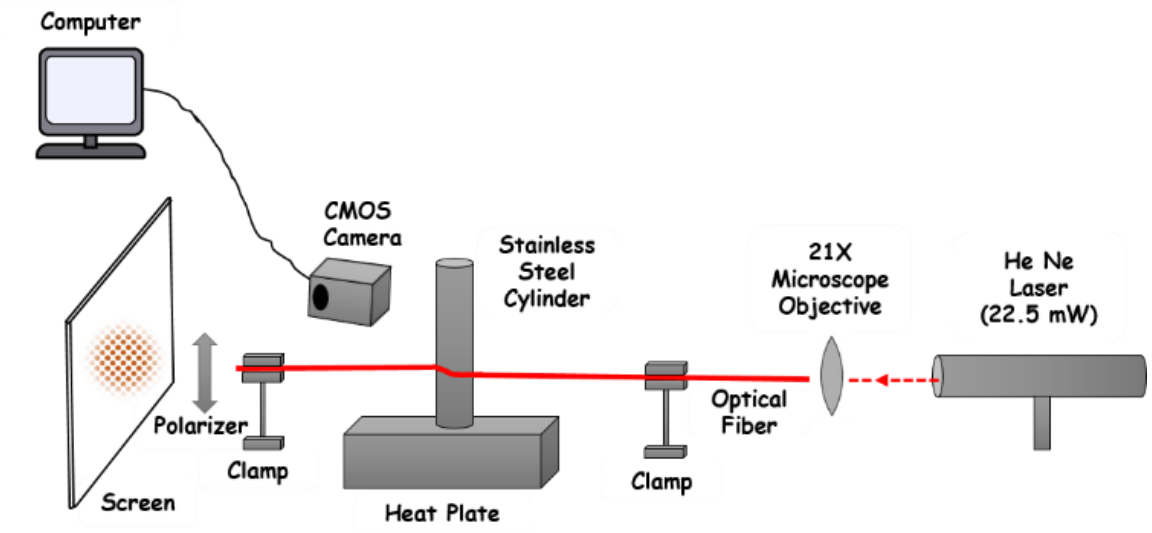

Figure 4.3. Schematic representation of the experimental setup.

After a desired fringe pattern is obtained on the screen and monitored by a CMOS camera, a fiber length of about 12 cm is wound around a stainless-steel cylindrical rod with a diameter of 3.77 cm. The fiber ends are clamped to obtain a very tight circular loop for a shear strain in the four-core fiber to be effective as the metal rod thermally expands. The steel rod is placed on a heat plate, which is used to control the temperature and to provide thermal expansion of the rod. The temperature of the fiber loop and the heat plate are assumed to be the same since the fiber loop was placed very close to the touching end of the rod with the heat plate.

4.4. Results and Discussion

The heat plate is turned on to run from room temperature up to 100 ˚C. It is observed that the phase does not show any changes until the heater's temperature reaches about 40 ˚C, which means that the thermal expansion of the steel rod is not sufficiently large enough to initiate a desired strain for a phase shift between the fiber cores since the circular fiber loop around the metal rod is not amply tight. Therefore, the temperature interval from 50 ˚C to 92 ˚C is studied in our experiments to observe a clear phase change. The diameter of the stainless-steel rod is measured by a Vernier calipers at 50 ˚C and at 92 ˚C. The amount of the radial expansion of the steel rod causing a shear strain to the fiber ring is measured to be about 0.02 mm. Due to the geometry of the fiber ring, the outer core pairs are more stretched than the inner ones, which leads to an optical path-length difference between the waveguiding cores. This results in a phase variation, which is monitored and stored by a CMOS camera. A MATLAB code is used to analyze the stored interferogram frames during the phase change. When the phase shift occurs, the intensity distribution of the selected part of the fringe pattern varies. Since the observed phase shift is two-dimensional, our vertical and horizontal software reference lines, which are placed on the pictures in the MATLAB domain, allow us to analyze the intensity distributions on these directions. After horizontal and vertical phase shifts are calculated, the total phase change is determined using the Pythagorean theorem.

Although the phase shift itself is periodic in nature; such a shift is observed as a continuous flow away on the screen of the fast CMOS camera and then the data are stored. Therefore, the dynamic range of the sensor is not limited by the period. Figure 4.4 shows the

interference patterns for two different temperatures (50 ˚C and 92 ˚C). Since the pattern repeats itself after every 2π phase shift, the shift looks very slight due to a total phase shift of about 20.40 rad.

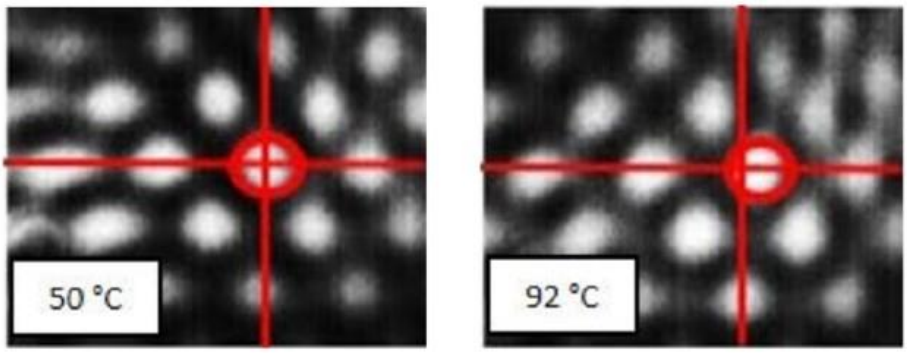

Figure 4.4. Interference patterns for two different temperatures (50 ˚C and 92 ˚C).

Figure 4.5 shows temperature versus phase shifts due to the path differences between various fiber core pairs, i.e., cores 1-3 plus 2-4 and cores 1-4 plus 2-3, together with the total phase shift versus temperature. As seen from the fit in the graph, a monotonic linear relationship between phase and temperature is obtained. If one assumes that e_1 and e_2 are the phase shift principal axes (see inset of Figure 4.5), the temperature-induced phase shift in the e_1 direction would be due to cores 1-3 plus 2-4 and the phase shift in the e_2 direction is due to cores 1-4 plus 2-3. In Figure 4.5, for the temperature range from 50 ˚C to 92 ˚C, a net phase shift of 18.8 rad is measured in the e_1 direction and 8.01 rad is measured in the e_2 direction, leading a total phase shift of 20.4 ± 0.29 rad. The phase shift in the e_2 direction is much less than that of in the e_1 direction, which tells us that the phase shift in the e_2 direction is due to the diagonal core pairs. In other words, the elongation in cores 1 and 2 (or 3 and 4) are the same since the inner/outer core pairs have the same bend radii, and they are expected to be stretched at the same rate. Measured phase shifts in the e_1 and e_2 directions together with the corresponding shear strains are summarized in the Table. The path-length difference Δl is determined from Equation 4.5 to be 1.66 μm and 0.71 μm for core pairs 1-3 plus 2-4 and 1-4 plus 2-3, respectively.

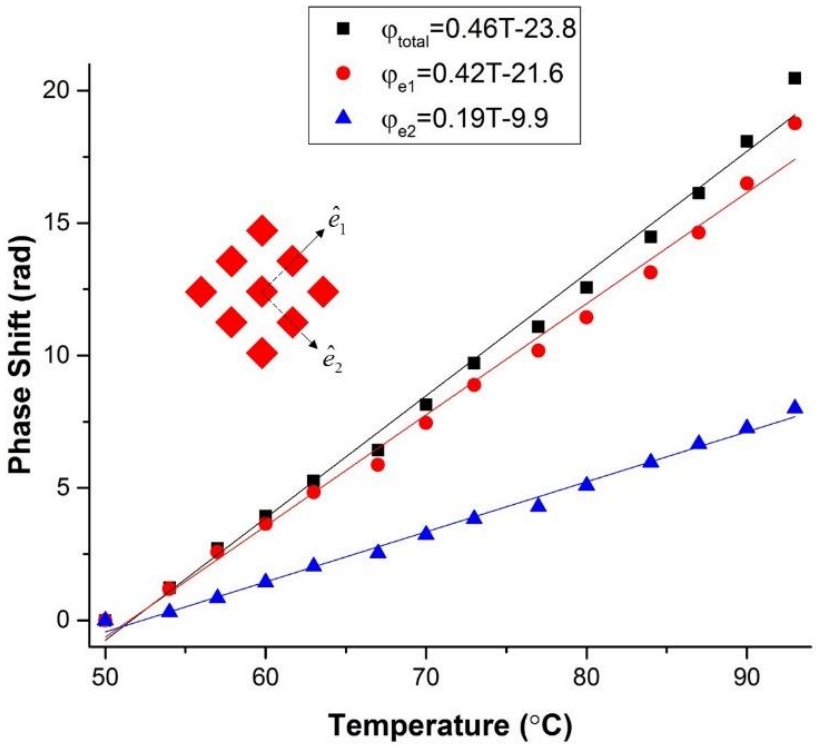

Figure 4.5. Phase change versus temperature in e_1 and e_2 directions together with the total phase shift for a winded four-core fiber loop around a stainless-steel solid cylinder.

Table 4.1. Phase shift and strain values in the e_1 and e_2 directions.

	e_1 direction	e_2 direction
Phase shift (rad)	18.76	8.01
Δl (μm)	1.66	0.71
ε_{xx} (microstrain)	13.50	5.77
ε_{xx} (microstrain)	40.89	12.36

The temperature-induced phase and strain sensitivities of the four-core fiber are determined to be $\Delta\varphi/l\Delta T$ = 3.74 rad/m˚C and 0.18 μm/˚C, respectively. The temperature resolution of the device is determined to be 0.49 rad/˚C, which is limited by the resolution of the CMOS camera (Optronis CR600x2). The camera could measure 15 mrad phase shifts, corresponding to 50 m˚C changes.

In this experiment, power fluctuations have no effects on the determination of the phase shifting of the fringes and hence the resultant temperature-induced strain data. No

power variations are detected in the system throughout the experiments. Even if there is a slight power variation in the optical system, this could only affect the fringe visibility slightly but not the phase measurement.

The transduction mechanism proposed here in this work has the potential to be a candidate for the construction of new fiber optic temperature sensors. Although the experiments are performed in the temperature interval between 50 ˚C and 92 ˚C, since the optical fiber's melting point is around 1100 ˚C [114], it is envisaged that the system can easily operate at temperatures beyond 92 ˚C unless the strain due to the thermal expansion of the rod causes any damage to the optical fiber material and its polymer jacket. For higher temperature operations, the strain experienced by the optical fiber may also be calculated with the expansion properties of the metal rod before the experiment. The tightness of the circular fiber loop around the stainless-steel cylinder should be adjusted in such a way that the tensile strength of the fiber is able to withstand much higher temperatures so that the fiber does not break down.

As stated above, a straight piece of a four-core optical fiber is totally immune to external temperature variations since there are no cavities or internal/external mirrors associated to the fiber itself to give rise to any optical imbalance between the fiber cores. Our main contribution here in this work is to scheme out a new temperature-sensing transduction mechanism, which is based on strain-caused optical imbalance in the guiding cores of a four-core fused silica optical fiber.

The main advantage of this method is the flexibility to design a more sensitive device for a desired temperature range. Apart from the stainless-steel rod, various types of materials can be employed in the experiment to induce different amounts of strain in the optical fiber. More sensitive sensors can be devised using materials with higher thermal expansion coefficient properties. In other words, one may consider a cylindrical material with high thermal expansion coefficient if the device is desired to be very sensitive. Similarly, a low thermal expansion coefficient material may be used to make use of the four-core fiber to achieve a much higher dynamical range, say up to the melting point of the polymer jacket, which covers the fused silica fiber, i.e. around 300 ˚C. The dynamic range would have been directly proportional to the limit of the tensile strength and the melting point of the fused

silica material, i.e. 1100 ˚C, if it were possible to bend a bare fiber with the radii we used in our experiments. Unfortunately, one cannot form a circular loop with a bare optical fiber of more than 20-30 cm in diameter due to the brittle nature of fused silica glass. Another benefit of our scheme is that instead of using a known material as a thermally expanding rod, the thermal expansion of unknown materials can also be measured with the phase shift by the same experimental arrangement if one calibrates the system with a known cylindrical material first.

The experiment is repeated with several different rod diameters and the measurements are carried out several times for each sample. The results are observed to be repeatable. It is observed that larger diameters give higher sensitivity since the exposed fiber length is larger. The whole purpose of this work is to demonstrate the sensing mechanism, which is based on the strain-induced optical path-length difference between the fiber core pairs. If one aims to make use of this mechanism to build a temperature sensor, it will simply require calibrating the sensor with the rod diameter in concern. For a more compact sensor, a thin rod with several fiber loops would significantly enhance the sensitivity of the sensor.

To obtain reliable experimental results, the system must be well isolated from the external disturbing factors and the fringe pattern must be kept stable throughout the measurements. Since the optical fiber is sensitive to mechanical fluctuations and bending effects, the external parameters are eliminated by stretching and fixing both fiber ends using clamps as shown in Figure 4.3. The optical fiber must be kept tense at every point in the experimental setup to achieve a pure strain in the fiber cores. Although the four-core optical fiber used in the experiment provides a good interferometric fringe pattern, a small core spacing of 40.6 μm and large core diameters of 10.6 μm result in higher-order guided modes in the interferogram, causing an insignificant fringe stability problem since the four-core fiber was originally designed at the optical communication wavelengths. To overcome this problem, a four-core optical fiber with smaller core diameters and smaller core spacing should be used to obtain more stable and much clearer interference fringes.

Finally, one needs to make sure whether the curved fiber that is wound around the cylindrical rod has a twist within the curved region. In that case, a specific core would be compressed at some places and stretched at other places. This results in some sudden phase

jumps in the phase of the guided light and hence sudden shifts would occur in the far-field interference pattern as the twist rescues itself. To overcome this problem, white light is coupled into the fiber cores to clearly observe each core under an optical microscope. The curved region is scanned under the microscope to avoid any fiber twist within the curved region around the cylindrical rod.

5. INTERFEROMETRIC TEMPERATURE AND HEAT SENSOR WITH A FOUR-CORE OPTICAL FIBER AND ITS FINITE ELEMENT SIMULATIONS

5.1. Introduction

Fiber optic sensors (FOSs) based on interferometric methods have a key role in detecting many of the external physical parameters such as temperature, heat, pressure, refractive index, strain, stress change etc. Simplicity, design, low cost, flexibility, durability, and reliability in signal detection are listed as some of the essential and significant features of fiber optic interferometry [6-8, 10-14, 46, 104, 106].

Depending on the operating principles and fabrication processes, many kinds of interferometers have been constructed by researchers to detect physical, chemical, and biological parameters. At the beginning of FOS studies, single core, single mode, and multiple numbers of optical fibers were preferred in the experiments. One of the most well-known and fundamental studies of fiber optic interferometry in sensing applications was successfully presented by G. B. Hocker in 1979 [6]. In this experiment, two single core and single mode optical fibers were used to form a Mach-Zehnder interferometer configuration. An interference pattern in transmission scheme was generated using two single mode and single core fibers. By applying temperature to one of the optical fibers, a phase shift in the interference pattern occurred and then the amount of the temperature change was determined.

In 1992, the configuration of the Fabry-Perot interferometer was used to measure heat transfer rates by K. S. Chana *et al.* [7]. One year later, a miniature interferometric fiber optic temperature sensor was constructed by M. N. Inci *et. al.* using single mode and single core optical fibers. The cross-sectional end face of the fiber was coated with titanium dioxide (TiO_2) and this coated surface served as an internal mirror in the optical fiber, which led this system to be presented as a Fabry-Perot interferometer. A short single core and single mode fiber was spliced to TiO_2 coated end of the fiber. By applying heat to second fiber, a shift in the interference pattern occurred. The temperature change and the amount of the heat accumulated inside the fiber core were calculated [8].

Within the last two decades, experiments have become less complicated and sensors have become more compact using multi-core fiber structures. A multicore fiber was employed for the first time by M.J. Gander *et al.* for bending measurements. In 2007, Libo Yuan *et al*. performed an experiment series which employs four-core optical fiber to detect some physical parameters such as bending, rotation, and temperature [11]. In the initial stage of the experiment, the fiber was bent at certain angles and the shifts in the interference pattern were recorded by a CCD camera. The first results clearly demonstrated that the fiber was able to detect the bending. As a second study, the optical fiber was rotated with small angles and the rotation pattern of the interference was detected by the camera. It was shown that the fiber was also able to detect the rotation. In the final step of this project, fiber structure was placed between two plates of Peltier device. While one of the plates was hot, the other one was cold to generate a temperature distribution between the fiber cores. In this part, there was no response to temperature distribution since all cores were experienced with that temperature distribution, simultaneously. In 2012, a temperature sensor based on refractive index change was constructed by R. Romaniuk *et al.*, using a two-core optical fiber [12]. In this work, both theoretical and experimental studies of a temperature sensor were reported. The main working mechanism of this study was based upon the changes in both physical length and refractive index of the region between two cores.

Recently, studies on temperature and heat sensing applications using different types of optical fibers with smart and compact configurations have been carried out. In 2016, L.V. Nguyen *et al.* fabricated an interferometric high temperature sensor which can operate up to 1100˚C [13]. This special fiber structure consists of three air holes and one core surrounded by these 3 empty cores and this fiber system still holds the total internal reflection phenomenon observed in regular fiber structures. In this experiment, using this special fiber structure, L.V. Nguyen *et al.* observed a shift in the interference pattern because of increase in temperature. Another recent study reported by Guigen Liu *et al.* successfully showed that a fiber optic temperature sensor can operate at temperatures higher than 1000˚C [14]. In their study, the miniature silicon crystal Fabry – Perot interferometry was attached to a single core fiber using a fusion splicer. The silicon part was heated with a laser and the shifts in the interference pattern were examined.

As mentioned above, the detection of various external physical parameters, such as temperature, with the help of single core and multicore fibers, has been extensively studied by many scientists [6-8, 11-14]. The aim of this project is to fabricate a multicore fiber optic sensor which enables highly precise measurements of temperature and heat transfer rates.

5.2. Theoretical Part

When optical fibers are exposed to temperature, the refractive indices (thermo-optical effect), diameters, and axial length (thermal expansion) of the cores change, accordingly. The working mechanism of interferometric heat and temperature sensors is usually based on making use of these variations. The interference pattern shifts as a result of the applied heat or temperature and this shift is observed with the help of a camera, photodetector, or an oscilloscope. Depending on the shift, the amount of accumulated heat and temperature change inside the fiber core is determined. The phase is given by the following formula [6-8]:

$$\varphi = \frac{2n\pi l}{\lambda} \tag{5.1}$$

In this formula, n represents refractive index of fiber core, l is the length of the sensitive part of the fiber, and λ is the wavelength of the light source. When temperature or heat is applied to the fiber, the phase change as a result of variation in the refractive index and the length of the fiber core is given by the following formula:

$$\Delta\varphi = \frac{2\pi l}{\lambda}\left(\frac{n}{l}\frac{dl}{dT} + \frac{dn}{dT}\right)\Delta T \tag{5.2}$$

In this equation, $\Delta\varphi$ and ΔT represents the average phase change and the average temperature change, respectively. Constant parameters of the fiber used in the experiment are given as follows: $n = 1.456$, λ is the wavelength of the light source, $dl / ldT = 5 \times 10^{-7}\ K^{-1}$ and $dn / dT = 10 \times 10^{-6}\ K^{-1}$[6-8]. As it can be seen from Equation 5.2, the phase change is directly proportional to temperature variations, and if one of the parameters is known, the other one can be easily calculated.

If a laser heat pulse is applied to the optical fiber from the Aluminum (Al) coated surface, a certain amount of heat accumulates inside the fiber core(s). The amount of the heat accumulated inside the fiber core is given by the following formula [8]:

$$Q = \rho c l \frac{dT}{dt} = \frac{\rho c}{k} \frac{d\varphi}{dt}. \tag{5.3}$$

Here, ρ represents the density of the core, c is the specific heat capacity, and k is the thermal sensitivity. Thermal sensitivity is given as

$$k = \frac{4\pi}{\lambda}\left(\frac{n}{l}\frac{dl}{dT} + \frac{dn}{dT}\right). \tag{5.4}$$

Another important parameter in temperature sensor applications is heat diffusion length. Heat diffusion length is given in the following formula [7]:

$$d = \sqrt{\gamma t}\,. \tag{5.5}$$

In this equation, the value of thermal diffusivity which is shown by γ, is equal to 8.2×10^{-7} m^2s, and t is the pulse duration. This formula can be used for heat and temperature sensing applications to determine effective diffusion length and minimum sensor length if the heat is applied along the axial direction. Minimum length of the fiber optic sensor (l) should be at least four times of the diffusion length to prevent the heat loss from the system [7].

$$l \geq 4d. \tag{5.6}$$

The relation between heat flow and temperature (T) is given by Fourier heat equation formula which is a function of position (r) and time (t). In addition to this, information about how far the heat diffuses is obtained by the following equation [106]:

$$K\nabla^2 T(r,t) = c\rho(\partial T/\partial t) - Q(r,t) \tag{5.7}$$

where K is the thermal conductivity coefficient and Q is the heat transfer rate. The one-dimensional solution of this equation provides us with the following equation [104]:

$$T(x,t) = \frac{Q}{\rho c K}\left[\frac{2\sqrt{t}}{\sqrt{\pi}} e^{-\frac{x^2}{4\alpha t}} - \frac{x}{\sqrt{\alpha}} erfc\sqrt{\frac{x^2}{4\alpha t}}\right]. \quad (5.8)$$

In our experiments because laser heat pulse is applied from lateral Al coated surface, Equation 5.6 is not applicable to determine the diffusion length and the minimum sensor length. For this study, Finite Element Modelling (FEM) simulations are carried out to determine the heat diffusion length and minimum sensor length.

5.3. Experimental Part

A multicore optical fiber is used in our experiments. This fiber consists of four cores with a refractive index of 1.456, four triangular air holes, and a square air hole which is located at the center of the fiber. Each core diameter is approximately 10.6 µm and the distance between adjacent core pairs is about 40.6 µm. While one side length of the square air hole is 15 µm, each side of triangular air holes is approximately 17 µm (Figure 5.1). Cores and air holes are surrounded by a cladding which is a material with lower refractive index than the cores and with a diameter of 125 µm. In addition to this, cores, air holes, and cladding region are covered by a silicon jacket with a diameter of 250 µm to protect the fiber structure from the environmental factors.

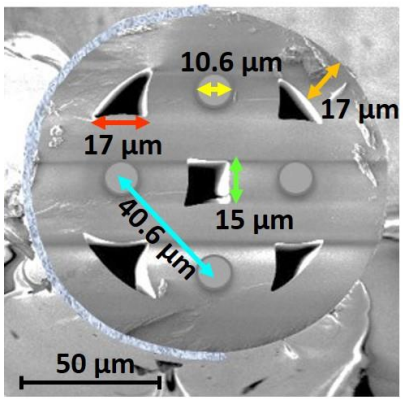

Figure 5.1. The dimensions of air holes in a four-core fiber structure are decided by using ImageJ program.

At the initial step of the experiment, silicon jacket with a length of 4-5 cm and is removed from both ends and center part of the fiber. Because fiber structure is transparent

to the heat pulsed produced at 532 nm by an Nd:YAG laser source, it is fixed on a flat plate and the half of this lateral surface is coated with Al with a thickness of 100 nm by thermal evaporation method. When a laser heat pulse is applied to this Al coated fiber, it is absorbed by this surface, which starts to heat up, and then this heat dissipates through the radial and axial directions in the fiber core(s). Schematic representation of fiber preparation steps for heat and unsteady temperature measurements is shown in Figure 5.2.

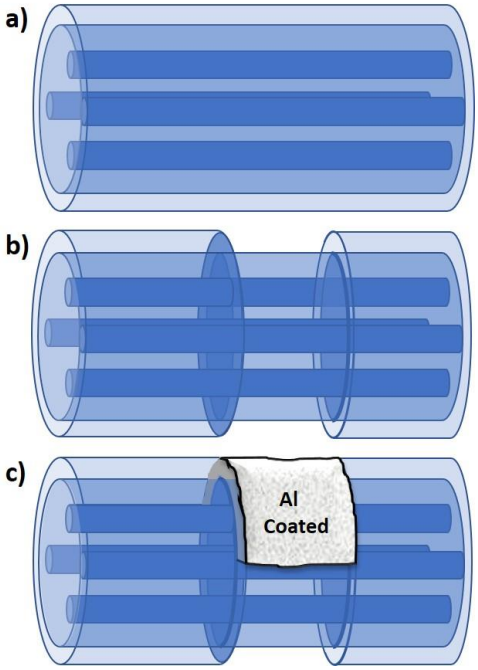

Figure 5.2. (a) A four-core optical fiber with cladding and silicon jacket part. (b) Silicon jacket with a length of 4-5 cm is removed from the center part of the fiber. (c) Half of the lateral surface is coated with Al.

In the temperature and heat transfer rate measurement experimental studies, two different lasers are employed. While one of them is used to generate an interference pattern in transmission spectrum, the other one is utilized for heating. During the experiment, firstly, He-Ne laser with a wavelength of 632.8 nm is directed into the fiber cores. Incident light is coupled into the cores by using a 10× focusing lens and an interference pattern is formed in transmission scheme. This interference pattern is directly sent onto a CMOS camera to record the frames during the experiments. One of the most important part of this experiment is to obtain a stable and reliable interference pattern which is not affected from the external fluctuations. Figure 5.3 shows the interference pattern combinations depending on the positions of cores and core couplings. Vertical fringe pattern is due to core 1- core 2 and

core 3 - core 4 couplings; and horizontal fringes are formed by core 1- core 3 and core 2- core 4 couplings. In addition to these fringes, couplings of core 1- core 4 and core 2 - core 3 produce diagonal fringes [14]. The final interference pattern is in the form of a combination of all these patterns (Figure 5.3).

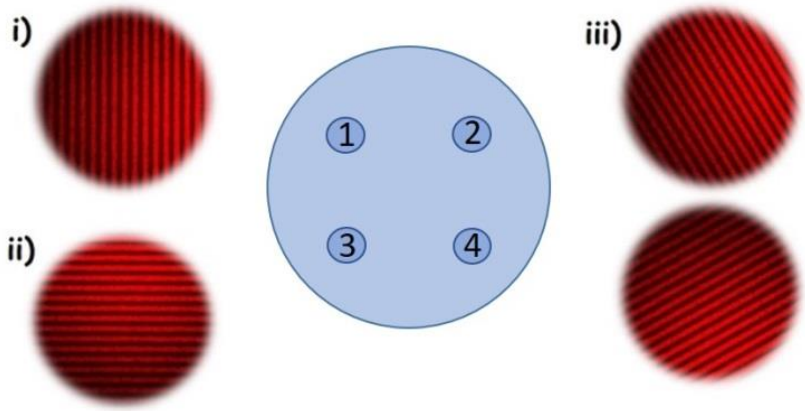

Figure 5.3. Interference pattern combinations depending on the core couplings. 1-2 and 3-4 couplings result in an interference pattern in i. 1-3 and 2-4 couplings generate an interference pattern in ii. 1-4 and 2-3 couplings causes interference pattern in iii. In this study, the interference pattern is a combination of all these fringes.

After a stable interference pattern is obtained, Al coated lateral surface of fiber is heated by a continuous Nd:YAG laser with a wavelength of 532 nm. In front of the laser, a chopper is placed to generate laser heat pulses. Therefore, enough time is allowed for the fiber to warm up and to cool down. The incoming laser light is focused on the fiber core using a microscope lens with a numerical aperture of 0.70 (Nikon ELWD 100 X). Figure 5.4 shows the detailed schematic representation of the experimental setup.

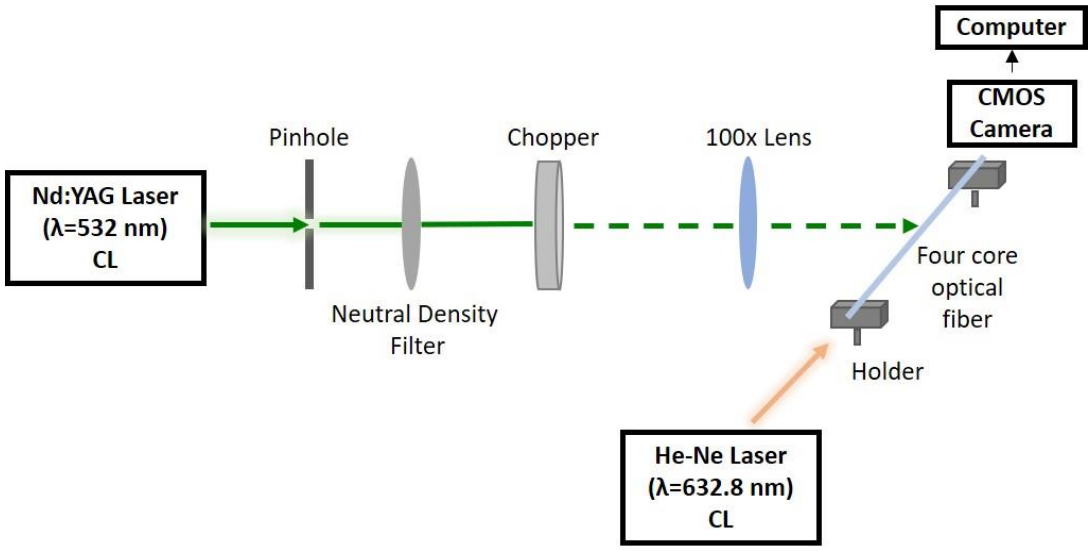

Figure 5.4. Schematic representation of the experimental setup.

In addition to the experiments, which use laser heat pulses to cause temperature and heat changes in a fiber core, another experiment series is carried out. Experimental setup is schematically shown from Figure 5.5. In these experiments, hot air vortices are utilized to observe the response of multi core fiber sensor to unsteady temperature changes. Hot air vortices are sent onto the lateral surface of fiber structure. In this experimental setup, by using a power supply, a copper wire is heated. Air flow from an air blower is sent onto the hot copper wire. This causes the generation of hot air vortices. Hot air vortices cause unsteady temperature changes in targeted fiber core.

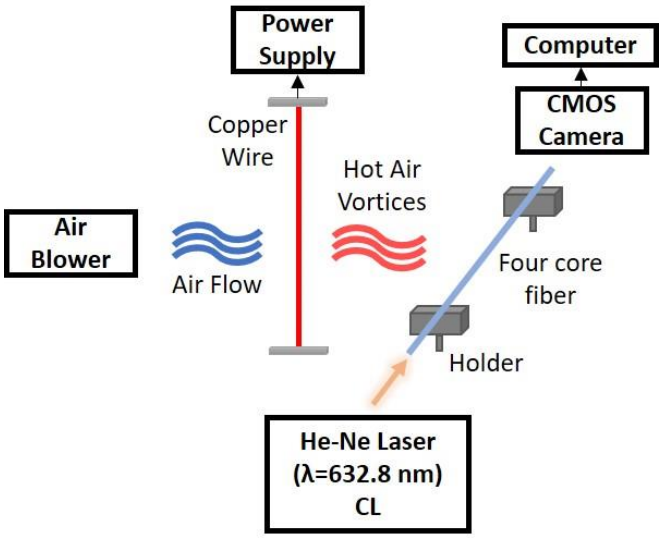

Figure 5.5. Schematic representation of unsteady temperature measurement experiment.

5.4. Experimental Data Analysis

The main working principle of this system is based on the change in the optical path length, which is caused by the variation in the refractive index and the physical length of the fiber cores. This optical path difference between cores introduces a shift in the interference pattern. One of the most important factors is the number of the heated cores by the laser pulses. In the experiments, it is aimed that heat laser pulses and hot air vortices are sent onto only one targeted fiber core. By observing the interference pattern, it is very easy to estimate core positions. As stated before, the resulting interference pattern in Figure 5.6 is a combination of horizontal, vertical, and diagonal interferograms. While the core positions are not rotated, the resulting fringe pattern will be in the Figure 5.6a. If the fiber structure is rotated about 45° from its original place (0°), interference pattern will be in the Figure 5.6b. The schematic representations of concerned core positions with their corresponding interference patterns are shown in Figure 5.6.

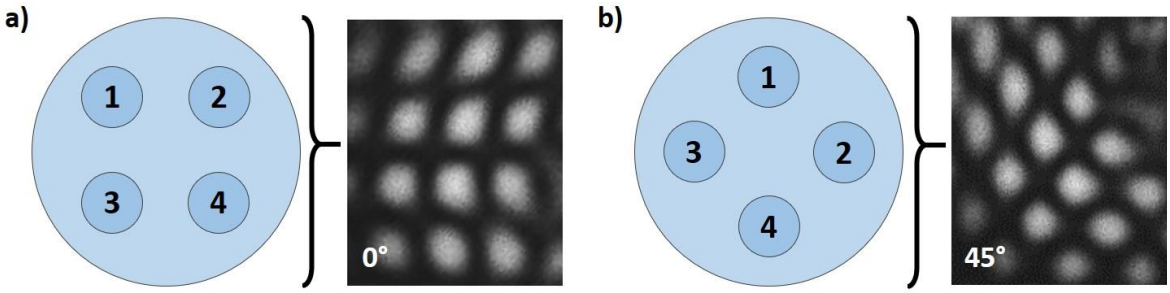

Figure 5.6. (a) Core positions with no rotation and (b) core position with a rotation of 45° and their corresponding fringe patterns.

Figure 5.7a shows the interference pattern and intensity distribution in both directions for a pulse duration of 0.12 s. To obtain the intensity distribution for both direction, three bright spots in x and y directions are chosen (Figure 5.7a).

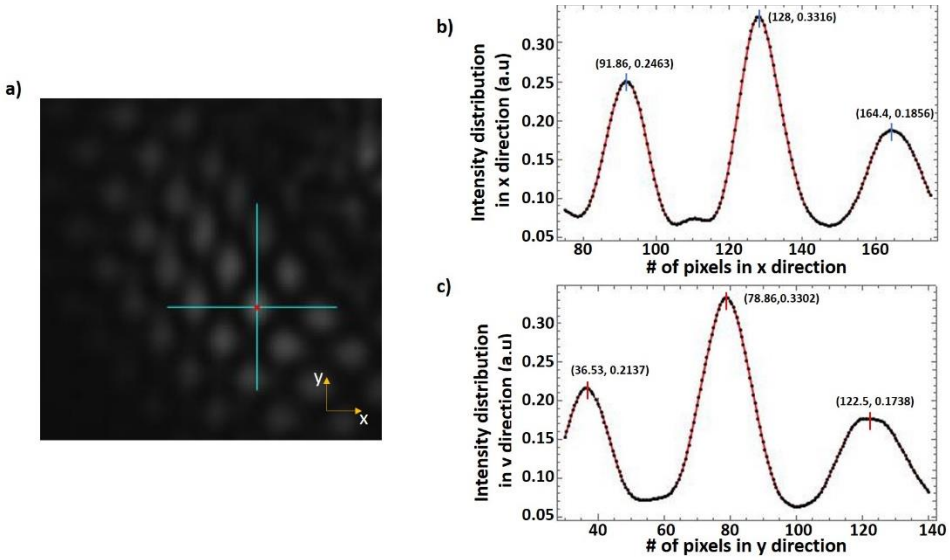

Figure 5.7. (a) The resulting interference pattern of a four-core optical fiber, (b) and (c) intensity distributions in x and y directions for 0.12 s.

The intensity distributions which belong to three bright spots in both directions are obtained by using a Mathematica code. Figure 5.7b and c show the intensity distribution for both directions and x and y values for local maxima of each peak. The pixel difference values of each two successive peaks (1-2 and 2-3) provide to obtain the number of pixels corresponding to 2π. The average pixel value for x and y direction are 36.3 and 43.4, respectively.

Consecutive laser heat pulses are applied to Al coated surface of optical fiber. Figure 5.8a and b show the shifts in x and y directions. For region 1 and region 2 in Figure 5.8a and b, shifts in x and y directions are the results of multi laser heat pulses. For region 3 in Figure 5.8a an b, only one laser heat pulse is applied.

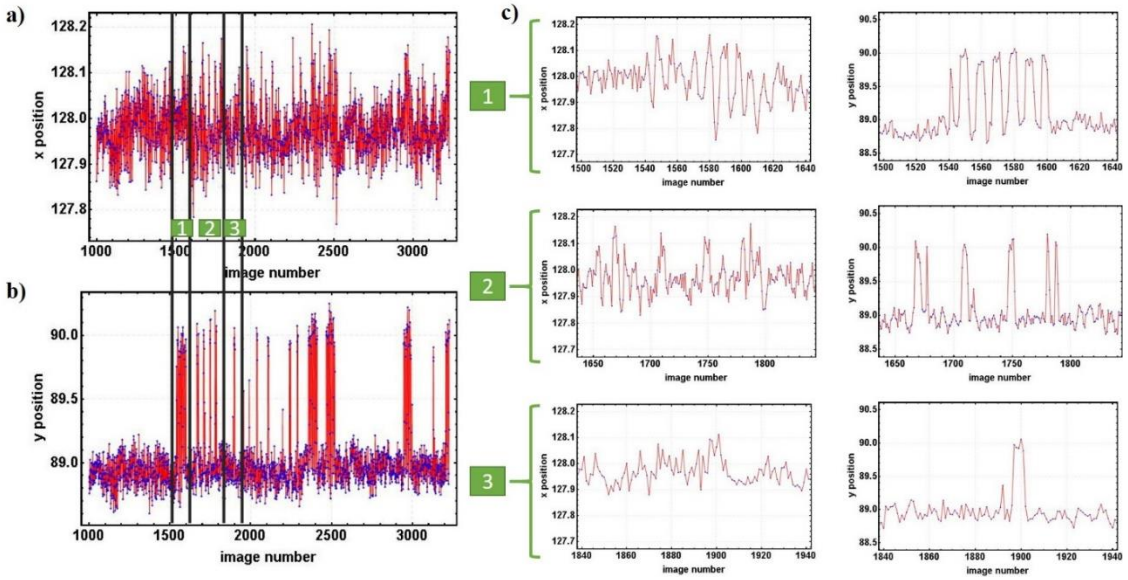

Figure 5.8. (a) and (b) phase shifts along x and y direction for 0.12 s due to different number of pulses. Zoom in plots are shown in green boxes in (c).

To observe the changes in the shift for individual and consecutive heat pulses, the zoom in plots of phase shift along x and y directions corresponding a pulse duration of 0.12 s pulse duration are shown in Figure 5.8c. As seen from the figures, while average shift in x direction is about 0.2 pixel, average shift in y direction is approximately 1.1 pixel. The value of total phase shift should be calculated in terms of π. By using the direct proportion relation, the average phase shifts are calculated as 0.011π and 0.051π in x and y directions, respectively. Using Pythagorean Theorem, two-dimensional total average phase shift is determined as 0.052π.

As mentioned in experimental part, in addition to experiments with laser heat pulses, a different experiment series based on unsteady temperature change measurements is also conducted. Hot air vortices are sent onto Al coated surface of fiber and variation in interference pattern is recorded by the CMOS camera. Shifts along x and y directions which stems from the hot air vortices are shown in Figure 5.9. It is clearly seen that phase shift along y-direction plays a dominant role in total phase shift behavior. It is worth noting that unsteady temperature changes cause some imbalances and oscillations in phase shifts (Figure 5.9).

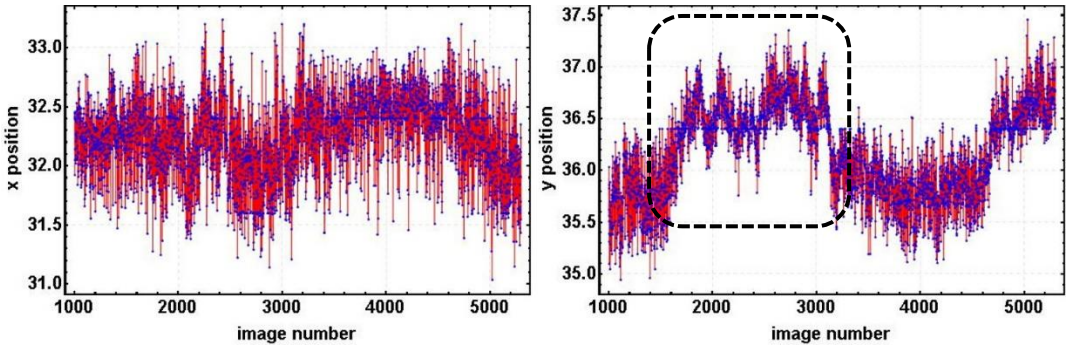

Figure 5.9. Shift in x and y directions for the application of hot air vortices. Green box focuses on the variation in phase shift due to unsteady temperature application.

Using schematically illustrated experimental setup in Figure 5.5, we obtain the base intensity measurements in the absence of hot air vortices. A further inspection of Figure 5.9b shows that we have a systematic change in the presence and in the absence of hot air vortices. For the first 700 frames in Figure 5.9b, there is no hot air vortices which is followed by the next 1700 frames in the presence of hot air vortices. In order to demonstrate reproducibility of the systematic change with and without hot air vortices, we repeated the previous two steps and show them in Figure 5.9b.

The only thing which can be obtained from the experiments is the total amount of phase shift due to the change in refractive index and physical length of the cores between each other. This is the left side of Equation 5.2. The right side of the equation will be verified by using FEM simulations.

5.5. Finite Element Simulations

Our experimental results give only the total amount of the phase shift. For some heat and temperature sensing studies, diffusion length cannot be determined by using the experimental data or theoretical calculations if the temperature or heat pulses are not applied from the axial direction. FEM simulations based theoretical calculations are performed in order to calculate the temperature diffusion length. Figure 5.10 demonstrates 3D fiber structure and each part of fiber (cores, cladding, air holes, and Al coated surface) is defined properly. Since laser heat pulse is applied from lateral surface, it is not possible to determine heat diffusion length by using the Equation 5.6.

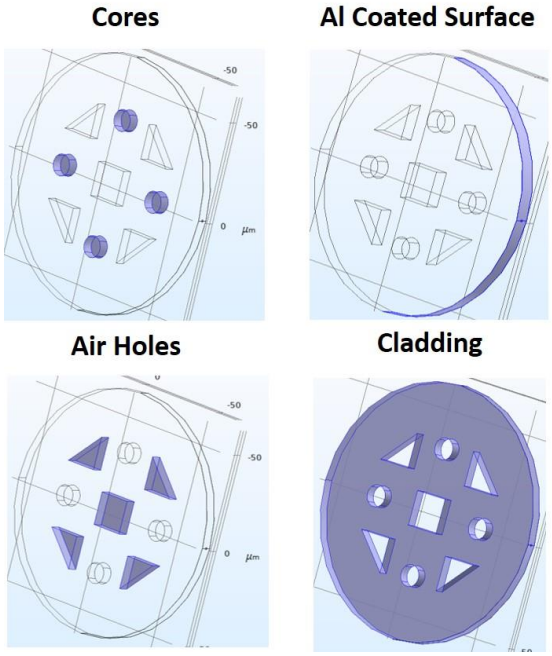

Figure 5.10. Highlighting the individual parts of multicore fiber-based FEM framework in 3D.

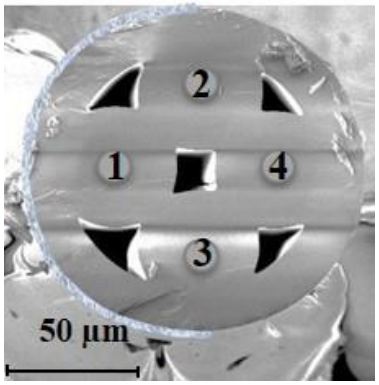

Figure 5.11. SEM image of the four-core optical fiber.

Figure 5.11 shows the SEM image of the four-core optical fiber. Heat pulses from the Nd:YAG laser are sent onto Al coated lateral surface of the optical fiber on provided that laser light is focused onto the first core which is shown by number 1 in the SEM image. In FEM simulations, average temperature variation is calculated for the first and the fourth core to determine the heat diffusion length. In these simulations, power value is increased starting from 50 mW to 150 mW with the steps of 10 mW to see the temperature rise depending on the power value of laser which is seen from Figure 5.12. In the experiments, the laser power

is set to 70 mW by using a density adjustable neutral density (ND) filter. While the first core experiences a temperature rise about 33.85 K, the temperature increase of the fourth core is about 29.5 K. As it is understood from the temperature increases, there is a heat dissipation throughout cross section of the optical fiber and this heat distribution reaches the fourth core. The temperature difference between the first and the fourth core is about 4.5 K for a power value of 70 mW and pulse duration of 0.12 s. By using the Equation 5.2, *l* is calculated 45.3 μm for the first core.

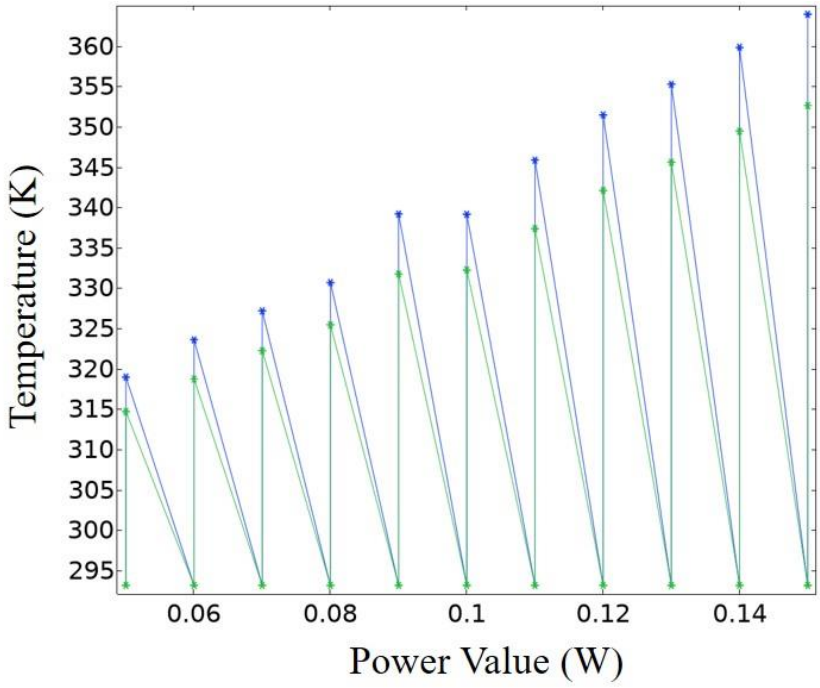

Figure 5. 12. Maximum average temperature increases in the first and fourth core of the optical fiber for different power values.

6. REFRACTOMETER WITH ETCHED CHIRPED FIBER BRAGG GRATING FABRY-PEROT INTERFEROMETER IN MULTICORE FIBER

6.1. Introduction

In recent years, fiber-optic refractometers based on Fiber Bragg gratings (FBGs) have been extensively studied because of their unique and impressive features such as compact size, simplicity in signal detection, and low cost. Different types of sensor structures have been employed, including regular FBGs [115], phase shifted FBGs [116, 16], tilted FBGs [117, 118, 18], or combination of them [119]. They can adapt to many different environments to measure RI changes in chemical [120] and biological compositions [121]. Some of fiber-optic refractometers can also measure temperature or other physical parameters simultaneously [122, 123]. For FBG-based refractometers, the sensing region of the fiber is obtained by etching the FBG part to reach the fiber core at the center of the fiber [124]. This process aims to expose the evanescent field of the core mode to the surrounding medium for refractive index (RI) measurement. The diameter of the fiber in the sensing region is reduced to just a few micrometers to reach the desirable sensitivity. Unfortunately, the amount of etching significantly reduces the mechanical strength of the sensor and also makes the sensor susceptible to physical perturbations, which is undesirable for practical applications.

In this project, we report a sensitive and mechanically robust fiber-optic refractometer with temperature compensation based on a Fabry-Perot interferometer (FPI) formed by two etched chirped fiber Bragg gratings (CFBGs) on a multicore fiber (MCF). The principle of operation is explained in Figure 6.1 using a seven-core MCF as an example. The arrangement of the cores before and after etching is schematically shown in Figure 6.1a. Only a small portion of the cladding needs to be removed to expose the optical field guided by the outer six cores to the ambient environment and the light guided in the center core is still confined within the fiber. For RI sensing, a pair of high-reflection CFBGs are fabricated on both the center core and outer cores of the fiber, as shown in Figure 6.1b. Each pair of CFBGs form a high-finesse FPI on each of the cores whose reflection spectrum features approximately equally spaced narrow spectral notches. The ambient RI affects the effective

RI of the outer cores only and causes spectral notch shifts of the corresponding CFBG-FPIs (Figure 6.1c). Temperature changes affect the effective RIs of both the outer cores and the center core in a similar way, causing almost identical shifts to both CFBG-FPIs (Figure 6.1d). As a result, the relative spectral shifts of the CFBG-FPIs can be used to measure the ambient RI with the temperature effect greatly suppressed. When a wavelength-scanning laser is used for demodulation, it also eliminates the errors caused by the wavelength drift of the laser. The narrow spectral notches of the sensor lead to high-resolution RI measurement using low-cost distributed feedback (DFB) lasers whose wavelength is scanned through injection-current modulation. Because only a relatively small layer of cladding is removed from in the sensing region, the sensor is rigid and robust. We note that other types of multicore fiber with various numbers of cores can be used in such experiment as long as the fiber has a reference central core as well as surrounding outer cores. The distance between outer cores and fiber center is critical to keep the sensor rigid and robust after etching.

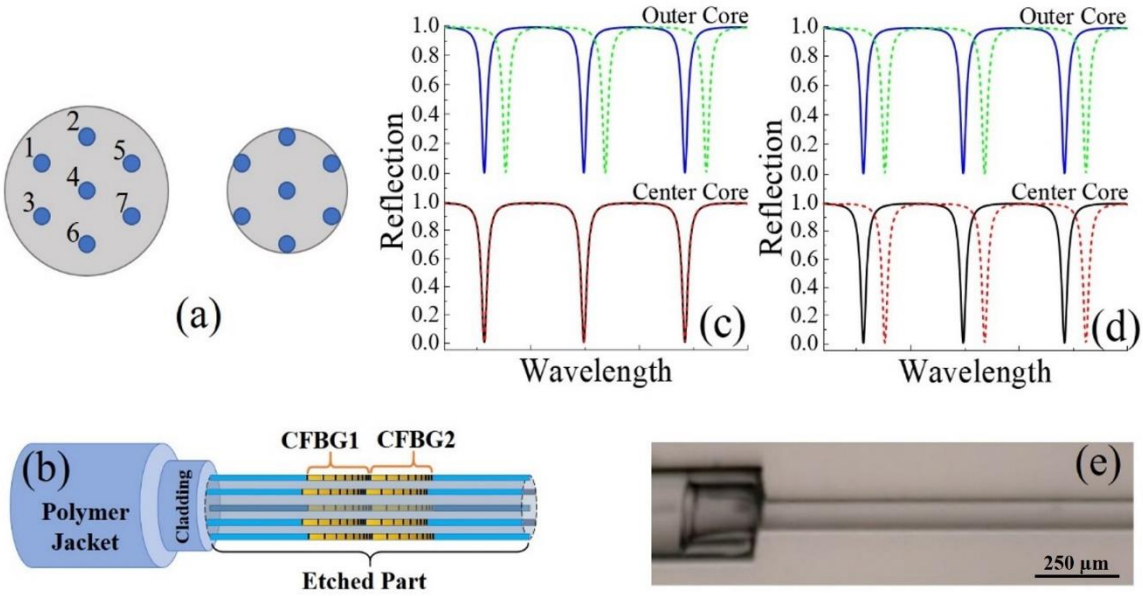

Figure 6.1. (a) Cross section of the seven-core fiber before (left) and after etching (right). (b) Schematic representation of the sensing structure of the seven-core fiber. (c) Spectral response of CFBG-FPIs in the outer core and the center core to ambient RI changes. (d) Spectral response of CFPG-FPIS in the outer core and the center core to the ambient temperature changes. (e) Optical microscope image of a fabricated RI sensor.

6.2. Experiment

The seven-core MCF used in our experiment had an outer diameter of 125 μm. The cores, each having a diameter of 9 μm and supporting single-mode operation in the 1550 nm region, form a hexagonal array with a core-to-core pitch of 37 μm. The fabrication of the sensor head involved two steps: 1) a pair of CFBGs each with a length of 7 mm were written into both the outer cores and the center core of the MCF to form a CFBG-FPI in each of the cores and 2) the cladding of a small length of the fiber including the CFBG-FPIs was etched by buffered hydrofluoric acid (BHF). More specifically, the first group of CFBGs were fabricated simultaneously on all seven cores of the MCF by a chirped phase mask (1067.7 nm period, 2.5 nm/cm chirping rate) based on the scanning beam technique using a 193 nm UV excimer laser [125]. The germanium doping of the MCF yielded strong two-photon absorption of the 193 nm UV laser, which allowed us to directly write FBGs on the fiber without hydrogen loading or other photosensitization processes [126]. Then the fiber was shifted in the axial direction to fabricate a second group of CBGs adjacent to the first group using the same setup. The length of each CFBG was 7 mm, limited by the size of the phase mask, resulting a 14 mm-long sensitive region. The chirping directions were the same for each of the CFBGs. During the CFBG writing process, the transmission spectrum of the center core (core 4 as shown in Figure 6.1a) was monitored using white light source along with an optical spectrum analyzer (OSA). The CFBG in the center core fabricated in the first UV exposure process showed a reflectivity of > 90% over a bandwidth of ~1.5 nm. After fabrication of the CFBG-FPI, the fiber was etched in the sensing region using BHF. During the etching process, the reflection spectra of the center and three outer cores were monitored. When the spectral notch wavelengths of CFBG-FPIs in the outer cores began to shift toward shorter wavelengths (blue shift), as a result of the evanescent field was being exposed to the surrounding liquid, the etching process was stopped. This occurred when the part of the cladding surrounding the outer cores was adequately removed. The total radial thickness of the removed cladding region was estimated to be about 12 μm, leaving an outer diameter of ~100 μm in the etched region of the fiber. The etching process of the cladding part took approximately two hours to reach the outer cores. As expected, there were not observable shifts in the reflection spectrum of the CFBG-FPI in the central core during the etching process. Figure 6.1e shows the optical microscope image of the etched fiber sensor head, which confirms the homogeneity in diameter throughout the etched fiber length.

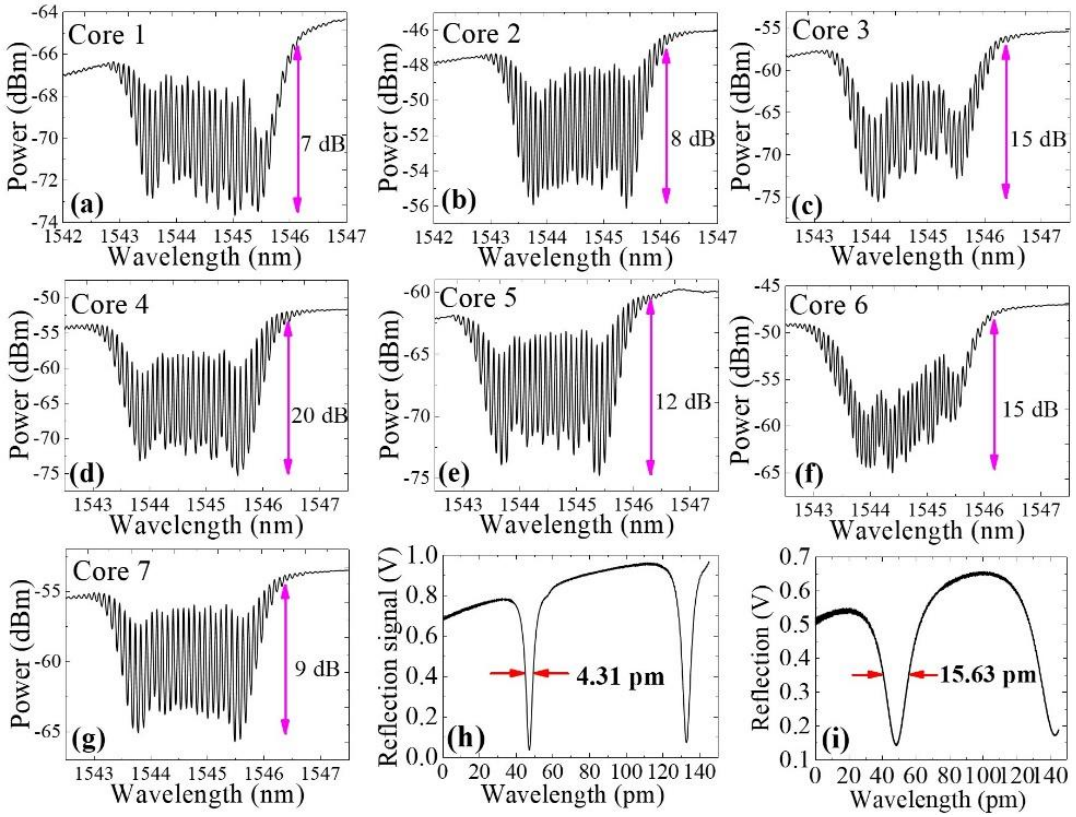

Figure 6.2. (a)-(g) Transmission spectra of the CFBG-FPIs in core 1-7, respectively, measured by an OSA with a spectral resolution of 20 pm. (h)-(i) Reflection spectrum of the FPI in cores 4 and 7, respectively, measured by a wavelength-scanning laser.

Figures 6.2(a)-(g) show the transmission spectra of the CFBG-FPIs in each core measured by an OSA with a spectral resolution of 20 pm. It is seen that the maximum transmission depth of the fringes, which is a measure of the fringe visibility, as well as the center wavelength of the CFBGs, were not uniform among these cores. We believe that the different locations of the cores relative to the UV beam led to the variations in the fabricated CFBGs on these cores. Specifically, the curvature from the cylindrical surface may result in non-uniform intensity distributions of the UV laser. To accurately measure the spectral width of the fringes, a wavelength-scanning DFB laser was used (described in more detail later). The spectral width was determined to be 4.3 pm for core 4 (center core) and 15.6 pm for core 7 (outer core), seen in Figure 6.2h and i. The larger spectral width for core 7 was due to the excessive optical loss of the core caused by etching that reduces the finesse of the FPI. The CFBG-FPIs in these two cores were chosen for RI sensing.

Experimental setup for RI sensor demonstration and performance evaluation is schematically shown in Figure 6.3. The light from a wavelength-scanning DFB laser operating at ~1545 nm was separated into two paths through a fiber coupler for demodulating the CFBG-FPIs in the outer and center cores. In each path, the light was directed to the pigtail fiber addressing that particular core in the MCF through a circulator. A polarization controller was included in each path before the circulator to ensure that the light polarization was aligned with one of the principal axes of the fiber in the grating region. The light reflected from the CFBG-FPI was directed to a photodetector by the circulator and recorded by a data acquisition (DAQ) system with a sampling rate of 2.0 MS/s and the data were stored in a computer for processing and analysis. Wavelength scanning of the DFB laser was achieved through injection current modulation. The current controller for the DFB laser was biased at 225 mA and modulated with a 500 Hz, 2 V (corresponding to 100 mA current) peak-to-peak triangle wave from a function generator to control the center wavelength and the scanning range of the laser. These values, together with the laser temperature, were selected to ensure that the wavelength scanning range of the laser could cover the full range of spectral shift for CFBG-FPIs in the center core and outer core. The function generator was also used to synchronize the DAQ system. A calibration of wavelength change vs. modulation voltage for the laser was performed following the method used in [127].

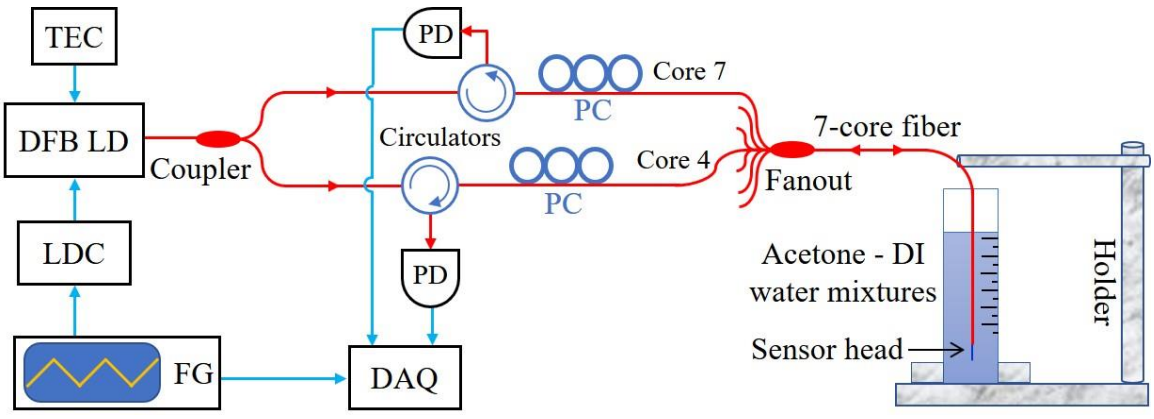

Figure 6.3. Schematic representation of the experimental setup: DFB LD: DFB laser diode, TEC: temperature controller, LDC: laser current controller, FG: function generator, DAQ: data acquisition, PD: photo diode, PC: polarization controller.

To demonstrate sensor operation for RI measurement and study its performance, the sensor head was immersed into 25 ml DI water and acetone was poured into the water with

steps of 1 ml. A total of 7 ml acetone was added to the water during the experiment with acetone concentration starting from 0% v/v and reaching approximately 21.9% v/v. The RI of the acetone/water solution n_M, is estimated using the following formula [128]:

$$n_M = n_W + C(n_A - n_W) \tag{6.1}$$

where n_W and n_A are RIs of the pure DI water and pure acetone, respectively, and C is the volume concentration of the acetone in the solution. Here, $n_W = 1.3164$ and n_A=1.3483 at the operating wavelength of ~1550 nm were used [129], corresponding to an increase of ~0.001 in RI for each ml acetone added to the solution.

6.3. Results and Discussions

As it is stated previously, the diameter of the cladding region is about 100 μm after the etching process is completed. The light guided by the outer cores extended out of the fiber and into the solution. Finite Element Simulations (FEM) simulations are carried out to demonstrate the difference of mode couplings (E_z field) for the following cases: i) before the etching process, ii) after the etching process, and iii) when the sensor head is placed into liquid mixture. Figure 6.4 shows the evolution of electromagnetic wave coupling as a response to these three cases. It is observed from FEM simulations that partial removal of cladding region diminishes the strength of the light coupling to the outer cores. This is demonstrated by showing the electric field distribution along z direction in the Figure 6.4d, e, and f. As it is clearly seen from Figure 6.4d, e and f that the inner core has a stronger coupling for all cases. During FEM simulations, all cores are illuminated simultaneously. It is worth noting that the cores can communicate with each other due to the short distances between them. Although there is no refractive index change in the cladding region, which surrounds the core in the center, there is a small change in the strength of the z-component of the electric field for the center core when the refractive index of the environment, which surrounds the outer cores, is changed. Because of that reason, in the experiment, a seven-core fiber fanout is used, light from a DFB laser diode is separated into seven beams, and all cores are illuminated separately.

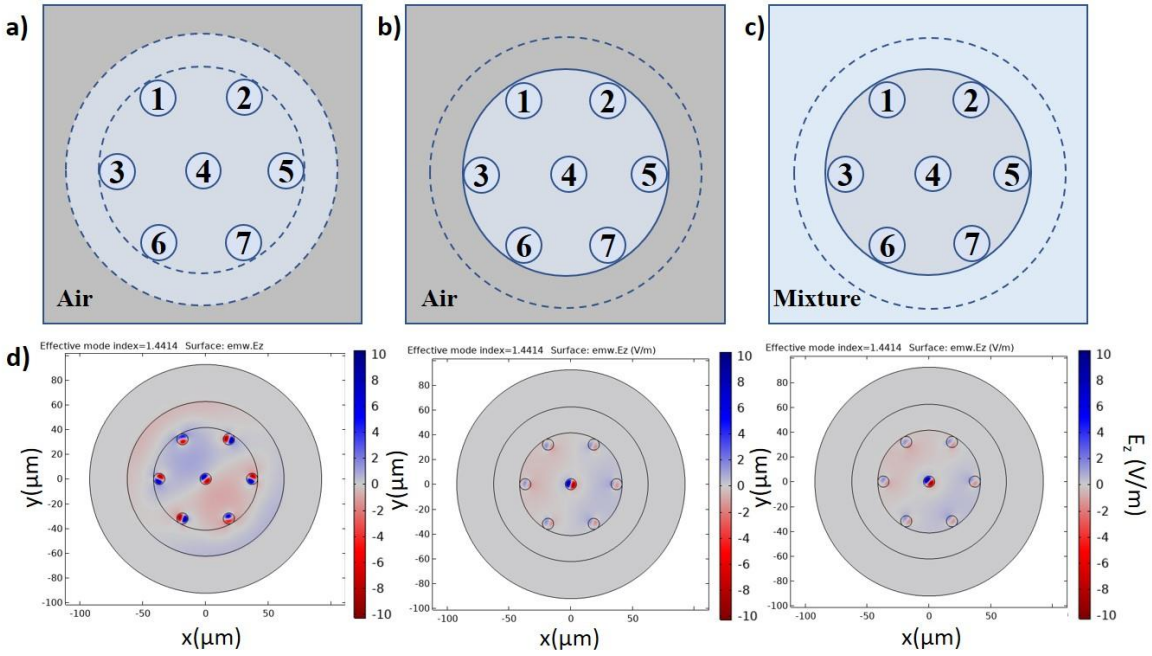

Figure 6.4. (a), (b), and (c) present the schematic representations of the fiber structure for the following cases: before etching process, after etching process, and when the sensor is placed into DI water- Ethanol mixture, respectively. (d), (e), and (f) demonstrate FEM analysis results of Electric Field (E_z) distribution of the fiber structure before etching process, after etching process, and when the sensor is placed into solution, respectively.

In the experiment, when the amount of acetone was increased with 1 ml steps, the reflection spectra of the CFPG-FPIs in the center core (core 4) and outer core (core 7) were measured using the set up shown in Figure 6.3 and the results are shown in Figure 6.4a and b for the center core and outer core, respectively. Although the light field guided by the center core was well confined inside the fiber and was not affected by the RI change of the solution, the fringes in the reflection spectrum shifted toward longer wavelength. The wavelength shift may result from a temperature increase of the solution. The wavelength drift of the DFB laser may cause the spectrum to have the appearance of shifting. Both the mixing of acetone and water and the ambient temperature changes may affect the temperature of the solution. The center wavelength of the DFB laser is also sensitive to the operation temperature of the laser diode. The light field guided by the outer core extended out of the fiber and into the solution. As expected, the fringes of the CFBG-FPI in the outer core experienced a larger shift toward longer wavelength because the increases led to red shifts of the spectrum. From the measured spectra, the wavelength positions of the fringe

valleys were obtained by a second-order polynomial curve fitting of the measured data around the fringe valleys. The wavelength shift as a function of RI of the solution is shown in Figure 6.4c for both CFBG-FPIs. The nonlinear responses of the spectral shift to RI can also be explained by the temperature changes of the solution and the wavelength drift of the DFB laser. These effects were removed by subtracting the wavelength shift of the central core notch from that of the outer core notch so that only the spectral shift corresponding to the RI change remained. The relative wavelength shift vs. the RI of the solution after removing the effects from temperature and laser drift is shown in Figure 6.4d. Linear fitting of the data reveals a good linearity of the sensor response to the RI of solution. The slope of the linear fitting gives the sensitivity of the refractometer as 1.43 nm/RIU (RIU: RI unit).

The calculation of the sensor sensitivity depends on the RI value of acetone at the operating wavelength (1550 nm). Based on our literature review, we came up with two different references for ethanol RI value [129,130]. We calculate and compare the resulting sensitivity values by using these two references. By taking the RI value of acetone (n_A) as 1.3483 from the reference paper [129], the sensitivity value of acetone was reported as 1.43 nm/RIU. As n_A is taken as 1.3515 from the reference paper [130], and thus the sensitivity is found as 1.30 nm/RIU for acetone. We know that sensitivity value of a fiber optic sensor is not material dependent. Because of that reason, the same experiment is also carried out for ethanol. If n_E is taken as 1.3522 from the reference paper [129], the slope of the linear fitting gives the sensitivity of the refractometer as 0.94 nm/RIU (RIU: RI unit). For the other reference [130] which reports n_E of ethanol as 1.3417, the sensitivity value is obtained as 1.34 nm/RIU. We note that the RI values for ethanol and acetone from Ref [130] gives consistent RI sensitivities of the sensor (1.34 nm/RIU for ethanol solution vs. 1.30 nm/RIU for the acetone solution) and the values from Ref. [129] lead to relatively large discrepancies (0.94 nm/RIU for ethanol solution vs. 1.43 nm/RIU for acetone solution).

During the etching process, when the spectral notch wavelengths of CFBG-FPIs start to shift toward shorter wavelengths, the etching process is stopped. This means that outer cores start to be exposed surrounding environment. Using some imaging methods like Optical Microscope or Scanning Electron Microscope (SEM), it is not possible to decide whether there is any core etching process or not. The amount of the core etching is very important for increasing the sensitivity of the sensor. To decide the right amount of the

etching rate of the fiber cores exactly, some further FEM simulations are necessary to carry out.

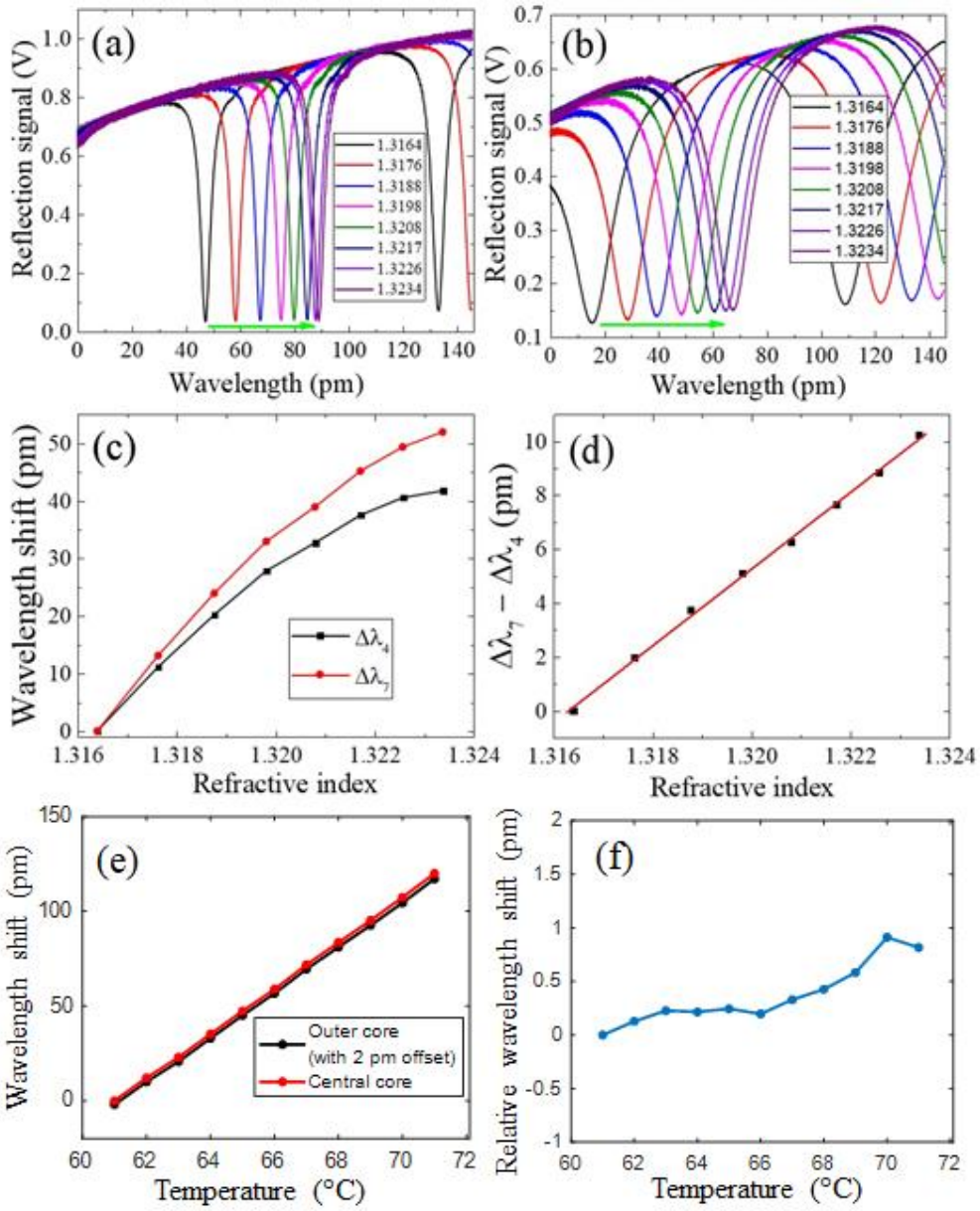

Figure 6.5. The reflection spectra around a spectral notch of the CFBG-FPIs in the center core (a) and in the outer core (b) measured by the wavelength scanning DFB laser immersed in solutions of different RIs. Wavelength shifts of the spectral notches as functions of the surrounding RI for the CFBG-FPIs in the center core (black) and in the outer core (red) (c). The relative wavelength shifts of between central core notch and the outer core notch vs. refractive index (d). The wavelength shift (e) and the relative wavelength shift (f) of the central core notch and an outer core notch vs. temperature. For clarity, a 2-pm offset was added to the results for the central core notch.

To further verify the capability of the sensor for temperature compensation, we measured the wavelength shifts of the center core notch and an outer core notch, using a tunable external cavity diode laser (Model 6328, New Focus), as a function of temperature and the results are shown in Figures 6.5(e) and (f). Both notches shifted ~119 pm over a 10 °C temperature change, showing similar temperature sensitivity of 11.9 pm/˚C. The relative wavelength shift was <1 pm over the same range, indicating that the temperature effect could be reduced by > 100 times.

For some fiber optic sensor applications, cladding region is usually removed by the etching method to expose the evanescent field to surrounding medium of the fiber core(s), which causes a variation in the wavelength on reflection spectrum. The amount of etching is one of the most critical parameters for the sensing studies. Since the etching process may cause a decrease in the mechanical strength of the sensor, the sensor can be affected by the physical perturbations easily [131], since the diameter of the fiber structure is reduced to a few micrometers to keep the sensitivity high. During the etching process, the total radial thickness removed from cladding region is approximately 12 μm and the new diameter of the optical fiber is about 100 μm which is very close to the initial diameter. Since only a small portion of the cladding region is removed, the sensor maintains an excellent mechanical strength.

Finally, we studied the noise performance and determined the detection limit of the fiber-optic refractometer system. We placed the sensor in DI water and continuously recorded 1000 frames of the spectra of both CFBG-FPIs in the center core and the outer core over a period of 2 s (with a frame rate of 500 Hz). For each frame, the wavelength shifts of the spectral notches for the CFBG-FPIs in the center core and the outer core were calculated and the relative wavelength shifts between these two spectral notches were used to gauge the RI. The results are shown as the black curve in Figure 6.6, from which the standard deviation was calculated to be 1.4×10^{-2} pm. Using the RI sensitivity of 1.43 nm/RIU obtained above, the detection limit, which describes the smallest RI change that can be resolved, is calculated to be 1.0×10^{-5} RIU at the background RI of ~1.316 measured at 1550 nm. It is noted that the fluctuations contributing to the standard deviation were most high-frequency noises, which can be effectively reduced out using a simple moving average filter. The red curve in Figure 6.6 is the results after applying a 50 data-point simple moving average. The

standard deviation was reduced to 3.4×10^{-3} pm, corresponding to a RI detection limit of 2.4×10^{-6} RIU at the background RI of ~1.316. The moving average reduces the effective measurement speed from 500 Hz to 10 Hz, which is sufficient for most applications involving RI measurement.

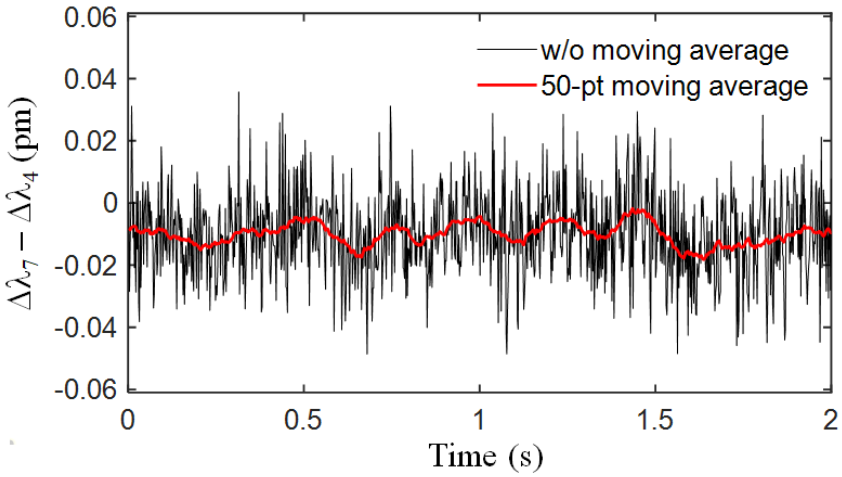

Figure 6.6. Difference in wavelength shifts between the spectral notches of the CFBG-FPIs in the central core and the outer core for RI at 1.316.

6. CONCLUSIONS

This thesis consists of four different fiber optic sensing mechanisms and their theoretical studies. In these studies and experiments, two different type of optical fibers are employed: four core and seven core optical fibers. In addition to the number of cores, different sensing mechanisms of these two optical fibers are generated. As an interferometric sensor is fabricated using a four-core optical fiber for detecting some physical parameters such as temperature, heat transfer rate, and strain, a Bragg grating is written into a seven core optical fiber to obtain a grating based fiber sensor to determine refractive index changes in various liquids.

In the first project, a four-core optical fiber is introduced as a calorimetric gauge for heat transfer rates and temperature sensing measurements using intrinsic features of the fused silica material. Because the optical fiber is transparent to the laser light at 532 nm, the cross-sectional end face of the fiber is coated with Aluminum (Al). Interference pattern is combination of vertical, horizontal, and diagonal interferograms in the reflection spectrum. Heat pulses from an Nd:YAG laser are sent onto one targeted optical fiber core, which results in an optical path length difference between the four guiding cores. Heat pulses are applied to the fiber end face to allow the heat penetration along the fiber core and to treat the four-core fiber as a calorimetric gauge. Thus, causing a phase shift in the interference pattern depending on the power of the laser pulses. The amount of total phase shift is calculated from the experimental part and helps us to calculate the temperature rise and accumulated heat inside the fiber core. In addition to these parameters, diffusion length is also calculated to determine the minimum sensor length.

In the second section, a novel temperature sensing mechanism is demonstrated for the strain measurement employing again a four-core optical fiber. Interference pattern in transmission spectrum is obtained and the intrinsic and interferometric features of the four-core optical fiber are used. A few inches length of the four-core fiber is winded very tightly around a stainless-steel cylinder which is placed onto a heater to increase the temperature to cause a thermal expansion of the metal cylinder. This results in a phase shift in the interference pattern and a shear strain in the fiber core as a result of optical path difference

between inner and outer core pairs. In conclusion, phase shift provides to find the amount of the strain.

As a third study, a four-core fiber is proposed and demonstrated for temperature sensing and heat transfer rate measurements, successfully. Cladding region with a length of 4-5 cm is removed from the center part of the optical fiber to coat half of this surface with Al. Laser heat pulses from Nd:YAG laser of 532 nm are sent onto this Al coated surface, which results in a variation in the interference pattern in the transmission scheme as a result of change in the refractive index and physical lengths of the cores. These heat pulse applications cause a heat dissipation among the fiber cores. Applying heat pulses also causes thermal expansion in the radial direction, which is negligible when it is compared to the thermal expansion in the axial direction. In addition to experiments with laser heat pulses, a different experiment series based on unsteady temperature change measurements is also conducted. Hot air vortices were sent onto Al coated surface of the fiber and variations in interference pattern are recorded by a CMOS camera. These hot air vortices cause phase shifts along x and y directions. It was clearly seen that the phase shift along y-direction plays a dominant role in total phase shift behavior. It is worth noting that the unsteady temperature changes cause some imbalances and oscillations in the phase shifts.

Unlike the aforementioned two studies, in the third section, a seven-core optical fiber with two fiber Bragg gratings is employed to detect the refractive index changes of the surrounding environment. A fiber optic refractometer based upon CFBG-FPIs fabricated on both the center core and outer cores of a seven-core MCF is demonstrated. A small portion of the fiber cladding is etched by using BHF to expose the optical fields in the outer core to the surrounding environment. The total length of the CFBG-FPIs is 14 mm and the diameter of the fiber after etching process is approximately 100 μm which is the evidence that the optical fiber sensor maintains the rigidity. The reflection spectrum of each CFBG-FPI, measured using low-cost DFB diode lasers with high resolution, had a series of narrow spectral notches and the relative wavelength shift between the fringes of the two CFBG-FPIs in one of the outer cores and the center core is used for RI measurement. As the outer cores are affected by both temperature and refractive index change, the center core is only affected by the temperature. The wavelength shift due to the refractive index change is obtained by subtracting the wavelength shift of the center core from the wavelength shift of outer core.

The refractometer exhibits a sensitivity of 1.43 nm/RIU with good linearity and a detection limit of 2.4×10^{-6} RIU with an effective measurement speed of 10 Hz around a background RI of 1.316.

As a future work, because laser heat pulses are applied from Al coated lateral surface of the optical fiber, it is not possible to determine the diffusion length and minimum sensor length without any heat loss using the heat diffusion equation in the last project of this thesis. Further finite element simulations can be carried out to decide the heat diffusion length in the axial direction. For the project titled as Refractometer with Etched Chirped Fiber Bragg Grating Fabry-Perot Interferometer in Multicore Fiber, we cannot obtain any information about the core etching rate using some imaging methods such as SEM or optical microscope. It is known that the etching rate of the fiber core plays a significant role in the sensitivity performance. If the amount of etching rate for fiber cores is increased, the sensitivity of the sensor increases. Hence, as a future work, some further FEM simulations can be carried out to theoretically determine the etching rate. For the first study, we assumed that the heat distribution occurs inside the targeted fiber core and the radial heat distribution does not reach the other cores due to the air holes. Some further FEM simulations can help for the observation of a 3D heat distribution and the verification of that whether the temperature distribution reaches the other cores or not.

APPENDIX A: Phase Calculations for Interferometers

A.1. Mach Zehnder Interferometer

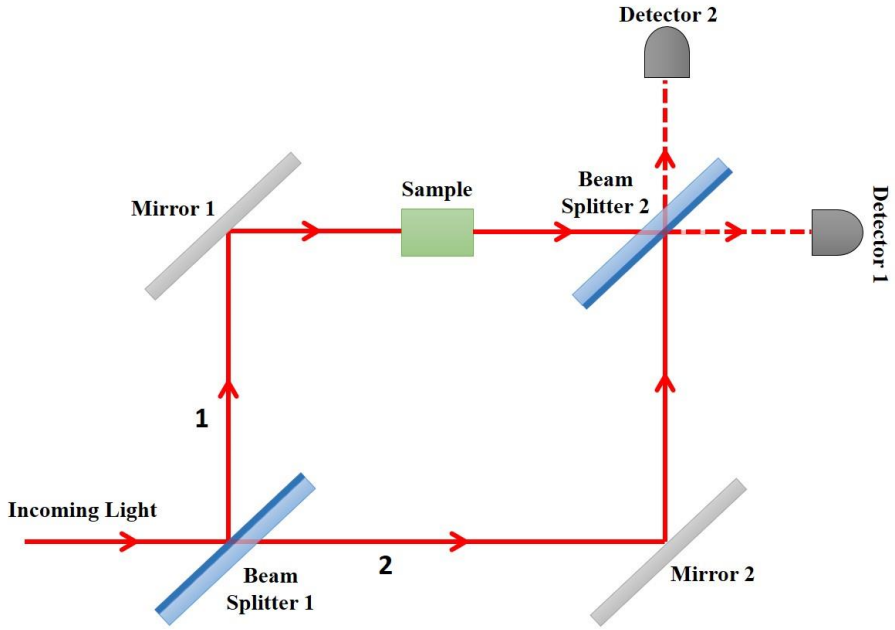

Figure A.1. Schematic representation of Mach Zehnder Interferometer.

The working mechanism of MZI is based on the path difference of two beams. Using the first beam splitter, incoming light is split into two beams and they are reflected by two mirrors. Reflected beams are recombined by the second beam splitter and sent to photodetectors. Reflected light will experience π phase shift. In addition to this phase shift, as light is transmitted in beam splitters, it also experiences a phase shift.

Detector 1: While first light beam experiences two reflections from beam splitter 1 and mirror 1, one transmission occurs passing through beam splitter 2. This results in a phase shift of 2π and $2\pi\left(\frac{l_1+d}{\lambda}\right)$ due to reflections and transmission, respectively. The total phase is given by the following formula [5, 73]:

$$\emptyset_1 = 2\pi + 2\pi\left(\frac{l_1 + d}{\lambda}\right) \tag{A.1}$$

where l_1 and l_2 are the total path lengths from the source to detectors for the first beam and second beam, λ is the wavelength of the light source, and d is the optical path length through the beam splitters. Optical path length is the product of the total path length and the refractive index of the beam splitters.

While second light beam experiences two reflections from mirror 2 and beam splitter 2 and mirror 1, one transmission occurs passing through beam splitter 1. This results in a phase shift of 2π and $2\pi\left(\frac{l_2+d}{\lambda}\right)$ due to reflections and transmission, respectively. For the second beam, the total phase is:

$$\emptyset_2 = 2\pi + 2\pi\left(\frac{l_2 + d}{\lambda}\right) \tag{A.2}$$

The phase shift difference between two beams:

$$\emptyset_1 - \emptyset_2 = 2\pi\left(\frac{l_1 - l_2}{\lambda}\right) = \delta \tag{A.3}$$

Detector 2: While first light beam experiences two reflections from beam splitter 1 and mirror 1, two transmission occur passing through beam splitter 2. This results in a phase shift of 2π and $2\pi\left(\frac{l_1+2d}{\lambda}\right)$ due to reflections and transmission, respectively. The total shift is given by the following formula:

$$\emptyset_1 = 2\pi + 2\pi\left(\frac{l_1 + 2d}{\lambda}\right) \tag{A.4}$$

While second light beam experiences one reflection from mirror 2, two transmissions occur passing through beam splitter 1 and beam splitter 2. This results in a phase shift of π and $2\pi\left(\frac{l_2+2d}{\lambda}\right)$ due to reflection and transmissions, respectively. For the second beam, the total phase shift is:

$$\emptyset_2 = \pi + 2\pi\left(\frac{l_2 + 2d}{\lambda}\right) \tag{A.5}$$

The phase shift difference between two beams:

$$\emptyset_1 - \emptyset_2 = \pi + 2\pi\left(\frac{l_1 - l_2}{\lambda}\right) = \pi + \delta \tag{A.6}$$

If it assumed that $\delta = 0$,

Detector 1: Because $\emptyset_1 - \emptyset_2 = 0$, a constructive interference occurs.

Detector 2: Because $\emptyset_1 - \emptyset_2 = \pi$, a destructive interference occurs.

By changing δ value, it is possible to obtain partially destructive or constructive interference pattern. As seen from the Figure A.1, a sample can be placed to introduce a path difference between two beams.

A.2. Fabry Perot Interferometer

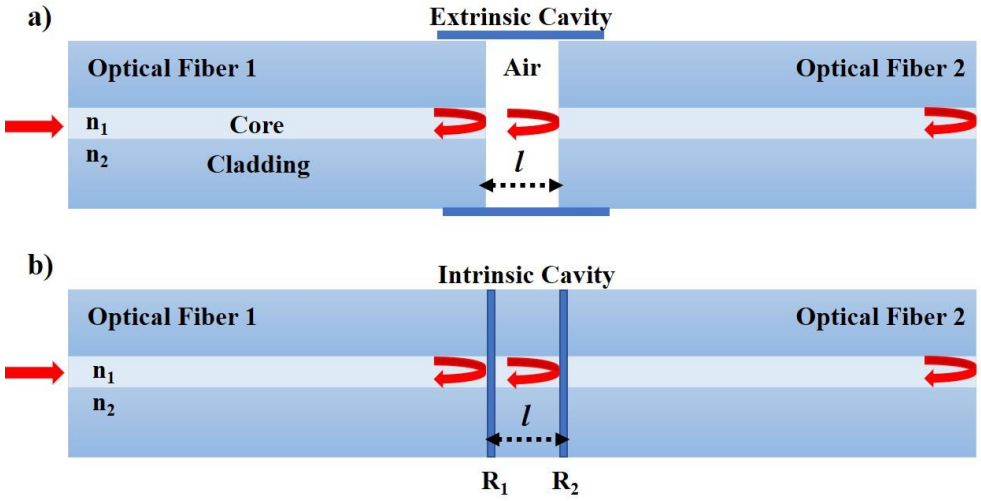

Figure A.2. Fabry Perot Interferometer with a) extrinsic and b) intrinsic cavity.

The phase difference is calculated by using the following formula [5]:

$$\delta = 2\pi\left(\frac{n2l}{\lambda}\right) \tag{A.7}$$

where l the length of the extrinsic or intrinsic cavity, n is the refractive index of the cavity, and λ is the wavelength of the light source. When an external parameter is applied to the sensing region, this results in an optical path difference.

A.3. Sagnac Interferometer

The phase difference is calculated by using the following formula [5]:

$$\delta = 2\pi\left(\frac{|n_f - n_s|l}{\lambda}\right) \tag{A.8}$$

where l the length of the sensing fiber, λ is the wavelength of the light source, and n_f and n_s are the refractive index of the fast and slow modes, respectively.

REFERENCES

1. Roriz, P., S. Silva, O. Frazão, and S. Novais, "Optical Fiber Temperature Sensors and Their Biomedical Applications", *Sensors*, Vol. 20, No. 7, Article number: 2113, 2020.

2. Sabri, N., S. A. Aljunid, M. S. Salim, and S. Fouad, "Fiber Optic Sensors: Short Review and Applications", *Recent Trends in Physics of Material Science and Technology*, Springer Series in Materials Science, Vol. 204, pp. 299-311, 2015.

3. Gholamzadeh, B. and H. Nabovati, "Fiber Optic Sensors", *World Academy of Science, Engineering and Technology, International Journal of Electrical, Computer, Energetic, Electronic and Communication Engineering*, Vol. 2, No. 6, pp.1107-1117, 2008.

4. Annamdas, V. G. M., "Review on Developments in Fiber Optical Sensors and Applications", *International Journal of Materials Engineering*, Vol. 1, No. 1, pp. 1-16, 2011.

5. Lee, B. H., Y. H. Kim, K. S. Park, J. B. Eom, M. J. Kim, B. S. Rho, and H. Y. Choi, "Interferometric Fiber Optic Sensors", *Sensors*, Vol. 12, No. 3, pp. 2467-2486, 2012.

6. Hocker, G. B., "Fiber-Optic sensing of Pressure and Temperature", *Applied Optics*, Vol. 18, No. 9, pp. 1445-1448, 1979.

7. Chana, K. S., S. R. Kidd, I. W. Matthews, J. S. Barton, and J. D. C. Jones, "Optical Fibre Fabry-Perot Interferometers for Calorimetric Heat Transfer Gauges", *Defence Research Agency*, Farnborough, United Kingdom, 1992.

8. Inci, M. N., S. R. Kidd, J. S. Barton, and J. D. C. Jones, "High temperature miniature fibre optic interferometric thermal sensors", *Measurement Science Technology*, Vol. 4, No. 3, pp. 382-387, 1993.

9. Meng, H., W. Shen, G. Zhang, X. Wu, W. Wang, C. Tan, and X. Huang, "Michelson interferometer-based fiber-optic sensing of liquid refractive index", *Sensors and Actuators B: Chemical*, Vol. 160, No. 1, pp. 720-723, 2011.

10. Gander, M. J., E. A. C. Galliot, R. McBride, J. D. C. Jones, J. G. Burnett, and A. H. Greenaway, "Bend measurement using multicore optical fiber," *12th International Conference on Optical Fiber Sensors*, OSA Technical Digest Series, Vol. 16, paper OWC6, 1997.

11. Yuan, L. and X. Wang, "Four-beam single fiber optic interferometer and its sensing characteristics", *Sensor Actuators A: Physical*, Vol. 138, No. 1, pp. 9-15, 2007.

12. Romaniuk, R. and J. Dorosz, "Temperature sensor based on double core optical fibre," *Proceedings of SPIE-Optical Techniques for Environmental Sensing, Workplace Safety, and Health Monitoring*, Vol. 4887, 2012.

13. Nguyen, L. V., S. C. W. Smith, H. E. Heidepriem, and T. M. Monro, "Interferometric high temperature sensor using suspended-core optical fibers", *Optics Express*, Vol. 24, No. 8, pp. 8967-8977, 2016.

14. Liu, G. G., Q. W. Sheng, D. Dam, J. Hua, W.L. Hou, and M. Han, "Self-gauged fiber-optic micro-heater with operation temperature above 1000 °C", *Optics Letters*, Vol. 42, No. 7, pp. 1412-1415, 2017.

15. Hill, K. O., Y. Fujii, D. C. Johnson, and B. S. Kawasaki, "Photosensitivity in optical fiber waveguides: application to reflection fiber fabrication", *Applied Physics Letters*, Vol. 32, No. 10, pp. 647-649, 1978.

16. Zhou, W., X. Dong, L. Y. Shao, C.C. Chan, C. L. Zhao, and P. Shum, "Compact refractometer based on extrinsic-phase-shift fiber Bragg grating", *Sensors and Actuators A: Physical*, Vol. 168, No. 1, pp. 46-50, 2011.

17. Z. Cai, F. Liu, T. Guo, B. O. Guan, G. D. Peng, and J. Albert, "Evanescently coupled optical fiber refractometer based a tilted fiber Bragg grating and a D-shaped fiber", *Optics Express*, Vol. 23, No. 16, pp. 20971-20976, 2015.

18. Guo, T., H. Y. Tam, P. A. Krug, and J. Albert, “Reflective tilted fiber Bragg grating refractometer based on strong cladding to core recoupling”, *Optics Express*, Vol. 17, No. 7, pp. 5736-5742, 2009.

19. Li, T., X. Dong, C. C. Chan, C. L. Zhao, and S. Jin, “Power-Referenced Optical Fiber Refractometer Based on a Hybrid Fiber Grating”, *IEEE Photonics Technology Letters*, Vol. 23, No. 22, pp. 1706-1708, 2011.

20. Jung, J., H. Nam, B. Lee, J. O. Byun, and N. S. Kim, "Fiber Bragg grating temperature sensor with controllable sensitivity", *Applied Optics*, Vol. 38, No. 13, pp. 2752-2754, 1999.

21. Mohammed, N. A, T. A. Ali, and M. H. Aly, "Evaluation and performance enhancement for accurate FBG temperature sensor measurement with different apodization profiles in single and quasi-distributed DWDM systems", *Optics and Lasers in Engineering*, Vol. 55, pp. 22-34, 2014.

22. Liu, Z., G. Liu, Y. Zhu, Q. Sheng, X. Wang, Y. Liu, Z. Jing, W. Peng, and M. Hang, "Unambiguous Peak Identification of a Silicon Fabry-Perot Temperature Sensor Assisted with an In-Line Fiber Bragg Grating", *Journal of Lightwave Technology*, Vol. 37, No. 17, pp. 4210-4215, 2019.

23. Singh, A. K., S. Berggren, Y. Zhu, M. Han, and H. Huang "Simultaneous strain and temperature measurement using a single fiber Bragg grating embedded in a composite laminate", *Smart Materials and Structures*, Vol. 26, No. 11, 2017.

24. Huang J., Z. Zhou, D. Zhang, and Q. Wei, "A Fiber Bragg Grating Pressure Sensor and Its Application to Pipeline Leakage Detection", *Advances in Mechanical Engineering*, 2013.

25. Meltz, G., W. W. Morey, and W. H. Glenn, "Formation of Bragg gratings in optical fibers by a transverse holographic method", *Optics Letters*, Vol. 14, No.15, pp. 823-825, 1989.

26. Morey, W. W., G. Meltz, and W. H. Glenn, "Fiber Optic Bragg Grating Sensors", *Proceedings of SPIE-Fiber Optic and Laser Sensors VII*, Vol. 1169, 1990.

27. Gasulla, I., D. Barrera, J. Hervás, and S. Sales, "Spatial Division Multiplexed Microwave Signal processing by selective grating inscription in homogeneous multicore fibers", *Scientific Reports*, Vol. 7, Article number:41727, 2017.

28. Cranch, G. A. and G. M. H. Flockhart, "Multicore fiber curvature sensor", US Patent 7324714B1, 2008.

29. Davis, M. A., D. G. Bellemore, M. A. Putnam, and A. D. Kersey, "Interrogation of 60 fibre Bragg grating sensors with microstrain resolution capability", *Electronics Letters*, Vol. 32, No. 15, pp. 1393-1394, 1996.

30. Amiri, I. S., S. R. B. Azzuhri, M. A. Jalil, H. M. Hairi, J. Ali, M. Bunruangses, P. Yupapin, "Introduction to Photonics: Principles and the Most Recent Applications of Microstructures", *Micromachines*, Vol. 9, No. 9, pp. 452, 2018.

31. Ferreira, M. F. S., E. Castro-Camus, D. J. Ottaway, J. M. López-Higuera, X. Feng, W. Jin, Y. Jeong, N. Picqué, L. Tong, B. M. Reinhard, P. M Pellegrino, A. Méndez, M. Diem, F. Vollmer, and Q. Quan, "Roadmap on optical sensors", *Journal of Optics*, Vol. 19. No. 8, pp. 083001, PMID: 29375751, PMCID: PMC5781231, 2017.

32. Fernandez-Vallejo, M. and M. Lopez-Amo, "Optical Fiber Networks for Remote Fiber Optic Sensors", *Sensors*, Vol. 14, No. 4, pp. 3929-3951, 2012.

33. Wu, T., G. Liu, S. Fu and F. Xing, **"**Recent Progress of Fiber-Optic Sensors for the Structural Health Monitoring of Civil Infrastructure**"**, *Sensors*, Vol. 20, No. 16, pp. 4517, 2020.

34. Annamdas, K. K. K. and V. G. M. Annamdas, **"**Review on developments in fiber optical sensors and applications**"**, *Proceedings of Fiber Optic Sensors and Applications VII*, Vol. 7677, pp. 76770R, 2010.

35. Wang, B., F. Zhang, F. Pang and T. Wang, **"**An optical fiber humidity sensor based on optical absorption**",** *Proceedings of Optical Sensors and Biophotonics III*, Vol. 8311, pp. 83112A, 2011.

36. Nguyen, T. H., T. Venugopalan, T. Sun and K. T. V. Grattan, **"**Intrinsic Fiber Optic pH Sensor for Measurement of pH Values in the Range of 0.5–6**",** *IEEE Sensors Journal*, Vol. 16, No. 4, pp. 881-887, 2016.

37. Di Sante, R., **"**Fibre Optic Sensors for Structural Health Monitoring of Aircraft Composite Structures: Recent Advances and Applications**",** *Sensors*, Vol. 15, No. 8, pp. 18666-18713, 2015.

38. Othonos, A., **"**Bragg Gratings in Optical Fibers: Fundamentals and Applications**"**, *Optical Fiber Sensor Technology*, Springer, Boston, MA, pp. 79-187, 2000.

39. Personick, S., **"**Review of fundamentals of optical fiber systems**"**, *IEEE Journal on Selected Areas in Communications*, Vol. 1, No. 3, pp. 373-380, 1983.

40. Addanki, S., I. S. Amiri and P. Yupapin, **"**Review of optical fibers-introduction and applications in fiber lasers**"**, *Results in Physics*, Vol. 10, pp. 743-750, 2018.

41. Anuszkiewicz, A., R. Kasztelanic, A. Filipkowski, et al. **"**Fused silica optical fibers with graded index nanostructured core**"**, *Scientific Reports*, Vol. 8, Article number: 12329, 2018.

42. Viswanathan, N. K., **"**Guided Wave Optical Components and Devices**"**, CHAPTER 16 - Enhancing Photosensitivity in Optical Fibers, *Chapter Academic Press*, pp. 243-250, 2006.

43. Jenkins, F. A. and H. E. White, "Fundamentals of Optics, Fourth Edition", Laws of Reflection and Refraction, *The McGraw-Hill Companies*, 1976.

44. Gardner, C. S. and George Papen, "22 - Optical Communications", *Reference Data for Engineers (Ninth Edition)*, pp. 22-1-22-28, 2002.

45. Elliott, D. J., "Ultraviolet Laser Technology and Applications", Chapter 5 - UV Optics and Coatings, *Academic Press*, pp. 123-171, 1995.

46. Saleh, B. E. A. and M. C. Teich, **"**Fundamentals of Photonics**"**, New York, Wiley, 1991.

47. Wang, Q., G. Farrell and W. Yan, **"**Investigation on Single-Mode–Multimode– Single-Mode Fiber Structure**"**, *Journal of Lightwave Technology*, Vol. 26, No. 5, pp. 512-519, 2008.

48. Massa, N. M., **"**Fundamentals of Photonics**"**, Fiber Optic Telecommunication, Chapter 8, *eBooks of SPIE,* https://doi.org/10.1117/3.784938.ch8, 2008.

49. Ramaswami, R., K. N. Sivarajan, and G. H. Sasaki, **"**Chapter 2 - Propagation of Signals in Optical Fiber**"**, *Optical Networks (Third Edition)*, pp. 47-112, 2010.

50. Chen, X., S. R. Bickham, J. S. Abbott, J. D. Coleman, and M. J. Li, "Multimode Fibers for Data Centers"**,** *Handbook of Optical Fibers*, Springer, Singapore, 2018.

51. Ortiz, A. M. and R. L. Sáez, "Multi-Core Optical Fibers: Theory, Applications and Opportunities"**,** *Selected Topics on Optical Fiber Technologies and Applications*, IntechOpen, DOI: 10.5772/intechopen.72458, 2017.

52. Singh, K. and G. Kaur, "Multi-Core Fibers: An Overview"**,** *Conference: International Conference on Emerging Technologies in Electronics & Communication (ICETEC-13)*, Vol. 1, 2013.

53. Hayashi, T., T. Nakanishi, K. Hirashima, O. Shimakawa, F. Sato, K. Koyama, A. Furuya, Y. Murakami, and T. Sasaki, "125-μm-Cladding Eight-Core Multi-Core Fiber Realizing Ultra-High-Density Cable Suitable for O-Band Short-Reach Optical Interconnects", *Journal of Lightwave Technology*, Vol. 34, No. 1, pp. 85-92, 2016.

54. Awaji, Y., J. Sakaguchi, B. J. Puttnam, R. S. Luís, J. M. D. Mendinueta, W. Klaus, and N. Wada, "High-capacity transmission over multi-core fibers", *Optical Fiber Technology*, Vol. 35, pp. 100-107, 2017.

55. Epstein, M., "Fiber optics in medicine", *Critical Reviews in Biomedical Engineering*, Vol. 7, No. 2, pp. 79-120, 1982.

56. Lee, B., "Review of the present status of optical fiber sensors", *Optical Fiber Technology*, Vol. 9, No. 2, pp. 57-79, 2003.

57. Wiora, G., M. Weber, and S. Chanbai, "Optical Interferometry", *Encyclopedia of Tribology*, Springer, Boston, MA, 2013.

58. Statkiewicz-Barabach, G., J. Olszewski, P. Mergo, and W. Urbanczyk, “Hydrostatic Pressure and Temperature Measurements Using an In-Line Mach-Zehnder Interferometer Based on a Two-Mode Highly Birefringent Microstructured Fiber”, *Sensors*, Vol. 17, No. 7, Article number:1648, 2017.

59. Fabry, C and A. Perot, **“**Theorie et applications d'une nouvelle methode de spectroscopie interferentielle**”**, *Annales de chimie et de physique*, Vol. 16, No. 7, pp.115-144, 1899.

60. Perot, A. and C. Fabry, “On the Application of Interference Phenomena to the Solution of Various Problems of Spectroscopy and Metrology”, *Astrophysical Journal*, Vol. 9, pp. 87, 1899.

61. Liu, G., J. Philtron, Y. Zhu, J. L. Rose and M. Han, “Detection of Fundamental Shear Horizontal Guided Waves Using a Surface-Bonded Chirped Fiber-Bragg-Grating Fabry–Perot Interferometer”, *Journal of Lightwave Technology*, Vol. 36, No. 11, pp. 2286-2294, 2018.

62. Gong, Y., Y. J. Rao, Y. Guo, Y. Wu and Z. L. Ran, “Micro fiber-optic Fabry-Perot interferometer fabricated by chemical etching of Er-doped fiber”, *Proceeding of SPIE 20th International Conference on Optical Fibre Sensors*, Vol. 7503, 2009.

63. Nespereira, M., J. M. P. Coelho and J. M. Rebordão, “A Refractive Index Sensor Based on a Fabry–Perot Interferometer Manufactured by NIR Laser Microdrilling and Electric Arc Fusion”, *Photonics*, Vol. 6, No. 4, pp. 109, 2019.

64. Zhang, W., R. Wang, Q. Rong, X. Qiao, T. Guo, Z. Shao, J. Li, and W. Ma, “An optical fiber Fabry-Perot interferometric sensor based on functionalized diaphragm for ultrasound detection and imaging”, *IEEE Photonics Journal*, Vol. 9, No. 3, pp. 1-8, 2017.

65. Zhu, Y., Q. Sheng and M. Han, “Effect of Laser Polarization on Fiber Bragg Grating Fabry-Perot Interferometer for Ultrasound Detection”, *IEEE Photonics Journal*, Vol. 12, No. 4, pp. 1-8, 2020.

66. Shrivastav, A. M., D. S. Gunawardena, Z. Liu, et al., “Microstructured optical fiber based Fabry–Pérot *interferometer* as a humidity sensor utilizing chitosan polymeric matrix for breath monitoring”, *Scientific Reports*, Vol. 10, Article number: 6002, 2020.

67. Flores, R., R. Janeiro, and J. Viegas, “Optical fibre Fabry-Pérot interferometer based on inline microcavities for salinity and temperature sensing”, *Scientific Reports*, Vol. 9, Article number: 9556, 2019.

68. Chen, Z., S. Xiong, S. Gao, H. Zhang, L. Wan, X. Huang, B. Huang, Y. Feng, W. Liu, and Z. Li, “High-Temperature Sensor Based on Fabry-Perot Interferometer in Microfiber Tip”, *Sensors*, Vol. 18, No. 1, 2018.

69. Wei, H., M. Chen, and S. Krishnaswamy, “Three-dimensional-printed Fabry–Perot interferometer on an optical fiber tip for a gas pressure sensor”, *Applied Optics*, Vol. 59, No. 7, 2020.

70. Yu, Q. and X. Zhou, “Pressure sensor based on the fiber-optic extrinsic Fabry-Perot interferometer”, *Photonic Sensors*, Vol. 1, pp. 72–83, 2011.

71. Zehnder, L., “Ein neuer Interferenzrefraktor”, *Zeitschrift für Instrumentenkunde*, Vol. 11: pp. 275–285, 1891.

72. Mach, L., “Ueber einen Interferenzrefraktor”, *Zeitschrift für Instrumentenkunde*, Vol. 12, pp. 89–93, 1892.

73. Zetie, K. P., S. F. Adams, and R. M. Tocknell, “How does a Mach-Zehnder interferometer work?”, *Physics Education*, Vol. 35, No. 1, 2000.

74. Li, L., L. Xia, Z. Xie, and D. Liu, “All-fiber Mach-Zehnder interferometers for sensing applications”, *Optics Express*, Vol. 20, No. 10, 2012.

75. Hu, T., Y. Wang, C. Liao, and D. Wang, “Miniaturized fiber in-line Mach-Zehnder interferometer based on inner air cavity for high-temperature sensing”, Optics Letters, Vol. 37, No. 24, 2012.

76. Wang, Y., Y. Li, C. Liao, D. Wang, M. Yang, and P. Lu, “High-Temperature Sensing Using Miniaturized Fiber In-Line Mach-Zehnder Interferometer”, *IEEE Photonics Technology Letters*, Vol. 22, No. 1, pp. 39-41, 2010.

77. Wu, Q., A. M. Hatta, P. Wang, Y. Semenova and G. Farrell, “Use of a Bent Single SMS Fiber Structure for Simultaneous Measurement of Displacement and Temperature Sensing”, *IEEE Photonics Technology Letters*, Vol. 23, No. 2, pp. 130-132, 2011.

78. Liao, C. R., D. N. Wang, and Y. Wang, “Microfiber in-line Mach–Zehnder interferometer for strain sensing”, *Optics Letters*, Vol. 38, No. 5, pp. 757-759, 2013.

79. Wu, Y., Y. Xu, Y. Yang, W. Jin, Y. Jiang, Y. Shen and S. Jian “High-sensitivity pressure sensor based on fiber Mach-Zehnder interferometer”, *Measurement Science and Technology*, Vol. 28, No.10, 2017.

80. Yin, G., S. Lou, and H. Zou, “Refractive index sensor with asymmetrical fiber Mach–Zehnder interferometer based on concatenating single-mode abrupt taper and core-offset section”, *Optics & Laser Technology*, Vol. 45, pp. 294-300, 2013.

81. Liu, W., X. Wu, G. Zhang, S. Li, C. Zuo, S. Fang, and B. Yu, “Refractive index and temperature sensor based on Mach-Zehnder interferometer with thin fibers”, *Optical Fiber Technology*, Vol. 54, 2020.

82. Michelson, A. and E. Morley, “On the Relative Motion of the Earth and the Luminiferous Ether”, *American Journal of Science*, Vol. 34, No. 203, pp. 333-345, 1887.

83. Abbott, B. P., et al. (LIGO Scientific Collaboration and Virgo Collaboration), “Observation of Gravitational Waves from a 22- Solar-Mass Binary Black Hole Coalescence”, *Physical Review Letters*, Vol. 116, No. 24, 2016.

84. Qi, K., Y. Zhang, J. Sun, and G. Yi, “All-Fiber high temperature and refractive index sensor based on three microspheres array Michelson interferometer”, *Optics & Laser Technology*, Vol. 129, 2020.

85. Yuan, L., J. Yang and Z. Liu, “A Compact Fiber-Optic Flow Velocity Sensor Based on a Twin-Core Fiber Michelson Interferometer”, *IEEE Sensors Journal,* Vol. 8, No. 7, pp. 1114-1117, 2008.

86. Li, Z., C. Liao, Y. Wang, L. Xu, D. Wang, X. Dong, S. Liu, Q. Wang, K. Yang, and J. Zhou, “Highly-sensitive gas pressure sensor using twin-core fiber based in-line Mach-Zehnder interferometer”, *Optics Express,* Vol. 23, No. 5, pp. 6673-6678, 2015.

87. Sagnac, G., “L'éther lumineux démontré par l'effet du vent relatif d'éther dans un interféromètre en rotation uniforme (The demonstration of the luminiferous aether by an interferometer in uniform rotation)”, *Comptes Rendus,* Vol. 157, pp. 708–710, 1913.

88. Sagnac, G., “Sur la preuve de la réalité de l'éther lumineux par l'expérience de l'interférographe tournant (On the proof of the reality of the luminiferous aether by the experiment with a rotating interferometer)”, *Comptes Rendus,* Vol. 157, pp. 1410–1413, 1913.

89. He, X., C. Ma, X. Wang, Z. Wang, and L. Yuan, “Pressure vector sensor based on an orthogonal optical path Sagnac interferometer”, *Optics Express,* Vol. 28, No. 6, pp. 7969-7979, 2020.

90. Gao, P., X. Chen, and W. Feng, “Simultaneous measurement of external refractive index and temperature based on long-period-grating-inscribed Sagnac interferometer and fiber Bragg grating”, *Review of Scientific Instruments,* Vol. 83, No. 10, 2012.

91. Wang, X. Z. and Q. Wang. “A High-Birefringence Microfiber Sagnac-Interferometer Biosensor Based on the Vernier Effect”, *Sensors,* Vol. 18, No. 12, pp. 4414, 2018.

92. Zhao, J., Y. Zhao, L. Bai, and Y. Zhang, “Sagnac Interferometer Temperature Sensor Based on Microstructured Optical Fiber Filled with Glycerin”, *Sensors and Actuators A: Physical*, Vol. 314, 2020.

93. Sarkar, B., C. Koley, N. K. Roy, and P. Kumbhakar, “Condition monitoring of high voltage transformers using Fiber Bragg Grating Sensor”, *Measurement,* Vol. 74, pp. 255-267, 2015.

94. Suresh, R., S. C. Tjin, and J. Hao, “Applications of Fiber Bragg Grating Sensors”, *Smart Materials in Structural Health Monitoring, Control and Biomechanics*, Advanced Topics in Science and Technology in China, Springer, Berlin, Heidelberg. pp. 441-480, 2012.

95. Iadicicco, A., A. Cusano, S. Campopiano, A. Cutolo and M. Giordano, “Thinned fiber Bragg gratings as refractive index sensors”, *IEEE Sensors Journal*, Vol. 5, No. 6, pp. 1288-1295, 2005.

96. Hirayama, N. and Y. Sano, “Fiber Bragg grating temperature sensor for practical use”, *ISA Transactions*, Vol. 39, No. 2, pp. 169-173, 2000.

97. Liu, L., H. Zhang, Q. Zhao, Y. Liu, and F. Li, “Temperature-independent FBG pressure sensor with high sensitivity”, *Optical Fiber Technology*, Vol. 13, No. 1, pp. 78-80 2007.

98. Campanella, C. E, A. Cuccovillo, C. Campanella, A. Yurt, V. M. N. Passaro, “Fibre Bragg Grating Based Strain Sensors: Review of Technology and Applications”, *Sensors*, Vol. 18, No. 9, Article number: 3115, 2018.

99. Lu, P., N. Lalam, M. Badar, B. Liu, B. T. Chorpening, M. P. Buric, and P. R. Ohodnicki, “Distributed optical fiber sensing: Review and perspective”, *Applied Physics Reviews*, Vol. 6, No. 4, Article number:041302, 2019.

100. Bao, X. and L. Chen, “Recent Progress in Distributed Fiber Optic Sensors”, *Sensors*, Vol. 12, No. 7, pp. 8601-8639, 2012.

101. Schenato, L., “A Review of Distributed Fibre Optic Sensors for Geo-Hydrological Applications”, *Applied Sciences*, Vol. 7, No. 9, pp.896, 2017.

102. Lu, X., P. J. Thomas, and J. O Hellevang, “A Review of Methods for Fibre-Optic Distributed Chemical Sensing”, *Sensors*, Vol. 19, No. 13, pp. 2876, 2019.

103. Hartog, A., “Distributed Fiber-Optic Sensors: Principles and Applications”, *Optical Fiber Sensor Technology*, Springer, Boston, MA, pp. 241-301, 2000.

104. Schultz, D. I. and T. V. Jones, “Heat transfer Measurements in short-duration hypersonic facilities”, *AGARD-AG-165,* Advisory Group for Aerospace Research and Development Paris, France, 1973.

105. Bulut, K. and M. N. Inci, “Three-dimensional optical profilometry using a four-core optical fibre”, *Optics and Laser Technology*, Vol. 37, No. 6, pp. 463-469, 2005.

106. Inci, M. N., *Optical Coatings for Fibre Optic Sensors*, Ph.D. Thesis, Heriot-Watt University, 1992.

107. Gander, M. J., D. Macrae, E. A. C. Galliot, R. McBride, J. D. C. Jones, P. M. Blanchard, J. G. Burnett, A. H. Greenaway, and M. N. Inci, "Two-axis bend measurement using multicore optical fibre", *Optics Communications,* Vol. 182, No. 1-3, pp. 115-121, 2000.

108. Qu, H., G. F. Yan, and M. Skorobogatiy, "Interferometric fiber- optic bending/nano displacement sensor using plastic dual-core fiber", *Optics Letters,* Vol. 39, No. 16, pp. 4835-4838, 2014.

109. Antonio-Lopez, J. E., Z. S. Eznaveh, P. LiKamWa, A. Schülzgen, and R. Amezcua-Correa, "Multicore fiber sensor for high-temperature applications up to 1000°C", Optics Letters, Vol. 39, No. 15, pp. 4309-4312, 2014.

110. Aref, S. H., R. Amezcua-Correa, J. P. Carvalho, O. Frazão, P. Caldas, J. L. Santos, F. M. Araújo, H. Latifi, F. Farahi, L. A. Ferreira, and J. C. Knight, "Modal interferometer based on hollow-core photonic crystal fiber for strain and temperature measurement", Optics Express 17, Vol. 17, No. 21, pp. 18669-18675, 2009.

111. Blanchard, P. M., J. G. Burnett, G. R. G. Erry, A. H. Greenaway, P. Harrison, B. Mangan, J. C. Knight, P. St. J. Russell, M. J. Gander, R. McBride, and J. D. C. Jones, "Two-dimensional bend sensing with a single, multi-core optical fibre", *Smart Materials and Structures,* Vol. 9, No. 2, pp. 132-140, 2000.

112. Burnett, J. G.; Erry, G. R. G.; Dickson, R.; McBride, R.; Gander, M.; Jones, J. D. C.; Blanchard, P. M.; Harvey, A. R.; Greenaway, A. H. *Proc. Applied Optics Divisional Conf.*, 1998, 105-110.

113. Yılmaz, S. T., U. D. Özuğurel, K. Bulut, and M. N. Inci, "Vibration amplitude analysis with a single frame using a structured light pattern of a four-core optical fibre", *Optics Communications*, Vol. 249, No. 4-6, pp. 515-522, 2005.

114. Wallenberger, F.T., "Structural Silicate and Silica Glass Fibers", Materials Technology Series, Advanced Inorganic Fibers, Vol. 6, pp. 129-168, Springer, Boston, MA, 2000.

115. Asseh, A. S. Sandgren, H. Ahlfeldt, B. Sahlgren, R. Stubbe, and G. Edwall, "Fiber optical Bragg grating refractometer", *Fiber & Integrated Optics*, Vol. 17, No. 1, pp. 51-62, 1998.

116. Zhang, Q., L. L. Hu, Y. F. Qi, G. G. Liu, N. J. Ianno, and M. Han, "Fiber-optic refractometer based on a phase shifted fiber Bragg grating on a side-hole fiber", *Optics Express*, Vol. 23, No. 13, pp. 16750-16759, 2015.

117. Miao, Y. P., B. Liu, and Q. D. Zhao, "RI sensor based on measuring the transmission power of tilted fiber Bragg grating", *Optical Fiber Technology*, Vol. 15, No.3, pp. 233-236, 2009.

118. Cai, Z., F. Liu, T. Guo, B. O. Guan, G. D. Peng, and J. Albert, "Evanescently coupled optical fiber refractometer based a tilted fiber Bragg grating and a D-shaped fiber", *Optics Express*, Vol. 23, No. 16, pp. 20971-20976, 2015.

119. Li, T., X. Dong, C. C. Chan, C. L. Zhao, and S. Jin, "Power-Referenced Optical Fiber Refractometer Based on a Hybrid Fiber Grating", *IEEE Photonics Technology Letters*, Vol. 23, No. 22, pp. 1706-1708**,** 2011.

120. Liang, W. Y. Huang, Y. Xu, R. K. Lee, and A. Yariv, "Highly sensitive Fiber Bragg Grating RI Sensors", *Applied Physics Lett*ers, Vol. 86, No. 15, pp. 151122(1-3), 2015.

121. Chryssis, A. N., S. S. Saini, S. M. Lee, H. Yi, W. E. Bentley, and M. Dagenais, "Detecting Hybridization of DNA by highly sensitive evanescent field etched core fiber

Bragg grating", *IEEE Journal of Selected Topics in* Quantum Electronics, Vol. 11, No. 4, pp. 864-872, 2005.

122. Schroeder, K., W. Ecke, R. Mueller, R.Willsch, and A. Andreev, "A Fiber Bragg Grating Refractometer", *Measurement Science and Technology*, Vol. 12, No. 7, pp. 757-764, 2001.

123. Pereira, D. A., O. Frazao, and J. L. Santos, "Fiber Bragg Grating Sensing System for Simultaneous Measurement of Salinity and Temperature", *Optical Engineering*, Vol. 43, No. 2, pp. 299-304, 2004.

124. Chryssis, A. N., S. M. Lee, S.B. Lee, S. S. Saini, and M. Dagenais, "High Sensitivity Evanescent Field Fiber Bragg Grating Sensor", *IEEE Photonics Technology Letters,* Vol. 17, No. 6, pp. 1253-1255, 2015.

125. Loh, W., M. Cole, M. Zervas, S. Barcelos, and R. Laming, "Complex grating structures with uniform phase masks based on the moving fiber–scanning beam technique", *Optics Letters,* Vol. 20, No. 20, pp. 2051-2053, 1995.

126. Albert, J., B. Malo, K. O. Hill, F. Bilodeau, D. C. Johnson, and S. Theriault, "Comparison of one-photon and two-photon effects in the photosensitivity of germanium-doped silica optical fibers exposed to intense ArF excimer laser pulses", *Applied Physics Letters,* Vol. 67, No. 24, pp. 3529–3531, 1995.

127. Zhu, Y., Q. Zhang, G. Liu, X. Luo, and M. Han, "Fabry-Perot sensor using cascaded chirped fiber-Bragg-gratings with opposite chirp directions", *IEEE Photonics Technology Letters,* Vol. 30, No. 16, pp. 1431-1434, 2018.

128. McCarthy, P., "A Guide for Designing with Spherical Gradient-Index Materials Constrained to Real Material Properties in Code V", University of Rochester.

129. Saunders, J. E., C. Sanders, H. Chen, and H. P. Loock, "Refractive indices of common solvents and solutions at 1550 nm," *Applied Optics,* Vol. 55, No. 4, pp. 947-953, 2016.

130. Xu, W., X. G. Huang, and J. S. Pan, "Simple Fiber-Optic Refractive Index Sensor Based on Fresnel Reflection and Optical Switch", *IEEE Sensors Journal*, Vol. 13, No. 5, pp. 1571-1574, 2013.

131. Zaca-Moran, P., J. P. Padilla-Martinez, J. M. Perez-Corte, J. A. Davila-Pintle, J. G. Ortega-Mendoza, and N. Morales, "Etched optical fiber for measuring concentration and refractive index of sucrose solutions by evanescent waves", *Laser Physics*, Vol. 28, No. 11, 2018.